# ADVANCED TRANSCEIVER DESIGN FOR CONTINUOUS PHASE MODULATION

by

Barış Özgül

B.S., Electrical and Electronics Engineering, Boğaziçi University, 1998

M.S., Electrical and Electronics Engineering, Boğaziçi University, 2002

Submitted to the Institute for Graduate Studies in
Science and Engineering in partial fulfillment of
the requirements for the degree of
Doctor of Philosophy

Graduate Program in
Boğaziçi University
2008

ADVANCED TRANSCEIVER DESIGN FOR CONTINUOUS PHASE MODULATION

APPROVED BY:

| | |
|---|---|
| Prof. Hakan Deliç<br>(Thesis Supervisor) | ..... |
| Assist. Prof. Mutlu Koca<br>(Thesis Co-supervisor) | ..... |
| Assoc. Prof. Fatih Alagöz | ..... |
| Prof. Ümit Aygölü | ..... |
| Prof. Ayşın Ertüzün | ..... |
| Prof. Bülent Sankur | ..... |

DATE OF APPROVAL: 12.02.2008

# ACKNOWLEDGEMENTS

First of all, I would like to thank Prof. Hakan Deliç and Assist. Prof. Mutlu Koca for their invaluable help, encouragement, and support which made the accomplishment of this dissertation possible.

I am also thankful to the commitee members, namely, Prof. Ayşın Ertüzün, Prof. Ümit Aygölü, Prof. Bülent Sankur, and Assoc. Prof. Fatih Alagöz for their important contributions.

I would like to thank my friends and colleagues, especially Ersen Ekrem, Nazlı Güney, Cumhur Ozan Yalçın, Helin Dutağacı, Ender Konukoğlu, Celal Eşli, Erdem Yörük, and Uğur Bozkaya for their help and understanding.

I could not succeed without the support of my family. I would like to thank my father, Dr. Ali Rıza Özgül, and my brother, Dr. Alper Özgül, who still continue to stand beside me anytime I need. I would also like to thank the members of Satıoğlu family for their encouragement.

A special thank you goes to Ülgen Satıoğlu. I will always be grateful for your outstanding display of patience. A short break with you was enough to make long hours of work bearable. Thank you for being so special.

Finally, I would like to dedicate this dissertation to my mother Sabriye Özgül. Only thing I can do is to thank you very much for all those priceless things you did for me. I will always try to keep your memory alive.

This dissertation was partly supported by the Scientific and Technical Research Council of Turkey (TÜBİTAK) Integrated Doctorate Program (BDP), the Boğaziçi University Research Fund under Contracts 04HA201 and 06A204D, and the TÜBİTAK KARİYER Research Projects Fund under Contract 105E077.

# ABSTRACT


## ADVANCED TRANSCEIVER DESIGN FOR CONTINUOUS PHASE MODULATION

This dissertation proposes advanced transceiver designs applying turbo and space-time (ST) concepts to continuous phase modulation (CPM), which is preferred in numerous power- and band-limited communication systems for its constant envelope and spectral efficiency. Despite its highly attractive spectral properties, maximum-likelihood detection of CPM over the frequency-selective multipath fading channels can bring impractical complexity issues because of the intensive search over a single super trellis which combines the effects of the modulation and the multipath channel. Application of the reduced-state trellis search algorithms results in lower complexity but the computational load could still be prohibitively large to obtain high performance in long channel impulse responses. In the dissertation, instead of employing trellis-based combined detection methods, equalization and demodulation functions are separated and novel low-complexity receivers with soft-input soft-output (SISO) time-domain and frequency-domain linear equalizers are proposed for bit-interleaved coded CPM, which attain near-optimal performance by applying turbo processing. In the proposed receivers, the front-end soft-information-aided linear equalizer is followed by a central SISO CPM demodulator and a back-end SISO channel decoder where double turbo processing is employed by performing back-end demodulation/decoding iterations per each equalization iteration to improve the *a priori* information for the front-end equalizer. Performance for the frequency-domain equalization is further improved by proposing an orthogonal ST block coding scheme for CPM. The proposed technique maintains the constant envelope and the phase continuity of the CPM waveforms perfectly by using appropriate tail symbols and, therefore, has no impact on the spectral efficiency. Depending on the orthogonality of the ST combining, frequency-domain equalization is applied as in the case of single antenna transmissions without

any increase in the computational load. In the dissertation, the receiver complexity is reduced further by transferring all the equalization functions to the transmitter and employing pre-equalization. For precoding the CPM signals on multipath fading channels while maintaining the spectral efficiency, a novel ST pre-equalizer is proposed, limiting the envelope variations and attaining a peak-to-average power ratio that is close to one by using a transmit selection diversity scheme.

# ÖZET

## SÜREKLİ EVRE KİPLENİMİ İÇİN GELİŞMİŞ ALICI-VERİCİ TASARIMI

Sürekli evre kiplenimi (CPM) sabit zarfı ve spektral verimliliğinden dolayı pek çok güç ve bant kısıtlı iletişim sisteminde tercih edilmiştir. Bu tezde özyinelemeli ve uzay-zaman (ST) yöntemlerden faydalanılarak CPM için gelişmiş alıcı-verici tasarımları önerilmektedir. Doğrusal kiplenimlerden farklı olarak CPM sinyallerinin oluşturulması bir sonlu otomat tarafından gerçekleştirilmekte olup bu sonlu otomattaki durum sayısı kiplenimin hafıza büyüklüğü, kiplenim indisinin değeri ve sembol alfabesinin boyutuyla belirlenmektedir. Sağladığı üstün spektral verimliliğe rağmen CPM'nin çok yollu frekans seçici kanallar üzerinden en büyük olabilirlik kestirimi kiplenim ve çok yollu kanal hafızalarının birleşimini göz önüne alan bir süper kafes üzerinde yürütülen yoğun işlemlere dayanmaktadır. Bu durum alıcıda pratik boyutların üstünde işlemsel hacime neden olabilmektedir. Durum azaltılmış kafes araştırma algoritmalarının kullanımı bu karmaşıklığı belli bir ölçüde azaltmakla birlikte uzun kanal dürtü yanıtları söz konusu olduğunda problem devam etmektedir. Bu tezde bit serpiştirilmiş CPM için kafes tabanlı yöntemler uygulamak yerine denkleştirme ve geri kiplenim işlemlerini birbirinden ayıran ve yumuşak-girdi yumuşak-çıktı (SISO) özellikli zaman- veya frekans-bölgesel doğrusal denkleştiriciler kullanan özyinelemeli alıcılar önerilmekte ve uygulanan döngüler sayesinde en iyi başarıma yakın başarımlar elde edilmektedir. Önerilen alıcılarda ön kısımda bir SISO doğrusal denkleştirici bulunmakta ve bu denkleştiriciyi SISO özellikli geri kipleyici ve kanal kod çözücü takip etmektedir. Her denkleştirici döngüsünden sonra geri kipleyici ve kanal kod çözücü arasında döngüler koşturularak bir sonraki denkleştirme döngüsü için ön bilgi geliştirilmekte ve bu uygulama sonucu az karmaşıklıkla yüksek başarım elde edilmektedir. Önerilen frekans-bölgesel alıcının başarımı bir ST blok kodlama yöntemi uygulanarak daha da arttırılmıştır. Söz konusu ST blok kodlama yöntemi CPM'nin sabit zarf ve sürekli evre özelliklerine bir etki

yapmadığından spektral verimlilik aynen korunmuştur. Ayrıca uygulanan ST blok kod ortogonal olduğundan dolayı alıcıda herhangi bir yapısal değişikliğe veya işlemsel artışa neden olmamaktadır. Alıcı karmaşıklığının daha da azaltılması amacıyla vericide öndenkleştirme uygulanması bir diğer araştırma konusu olarak ele alınmaktadır. Bu çalışma sonucunda CPM'nin spektral verimliliği korunarak öndenkleştirilmesi için zarf değişintilerini kısıtlayan ve tepeden ortalamaya güç oranını bire yaklaştıran bir ST öndenkleştirme yöntemi önerilmektedir.

# TABLE OF CONTENTS

ACKNOWLEDGEMENTS . . . . . iii
ABSTRACT . . . . . iv
ÖZET . . . . . vi
LIST OF FIGURES . . . . . x
LIST OF TABLES . . . . . xiii
LIST OF SYMBOLS/ABBREVIATIONS . . . . . xiv
1. INTRODUCTION . . . . . 1
1.1. Background and Motivation . . . . . 1
1.2. Literature Review and Research Contributions . . . . . 2
1.3. Outline of Thesis . . . . . 7
2. RESEARCH PRELIMINARIES . . . . . 11
2.1. Signal Model . . . . . 11
2.1.1. Continuous Phase Modulation . . . . . 11
2.1.2. Approximation Methods for CPM . . . . . 16
2.2. Trellis Search Methods and Convergence Analysis for Turbo Decoding . 18
2.2.1. BCJR and Log-BCJR Algorithms . . . . . 20
2.2.2. Demodulation of CPM Using Log-BCJR Algorithm . . . . . 27
2.2.3. Convergence Analysis using EXIT Charts . . . . . 29
2.2.4. Convergence Analysis for Iterative Demodulation of CPM . . . 31
3. DOUBLE TURBO EQUALIZATION OF CPM WITH TIME DOMAIN PROCESSING . . . . . 35
3.1. Doubly-Iterative Equalization with Time Domain Processing . . . . . 36
3.1.1. Receiver Overview . . . . . 37
3.1.2. SIC/MMSE TDE . . . . . 40
3.1.3. Complexity Comparison . . . . . 45
3.2. EXIT Chart Analysis . . . . . 46
3.3. Simulation Results . . . . . 54
4. DOUBLE TURBO EQUALIZATION OF CPM WITH FREQUENCY DOMAIN PROCESSING . . . . . 58

4.1. Doubly-Iterative Equalization with Frequency Domain Processing . . . 60
4.1.1. Receiver Overview . . . 62
4.1.2. SIC/MMSE FDE . . . 63
4.1.3. Complexity Comparison . . . 65
4.2. EXIT Chart Analysis . . . 69
4.3. Simulation Results . . . 74
5. ORTHOGONAL ST BLOCK CODING OF CPM ON MULTIPATH FADING CHANNELS . . . 78
5.1. Orthogonal ST Block Coding of CPM for Frequency-Domain Equalization 79
5.1.1. ST Block Coding for CPM . . . 81
5.1.2. Frequency-Domain Equalization for ST Block-Coded CPM . . . 84
5.2. Simulation Results . . . 86
6. ST PRE-EQUALIZATION OF CPM ON MULTIPATH FADING CHANNELS 89
6.1. Space-Time Pre-Equalization of Continuous Phase Modulation . . . 91
6.2. Analyses for the Error Performance and the Number of Antennas . . . 98
6.2.1. Upper Bound on the Error Performance . . . 98
6.2.2. Analysis for the Number of Antennas . . . 101
6.3. Simulations . . . 102
7. CONCLUSIONS . . . 111
APPENDIX A: MEAN CPM SIGNALS BASED ON BIT PROBABILITIES . 113
APPENDIX B: MMSE FILTER COEFFICIENTS FOR SIC/FDE . . . 115
APPENDIX C: TIME-REVERSED CPM SIGNALS . . . 117
REFERENCES . . . 119

# LIST OF FIGURES

Figure 2.1. Turbo decoding of serially concatenated convolutional codes . . . . 20

Figure 2.2. Receiver EXIT charts for the turbo demodulation and decoding of coded CPM . . . . . 32

Figure 2.3. BER performance for the turbo demodulation and decoding of coded CPM . . . . . 33

Figure 3.1. The transmitter for the bit-interleaved coded CPM and the channel 36

Figure 3.2. Doubly-iterative receiver with TDE . . . . . 37

Figure 3.3. Transfer characteristics of the doubly-iterative receiver . . . . . 46

Figure 3.4. Transfer characteristic curves for the SIC/TDE at $E_b/N_0 = 3$ and 6 dB . . . . . 48

Figure 3.5. Comparison of the simulated trajectories and the characteristic curves for the TDE and the demodulator at $E_b/N_0$=3 dB . . . . . 50

Figure 3.6. EXIT chart analysis for the back-end iterations of the doubly-iterative receiver with TDE . . . . . 52

Figure 3.7. Analysis for the front-end and back-end iterations of the doubly-iterative receiver with TDE . . . . . 53

Figure 3.8. BER performance for no ISI, Proakis' A channel, and channel I . . 55

Figure 3.9. BER performance in channels I and II . . . . . 56

Figure 4.1. Modulating sequence with the cyclic prefix . . . . . 60

Figure 4.2. Doubly-iterative receiver with FDE . . . . . 62

Figure 4.3. Transfer characteristic curves for the SIC/FDE at $E_b/N_0 = 3$ and 6 dB . . . . . 71

Figure 4.4. EXIT chart analysis for the back-end iterations of the doubly-iterative receiver with FDE . . . . . 72

Figure 4.5. Analysis for the front-end and back-end iterations of the doubly-iterative receiver with FDE . . . . . 73

Figure 4.6. BER performance for no ISI, Proakis' A channel and channel I . . 75

Figure 4.7. BER performance of turbo FDE in channels I and II . . . . . 76

Figure 5.1. Modulating sequence for the ST block coding scheme with the cyclic prefix . . . . . 81

Figure 5.2. BER performance for the turbo FDE with/without ST combining, TAE, and no ISI scenario . . . . . 86

Figure 5.3. BER performance for the turbo FDE with ST combining . . . . . 87

Figure 6.1. Space-time CPM pre-equalizer . . . . . 95

Figure 6.2. Power spectra for the original and the precoded CPM signals . . . 104

Figure 6.3. Distance $\bar{D}$ versus $N_t$ for $\nu = 3$ and 5 . . . . . 105

Figure 6.4. BER performance for the no ISI scenario, FDE, and the pre-equalizers 106

Figure 6.5. BER performance of the CPM demodulator and the upper bound, $p_{me}$, for $N_T = 6$ . . . . . 107

Figure 6.6. BER performance of the CPM demodulator and the upper bound, $p_{me}$, for $\nu = 5$ . . . . . 107

Figure 6.7. BER for different maximum Doppler spread ($f_m$) values, where $N_T = 6$, $\nu = 5$, and $L_c = 20$ . . . . . 108

Figure 6.8. Turbo performance for $f_m t_f = 0.001$, $N_T = 6$, $\nu = 5$, and $L_c = 20$ . 109

# LIST OF TABLES

Table 4.1. Complexity of the SISO Modules Used by the Proposed Receiver, the Receivers in Chapter 3 and [23], and TAE . . . . . 66

Table 4.2. Computational Complexity per Signal Block for the Proposed Receiver, the Turbo Equalizers in Chapter 3 and [23], and TAE . . . 67

Table 6.1. Envelope Variations for the Precoded CPM . . . . . 103

# LIST OF SYMBOLS/ABBREVIATIONS

| | |
|---|---|
| $a_{k,i}$ | Projection coefficient of the $i$th complex exponential basis function at the $k$th symbol interval |
| $\tilde{a}_{k,i}$ | Projection coefficient of the $i$th orthonormal basis function at the $k$th symbol interval |
| $A_{\mathrm{D}}$ | Average information at the input of the equalizer |
| $A_{\mathrm{E}}$ | Average information at the output of the equalizer |
| $A_{\mathrm{E}}^{'}$ | Normalized $A_{\mathrm{E}}$ |
| $A_i$ | Modulo operation parameter for the real part of the projection coefficient of the $i$th orthonormal basis function |
| $b_i$ | $i$th data bit |
| $B$ | Length parameter for TDE filter |
| $B_i$ | Modulo operation parameter for the imaginary part of the projection coefficient of the $i$th orthonormal basis function |
| $c(t, \mathbf{x}_1^k)$ | CPM signal produced by the symbol sequence $\mathbf{x}_1^k$ |
| $c_{i,b}(t)$ | Space-time block-coded CPM signal transmitted from the $i$th antenna during the $b$th block interval |
| $\breve{c}(t)$ | Time-reversed CPM signal |
| $\mathbf{c}$ | Sequence of CPM signal samples |
| $\bar{\mathbf{c}}$ | Sequence of mean values of CPM signal samples |
| $c_n$ | $n$th CPM signal sample |
| $\mathbf{c}_n$ | Vector of CPM signal samples involved in the computation of the $n$th TDE filter output |
| $\bar{c}_n$ | Mean value for the $n$th CPM signal sample |
| $\bar{\mathbf{c}}_n$ | Vector of mean values of CPM signal samples involved in the computation of the $n$th TDE filter output |
| $\hat{c}_n$ | Equalizer output in the time domain for the $n$th CPM signal sample |
| $\mathbf{c}_1$ | Vector for the first block of CPM signal samples |
| $\mathbf{c}_2$ | Vector for the second block of CPM signal samples |
| $C_k$ | $k$th DFT coefficient for the CPM signal samples |

| | |
|---|---|
| $\bar{C}_k$ | $k$th DFT coefficient for the mean values of CPM signal samples |
| $\hat{C}_k$ | $k$th equalizer output in the frequency domain |
| $\mathbf{C}_1$ | Vector of DFT coefficients for the first block of CPM signal samples |
| $\mathbf{C}_2$ | Vector of DFT coefficients for the second block of CPM signal samples |
| $\bar{\mathbf{C}}_1$ | Vector of DFT coefficients for the mean values of the first block of CPM signal samples |
| $\bar{\mathbf{C}}_2$ | Vector of DFT coefficients for the mean values of the second block of CPM signal samples |
| $\hat{\mathbf{C}}_1$ | Vector of FDE outputs for the first block of CPM signal samples |
| $\hat{\mathbf{C}}_2$ | Vector of FDE outputs for the second block of CPM signal samples |
| $\mathbf{d}_m$ | $m$th codeword produced by the inner encoder |
| $d_n$ | $n$th inner code bit |
| $d_{n,i}$ | Complex amplitude of the $i$th Laurent pulse at the $n$th symbol interval |
| $D_i(t)$ | $i$th Laurent pulse |
| $D_{ij}(\tau)$ | Correlation function of the $i$th and $j$th Laurent pulses |
| $\mathbf{e}$ | $(L_f + L_c - 1) \times 1$ vector employed in FAI scenario for TDE |
| $E_b$ | Bit energy |
| $f_c$ | Carrier frequency |
| $f_i$ | Frequency of the $i$th complex exponential basis function |
| $\mathbf{f}_n$ | Time-varying TDE filter vector to compute the $n$th equalizer output |
| $\mathbf{f}_{\text{FAI}}$ | Time-invariant TDE filter vector for FAI case |
| $\mathbf{f}_{\text{ZAI}}$ | Time-invariant TDE filter vector for ZAI case |
| $F$ | Length parameter for TDE filter |
| $g(t)$ | Frequency shaping pulse for CPM |
| $G$ | Length of the cyclic prefix |
| $h$ | Modulation index for CPM |

| | |
|---|---|
| $\tilde{\mathbf{h}}$ | Sequence of fading coefficients for the fractionally-spaced multipath channel |
| $h_\ell$ | Fading coefficient of the $\ell$th channel path |
| $h_{\ell,p}$ | Fading coefficient of the $\ell$th channel path corresponding to $p$th transmit antenna |
| $\tilde{h}_l$ | Fading coefficient of the $l$th fractionally-spaced channel path |
| $\tilde{\mathbf{H}}$ | Convolution matrix for the fractionally-spaced multipath fading channel |
| $\tilde{H}_k$ | $k$th DFT coefficient for the fading coefficients of the fractionally-spaced multipath channel |
| $I(t)$ | ISI function |
| $I_{k,i}$ | ISI projection coefficient of the $i$th orthonormal basis function at the $k$th symbol interval |
| $\tilde{I}_{k,i}$ | Scaled ISI projection coefficient |
| $I_{\text{Dec}}$ | Mutual information at the output of the channel decoder |
| $I_{\text{D}\to\text{Dec}}$ | Mutual information at the output of the demodulator |
| $J$ | Number of bits for the quantization of the first channel path coefficient |
| $J_{\text{MSE}}(\mathbf{f})$ | MSE cost function for TDE |
| $J_{\text{MSE}}(W)$ | MSE cost function for FDE |
| $l_c$ | Memory length of the outer convolutional code |
| $l_e$ | Number of tail symbols to return to and stay at the zero state in the CPE trellis |
| $l_f$ | Number of tail symbols to maintain the phase continuity during interblock transitions |
| $l_t$ | Number of tail symbols to return to the zero state in the CPE trellis |
| $L$ | Memory length of CPM |
| $L(b_i)$ | Output LLR for the $i$th data bit |
| $L(u_m)$ | Input LLR for the $m$th outer code bit |
| $L_a(b_i)$ | *A priori* LLR for the $i$th data bit |
| $L_a(\tilde{u}_m)$ | *A priori* LLR for the $m$th interleaved outer code bit |
| $L_b$ | Length of the data bit sequence |

| | |
|---|---|
| $L_c$ | Number of taps for the fractionally-spaced multipath fading channels |
| $L_d$ | Length of the inner code bit sequence |
| $L_e(u_m)$ | Extrinsic LLR for the $m$th outer code bit |
| $L_e(\tilde{u}_m)$ | Extrinsic LLR for the $m$th interleaved outer code bit |
| $L_f$ | Length of the TDE filter |
| $L_u$ | Length of the outer code bit sequence |
| $M$ | Modulation order |
| $M_c$ | Length of the multipath channel impulse response in terms of symbol intervals |
| $n_f$ | Number of front-end iterations for the doubly-iterative receiver |
| $n_i$ | Number of iterations for the previously proposed turbo equalizers and at the back end of the doubly-iterative receiver |
| $n_s$ | Number of samples per symbol period |
| $N$ | Length of the modulating symbol sequence |
| $\bar{N}$ | Length of the modulating symbol sequence with redundancy |
| $\tilde{N}$ | Length of the received signal sequence after sampling |
| $N_b$ | Number of basis functions |
| $N_c$ | Number of taps for the multipath fading channels |
| $N_p$ | Number of Laurent pulses |
| $N_T$ | Number of transmit antennas |
| $N_0$ | One-sided power spectral density for AWGN |
| $\mathcal{P}$ | Denominator of the modulation index |
| $\mathbf{q}$ | $(L_f + L_c - 1) \times 1$ vector employed in ZAI scenario for TDE |
| $q(t)$ | Phase shaping pulse for CPM |
| $\breve{q}(t)$ | Time-reversed phase shaping pulse for CPM |
| $Q$ | Numerator of the modulation index |
| $r(t)$ | Received signal |
| $r_n$ | $n$th received signal sample |
| $\mathbf{r}_n$ | Vector of received signal samples involved in the computation of the $n$th TDE filter output |

| | |
|---|---|
| $\mathbf{R}$ | Vector of DFT coefficients for the received signal samples after ST combining |
| $\mathfrak{R}$ | Autocorrelation matrix for CPM |
| $\mathcal{R}(\tau)$ | Autocorrelation function for CPM |
| $\mathbf{R}_b$ | Vector of DFT coefficients for the received signal samples in the $b$th block |
| $\mathcal{R}_i$ | $\mathcal{R}(\tau)$ for $\tau = iT_s$ |
| $R_k$ | $k$th DFT coefficient for the received signal samples |
| $s$ | Index of the selected transmit antenna |
| $S$ | Number of states in CPE trellis |
| $\tilde{S}$ | Number of tilted-phase CPM signals |
| $S_{\text{in}}$ | Number of trellis states for the inner encoder |
| $S_{\text{out}}$ | Number of trellis states for the outer encoder |
| $\mathbf{t}$ | Training symbol sequence |
| $T$ | Symbol duration |
| $T_s$ | Sampling period |
| $\mathbf{u}_\ell$ | $\ell$th codeword produced by the outer encoder |
| $u_m$ | $m$th outer code bit |
| $\tilde{u}_m$ | $m$th interleaved outer code bit |
| $U$ | Block length |
| $\mathbf{v}$ | Sequence of AWGN samples |
| $v(t)$ | AWGN |
| $v_n$ | $n$th AWGN sample |
| $\mathbf{v}_n$ | Vector of AWGN samples involved in the computation of the $n$th TDE filter output |
| $\mathbf{V}_b$ | Vector of DFT coefficients for the AWGN samples in the $b$th block interval |
| $\tilde{\mathbf{V}}_1$ | Vector of DFT coefficients for the AWGN samples for the first block after ST combining |
| $\tilde{\mathbf{V}}_2$ | Vector of DFT coefficients for the AWGN samples for the second block after ST combining |
| $V_k$ | $k$th DFT coefficient for the AWGN samples |

| | |
|---|---|
| $\mathbf{w}$ | Sequence of the IDFT coefficients for the FDE filter coefficients |
| $w_n$ | $n$th IDFT coefficient for the FDE filter coefficients |
| $\mathbf{W}$ | Diagonal matrix of FDE filter coefficients |
| $\mathcal{W}(t)$ | Symbol independent part of the tilted phase |
| $\breve{\mathcal{W}}(t)$ | Time-reversed $W(t)$ |
| $W_k$ | $k$th FDE filter coefficient |
| $W_k^{\mathrm{FAI}}$ | $k$th FDE filter coefficient in case of FAI |
| $W_k^{\mathrm{ZAI}}$ | $k$th FDE filter coefficient in case of ZAI |
| $\mathbf{x}$ | Sequence of modulating symbols |
| $\dot{\mathbf{x}}$ | Sequence of modulating symbols with redundancy |
| $\breve{\mathbf{x}}$ | Reversed modulating symbol sequence |
| $\dot{\mathbf{x}}_{i,b}$ | Sequence of modulating symbols with redundancy to produce $b$th CPM signal block from the $i$th transmit antenna |
| $x_\ell$ | $\ell$th element of the modulating symbol sequence |
| $\dot{x}_\ell$ | $\ell$th element of the modulating symbol sequence with redundancy |
| $\breve{x}_\ell$ | $\ell$th element of the reversed modulating symbol sequence |
| $y(t, \mathbf{x}_1^k)$ | Tilted-phase CPM signal produced by the symbol sequence $\mathbf{x}_1^k$ |
| $\breve{y}(t)$ | Time-reversed tilted-phase CPM signal |
| $y_n$ | $n$th tilted-phase CPM signal sample |
| $\bar{y}_n$ | Mean value for the $n$th tilted-phase CPM signal sample |
| $\hat{y}_n$ | Equalizer output in the time domain for the $n$th tilted-phase CPM signal sample |
| $Y_{i,p}$ | $i$th sample of the $p$th tilted-phase CPM signal |
| $z(t)$ | Pre-equalized signal in case of single transmit antenna |
| $z_p(t)$ | Pre-equalized signal transmitted from the $p$th antenna |
| $\alpha(s_m)$ | Forward recursion term for the BCJR algorithm |
| $\tilde{\alpha}(s_m)$ | Forward recursion term for the Log-BCJR algorithm |
| $\beta(s_m)$ | Backward recursion term for the BCJR algorithm |
| $\tilde{\beta}(s_m)$ | Backward recursion term for the Log-BCJR algorithm |

| | |
|---|---|
| $\gamma$ | Pre-equalizer parameter to scale the envelope variations |
| $\gamma(s_{m-1}, s_m)$ | State transion term for the BCJR algorithm |
| $\tilde{\gamma}(s_{m-1}, s_m)$ | State transion term for the BCJR algorithm |
| $\lambda_{m,i}$ | Projection coefficient of the $i$th orthonormal basis function on the $m$th tilted-phase CPM signal |
| $\mathbf{\Lambda}$ | Diagonal channel matrix in the frequency domain after ST combining |
| $\mathbf{\Lambda}_1$ | Diagonal matrix of the DFT coefficients for the multipath channel coefficients corresponding to first antenna |
| $\mathbf{\Lambda}_2$ | Diagonal matrix of the DFT coefficients for the multipath channel coefficients corresponding to second antenna |
| $\mu$ | Symbol gain for the equalizer output |
| $\tilde{\mu}$ | Modulo operation parameter |
| $\nu$ | Transmit antenna selection parameter |
| $\phi_i(t)$ | $i$th orthonormal basis function |
| $\rho_\ell$ | Amplitude of the fading coefficient of the $l$th channel path |
| $\rho_{\ell,p}$ | Amplitude of the fading coefficient of the $l$th channel path corresponding to $p$th transmit antenna |
| $\rho_T$ | Summation of the first fading channel path amplitudes for all transmit antennas |
| $\bar{\sigma}^2$ | Average variance computed by the probability mapper |
| $\sigma_v^2$ | Variance of AWGN samples |
| $\theta_\ell$ | Phase of the fading coefficient of the $l$th channel path |
| $\theta_{\ell,p}$ | Phase of the fading coefficient of the $l$th channel path corresponding to $p$th transmit antenna |
| $\varphi(t, \mathbf{x}_1^k)$ | Phase function produced by the symbol sequence $\mathbf{x}_1^k$ |
| $\tilde{\varphi}(t, \mathbf{x}_1^k)$ | Tilted-phase function produced by the symbol sequence $\mathbf{x}_1^k$ |
| $\varphi_k$ | Cumulative phase at the $k$th symbol interval |
| $\tilde{\varphi}_k$ | Cumulative tilted phase at the $k$th symbol interval |
| $\varphi_L(t, \mathbf{x}_{k-L+1}^k)$ | Non-cumulative phase function at the $k$th symbol interval |
| $\tilde{\varphi}_L(t, \mathbf{x}_{k-L+1}^k)$ | Non-cumulative tilted-phase function at the $k$th symbol interval |

| | |
|---|---|
| $\varphi_{i,b}(t)$ | Phase function producing the space-time block-coded CPM signal transmitted from the $i$th antenna during the $b$th block interval |
| $\vartheta(t, \breve{\mathbf{x}}_1^k)$ | Time-reversed phase function |
| $\tilde{\vartheta}(t, \breve{\mathbf{x}}_1^k)$ | Time-reversed tilted-phase function |
| $\vartheta_k$ | Time-reversed cumulative phase |
| $\tilde{\vartheta}_k$ | Time-reversed cumulative tilted-phase |
| $\vartheta_L(t, \breve{\mathbf{x}}_{k-L+1}^k)$ | Time-reversed non-cumulative phase function |
| $\tilde{\vartheta}_L(t, \breve{\mathbf{x}}_{k-L+1}^k)$ | Time-reversed non-cumulative tilted-phase function |

| | |
|---|---|
| APP | *A posteriori* probability |
| AWGN | Additive white Gaussian noise |
| BCJR | Bahl-Cocke-Jelinek-Raviv |
| BER | Bit-error rate |
| BFDE | Block frequency-domain equalizer |
| BIT | Back-end iteration |
| CED | Combined equalizer/demodulator |
| CPE | Continuous phase encoder |
| CPM | Continuous phase modulation |
| CSI | Channel state information |
| DFE | Decision-feedback equalizer |
| FDE | Frequency-domain equalizer |
| FER | Frame error rate |
| FIT | Front-end iteration |
| i.i.d. | independent and identically distributed |
| MAP | Maximum *a posteriori* probability |
| me | Modulo operation error |
| MM | Memoryless modulator |
| MMSE | Minimum mean-squared error |
| MSE | Mean-squared error |
| nSnOEE | Non-symmetric non-orthogonal exponential expansion |
| PAPR | Peak-to-average power ratio |

| | |
|---|---|
| PDF | Probability density function |
| SIC | Soft-interference canceller |
| SISO | Soft-input soft-output |
| SnOEE | Symmetric non-orthogonal exponential expansion |
| SnOEE | Symmetric orthogonal exponential expansion |
| TDE | Time-domain equalizer |
| TLE | Turbo linear equalizer |
| TAE | Turbo *a posteriori* probability equalizer |
| TH | Tomlison-Harashima |

# 1. INTRODUCTION

## 1.1. Background and Motivation

Continuous phase modulation (CPM) is a well-known digital modulation scheme with constant envelope and continuous phase properties yielding high power and spectral efficiency [1, 2]. The phase continuity is maintained by the memory added in the modulation process which makes CPM attain better bandwidth characteristics and error performance compared to the linear constant-envelope modulation schemes such as phase-shift keying (PSK) in the expense of increased detection complexity. Depending on these properties, CPM becomes a popular choice for many communication systems with low peak-to-average power ratio (PAPR) and narrow bandwidth requirements. Among the best-known CPM schemes are the raised cosine with pulse length $L$ ($L$RC), tamed frequency modulation (TFM), generalized TFM (GTFM), minimum-shift keying (MSK), and Gaussian MSK (GMSK). The last scheme is the modulation technique specified in the Digital Enhanced Cordless Telecommunications (DECT) [3] and Global System for Mobile (GSM) [4] standards and is also used in the 2.5G and 2.75G technologies such as General Packet Radio Service (GPRS) and Enhanced GPRS (EGPRS) [5], respectively.

The modulation operation of CPM, associated with its intrinsic memory, can be represented by a finite-state machine or a trellis diagram. This makes the use of trellis search algorithms possible for the optimal demodulation of the CPM signals. The complexity of the search is determined by the number of trellis states which depends on the value of the modulation index, size of the input alphabet and the order of the modulation memory. In [6], the CPM modulator is decomposed as a continuous phase encoder (CPE) and a memoryless modulator (MM) where the CPE is equivalent to a convolutional encoder. Thus, the cascade of an outer convolutional encoder with an interleaver and the CPE can be viewed as the serial concatenation of two convolutional encoders separated by an interleaver. This makes the application of the iterative joint demodulation and decoding possible at the receiver by the exchange of soft information

between a soft-input soft-output (SISO) CPM demodulator and a SISO channel decoder [7, 8]. Here, both decoders are implemented by the SISO trellis search algorithms such as the *a posteriori* probability (APP) algorithm which is also known as the Bahl-Cocke-Jelinek-Raviv (BCJR) algorithm [9]. When the CPM signals are subject to multipath fading, the memory effects of both the modulator and the intersymbol interference (ISI) channel are combined in a single super-trellis over which a trellis search is performed for the joint equalization/demodulation [10]. For coded CPM signals, one can then couple this equalizer/demodulator with the back-end channel decoder to implement a turbo-type receiver. However, when the order of the modulation and/or channel memory is high, size of the resulting joint trellis is prohibitively large, making even non-iterative equalization practically unwieldy.

The objective of this dissertation is to design advanced transmitter and receivers for the detection of CPM over multipath fading channels. For this purpose, turbo receivers using time-domain and frequency-domain linear equalizers are proposed to detect the CPM signals with low computational complexity while achieving near-optimal performance. The performance is further improved by devising an orthogonal space-time (ST) block coding scheme which also preserves the constant envelope and the phase continuity properties for CPM. Then, a ST channel precoding scheme is proposed to transfer all the equalization functions to the transmitter and to reduce the complexity of the receiver significantly. During the pre-equalization of the CPM signals, spectral efficiency is maintained by using a transmit selection diversity scheme.

### 1.2. Literature Review and Research Contributions

Turbo equalization, introduced in [11] as a joint equalization and decoding method for data protected by an error-correcting code, has been shown to be highly effective against the ISI effects of frequency-selective multipath wireless channels. The corresponding turbo receiver iteratively exchanges probabilistic information between the SISO equalizer and decoder, both implemented by the BCJR algorithm. Unfortunately, because the front-end SISO equalizer relies on trellis search techniques, this type of turbo equalization has only been applicable to cases with a few number of

states, which typically occur for narrowband channels. This disadvantage of the so-called maximum *a posteriori* probability (MAP) equalizers has been removed by replacing the trellis-based SISO equalizer with a soft-information aided transversal filter. This time-domain filter used for minimum mean-squared error (MMSE) equalization is equipped with an *a priori* soft interference canceller (SIC) and an APP mapper so that it is capable of processing and generating soft information, as described for binary and $M$-ary linear modulation in [12, 13] and [14, 15], respectively. Despite its suboptimal performance compared to that of a MAP equalizer, such a filter yields a feasible turbo receiver scheme for channels with a long impulse response since it does not encounter the memory requirements and exponentially growing complexity of trellis-based approaches.

The methods above for linear modulations depend on soft information exchange between the equalizer at the front-end and the back-end channel decoder. However, for CPM, the iterations must be performed between the more-complex combined equalizer/demodulator (CED) that is described in Section 1.1 and the back-end channel decoder if optimal equalization/demodulation is considered. In order to circumvent the complexity limitations for CED that emerge from the size of the super-trellis it is associated with, suboptimal reduced-state SISO decoding algorithms have been proposed to yield a less intensive search [16, 17]. However the computational load for such algorithms is still exponentially constrained with the modulation and/or channel memory. An alternative approach to attain lower complexity is to separate the equalization and demodulation operations and assign those to a linear MMSE equalizer and a trellis-based demodulator, respectively. Depending on this architecture, a time-domain decision-feedback equalizer (DFE) followed by a Viterbi decoder has been proposed for CPM in [18]. However, this receiver is not suitable for turbo-equalization since the proposed DFE does not have any SISO capabilities.

**Contribution 1**: Details of the first contribution in this dissertation are as follows.

- A low-complexity turbo receiver is proposed, which consists of a front-end lin-

ear time-domain equalizer (TDE), a central CPM demodulator, and a back-end channel decoder where all three blocks have SISO capabilities.

- The proposed receiver performs double iterations among these blocks for soft-interference cancellation and turbo demodulation/decoding.
- Doubly iterative architecture yields high turbo gain with low complexity.
- Convergence behavior of the proposed receiver is analyzed and its bit-error rate (BER) performance is illustrated.

All the aforementioned linear TDEs compute the MMSE equalizer coefficients by employing cumbersome matrix inversions which may still cause the computational load to be relatively large for channels with long impulse responses. As presented in [19]-[21], performing the same operation in the frequency domain with the aid of a cyclic guard interval renders the equalizer complexity independent of the channel memory and the computation load is reduced further while attaining the same and often better performance. The frequency-domain equalization approach has also been extended for CPM in [22], where the frequency-domain equalizer (FDE) filter is not equipped with any SISO capability and, thus, is not suitable for turbo processing. The advantages of frequency-domain processing and iterative information exchange are combined in [23], where a turbo linear equalizer (TLE) is presented in which a SISO block-form FDE (BFDE) is followed by the SISO CPM demodulator and channel decoder modules. Here, the soft CPM signal information to start the subsequent equalization iterations are computed from the code bit probabilities obtained from the back-end channel decoder. However, this produces long error bursts due to the inherent modulation memory and thus, the CPM signal probabilities are delivered to BFDE module only at certain epoches to break up the error propagation at the expense of obtaining only a slight turbo gain. Moreover, because the proposed FDE operates on blocks of information, it still involves matrix inversions which result in an increased computational cost.

**Contribution 2**: The second contribution of this dissertation can be itemized as below.

- A soft-information-aided FDE is proposed for CPM which replaces the TDE in the aforementioned doubly-iterative receiver and also overcomes the disadvantages of the BFDE in [23].
- Better error performance with lower computational complexity is attained compared to both of the methods mentioned above.
- Convergence behavior of the doubly-iterative receiver with the proposed FDE is analyzed and its BER performance is illustrated.
- Performance of the SISO FDE can be improved further by applying an appropriate ST coding scheme at the transmitter.

ST coding combined with CPM is very suitable in terms of bandwidth and power efficiency, as also described in [24]-[29] by assuming single-path fading channels that are approximately constant at each symbol interval. In all these methods, ST coding is applied to information symbols prior to the CPM modulation to maintain the phase continuity. However, this approach results in extra computations at the receiver since the existing detection techniques for single antenna transmissions cannot be applied due to the inherent memory of CPM. Furthermore, in [24]-[27], the phase trellis of CPM is modified and, therefore, the receiver designs are specific to the ST coding schemes applied. The method in [28] results in moderate receiver complexity but it is not suitable for the CPM schemes out of MSK. Contrary to the aforementioned methods, ST coding in [30] is applied directly to the CPM waveforms rather than the information symbols, by assuming slowly-varying flat fading channels which are almost constant throughout two signal blocks. Since the proposed ST block coding scheme is orthogonal, the existing detection techniques for single antenna transmissions can be applied. During the transitions from one block to the next, guard intervals are used to minimize the phase discontinuities. However, for a given antenna, the signals transmitted at the consecutive blocks belong to different CPM schemes, respectively. Therefore, it is not possible to attain the exact phase continuity during the interblock transitions which yields that the spectral efficiency cannot be maintained perfectly. Furthermore, the method above is also not applicable in the presence of multipath fading channels.

**Contribution 3**: Details of the third contribution in this dissertation are listed below.

- An orthogonal ST block coding scheme that preserves the spectral efficiency of CPM perfectly is proposed
- The proposed method results in significant diversity gain for the frequency-domain equalization of CPM signals by deploying two transmit antennas.
- For the ST block coding, the scheme in [31] for linear modulations is modified to maintain the bandwidth efficiency of CPM.
- During interblock transitions and while appending the cyclic prefix, tail symbols are used to keep the signal phase continuous.
- After the appropriate sampling and the ST combining, the aforementioned doubly-iterative receiver structure is employed as in case of single antenna transmissions. BER performance is illustrated.

Application of linear TDE and FDE methods for CPM results in lower complexity receivers compared to the ones using trellis-based decoders, as previously described. However, employing channel precoding (or pre-equalization) at a base-station transmitter can reduce the complexity further at the mobile receivers with limited resources [32]. A well-known non-linear pre-equalization technique is Tomlinson-Harashima (TH) precoding [33, 34]. TH-type precoding uses modulo-arithmetic operations to maintain the stability of the transmitter, whereas its application to the phase modulated waveforms results in large envelope fluctuations and destroys the spectral efficiency. The dimension partitioning techniques which are proposed for quadrature PSK (QPSK) in [35] and $\pi/4$-QPSK in [36] keep the signal amplitude constant and only allow the distortion of the signal phase for pre-equalization. Such techniques divide the whole signal space into non-overlapping square partitions and enlarge the decision regions by generating the replicas of the central partition that defines the corresponding signal constellation. In [36], dimension partitioning is also applied to MSK because it can be represented as offset QPSK with half-sinusoid pulse shaping. However, this type of pre-equalization is not applicable to other CPM schemes in general since they cannot be represented by square signal constellations. The methods in [37] and [38] present frequency-domain

pre-equalizers for multipath fading channels. Furthermore, there are combined equalizers that consider pre-equalization at the transmitter and post-equalization at the receiver to increase the channel capacity rather than to reduce the receiver complexity, as described in [39] and [40]. However, application of the aforementioned frequency-domain pre-equalization and combined equalization methods to CPM signals results in envelope variations and phase discontinuities which disrupt the spectral efficiency. The CPM precoders in [41]-[45] yield good spectral properties but these methods aim to equalize the inherent ISI that results from the modulation memory rather than to mitigate the interfering effects of the multipath fading channels.

**Contribution 4**: Details of the final contribution in this dissertation are as follows.

- For precoding the CPM signals on multipath channels while maintaining the spectral efficiency, a ST pre-equalizer is proposed.
- The pre-equalizer limits the envelope variations and attains a PAPR that is close to one by using a transmit selection diversity scheme.
- One of the antennas is chosen to transmit the actual CPM signal and the rest of the antennas transmit bandwidth-efficient CPM-like signals for the ISI cancellation.
- An upper bound on the error performance is derived and the relationship between the number of antennas and the spectral efficiency is analyzed.
- Power spectra for the precoded signals and the BER performance are illustrated.

## 1.3. Outline of Thesis

This dissertation aims to propose advanced transmitter and receiver designs for CPM over multipath fading channels to achieve low detection complexity while attaining good performance by applying turbo and ST methods. The dissertation outline is as follows.

In the present chapter, background and motivation, literature review together

with the research contributions, and the outline of the dissertation are presented.

In Chapter 2, the preliminary information to be used in the rest of the dissertation is given, which are the signal model and the SISO trellis search methods together with the convergence analysis for the turbo receivers.

In Chapter 3, a soft-information-aided TDE is proposed, which is deployed in a doubly-iterative receiver structure for the low-complexity turbo equalization of coded CPM with high performance. After presenting the doubly-iterative architecture coupling the central CPM demodulator with both the front-end TDE and the back-end channel decoder, the derivation of the MMSE coefficients for the TDE filter is described. The proposed method is shown to result in less computational complexity compared to the turbo receiver employing a CED together with a channel decoder. The convergence behavior of the proposed receiver is determined by using extrinsic information transfer (EXIT) chart analysis which is proposed as a semi-analytical tool in [46] for turbo receivers that consist of two decoders. Because the doubly-iterative receiver has three SISO modules, a three dimensional graph as in [47] is illustrated to observe the convergence behavior between the CPM demodulator and the back-end channel decoder while the *a priori* information from the TDE improves. The BER simulations yield that high performance can be attained with low complexity by applying an efficient iteration strategy between the front-end TDE and the back-end receiver modules which is determined by the three-dimensional EXIT chart analysis.

In Chapter 4, a soft-information-aided FDE filter is introduced replacing the SISO TDE at the front-end of the doubly-iterative receiver in Chapter 3, where a cyclic prefix is appended to the transmitted packets to obtain a convenient signal representation at the receiver for frequency-domain equalization. First the method for the cyclic prefix addition while maintaining the phase continuity of CPM is described. Then the MMSE filter coefficients for the proposed FDE are derived. It is shown that the doubly-iterative receiver with the proposed FDE is less complex than not only the optimal CED implementation followed by a back-end channel decoder as in [10] but also the turbo receivers applying linear equalization methods such as the doubly-

iterative receiver with TDE in Chapter 3 and the TLE in [23] using a BFDE filter. The convergence behavior of the proposed receiver is analyzed using three-dimensional EXIT charts as in Chapter 3. The BER simulations yield that the proposed methods attain a better performance compared to the turbo receivers in Chapter 3 and in [23].

In Chapter 5, a ST block coding scheme using two transmit antennas is proposed. The ST block code maintains the phase continuity of the CPM signals not to disrupt the spectral efficiency and provides an orthogonal representation in the frequency domain so that the SISO FDE filter introduced in Chapter 3 can be applied as in case of single antenna transmission. After describing the details for the proposed scheme and the insertion of the guard intervals to main the phase continuity, the orthogonal representation that is obtained after appropriate sampling, low-pass filtering, and combining is presented and the aforementioned doubly-iterative receiver with the SISO FDE filter is applied. Depending on the orthogonality of the scheme, it is presented that the receiver architecture and the computational complexity remain unchanged. As verified by the BER simulations, the ST block coding results in significant diversity gain compared to the case with single antenna transmissions in Chapter 3.

In Chapter 6, a ST pre-equalization technique maintaining the spectral efficiency of CPM by exploiting a transmit selection diversity scheme is introduced. First a pre-equalization method which depends on the direct application of the TH-type precoding to the CPM signals is described where the resulting signal is shown to encounter large envelope variations that disrupt the spectral efficiency. Then the ST pre-equalization scheme is presented to alleviate the envelope variations using a scaling factor which is determined depending on a transmit selection diversity scheme. After describing the proposed method, the design of a training signal to estimate a channel parameter at the receiver is given. For the error performance of the system, an upper bound is derived. Furthermore the effect of the number of transmitted antennas on alleviation of the envelope variations and, therefore, on the spectral efficiency is analyzed. For different values of system parameters, power spectra of the resulting precoded signals are depicted. The BER performance is also presented for different number of antennas and different bandwidth and channel scenarios.

The conclusions for this dissertation and the discussions for future research contributions are presented in Chapter 7.

# 2. RESEARCH PRELIMINARIES

In this chapter, an overview of the signal model, the SISO trellis search methods, and the convergence analysis techniques for the turbo receivers are given, which are all applied in the remainder of the dissertation.

## 2.1. Signal Model

Phase modulation procedure for CPM, properties of the CPM signals, and the representation for the transmissions over multipath fading channels are presented in Section 2.1.1. The expansion methods to approximate the CPM signals by using a few pulses are summarized briefly in Section 2.1.2.

### 2.1.1. Continuous Phase Modulation

CPM is a nonlinear modulation scheme with memory. Given the $M$-ary symbol sequence $\mathbf{x}_1^k = [x_1, x_2, \ldots, x_k]$ with $x_k \in \{\pm 1, \pm 3, \ldots, \pm M-1\}$, the baseband CPM signal with unit amplitude is expressed as [2]

$$c(t, \mathbf{x}_1^k) = e^{j\varphi(t, \mathbf{x}_1^k)}, \qquad (k-1)T \le t \le kT, \qquad k = 1, 2, \ldots, N, \tag{2.1}$$

where $T$ is the symbol interval, $N$ is the block length, and

$$\varphi(t, \mathbf{x}_1^k) = 2\pi h \sum_{i=1}^{k} x_i q\big(t-(i-1)T\big) = \varphi_k \; + \; \varphi_L(t, \mathbf{x}_{k-L+1}^k). \tag{2.2}$$

with

$$\varphi_k \;\; = \;\; \pi h \sum_{i=1}^{k-L} x_i, \tag{2.3}$$

$$\varphi_L(t, \mathbf{x}_{k-L+1}^k) \;\; = \;\; 2\pi h \sum_{i=k-L+1}^{k} x_i q\big(t-(i-1)T\big) \tag{2.4}$$

as the cumulative and the time-varying non-cumulative phase specifying the CPM signal on the interval $(k-1)T < t < kT$, respectively. The signal generation for CPM can be described by a finite-state machine, where each state is defined by

$$\mathbf{s}_k := \{\varphi_k, x_{k-L+1}, \ldots, x_{k-2}, x_{k-1}\} \tag{2.5}$$

and the information symbol, $x_k$, results in the state transition. The phase shaping function $q(t)$ in (2.4) is defined as

$$q(t) = \int_0^t g(\tau)d\tau = \begin{cases} 0 & \text{for} \quad t < 0, \\ \frac{1}{2} & \text{for} \quad t \geq LT \end{cases}$$

where $g(t)$ is zero outside the interval $0 \leq t \leq LT$ and $L \geq 1$ is the length of the modulation memory. CPM is classified as full- and partial-response for $L = 1$ and $L > 1$, respectively. The modulation index is $h = Q/\mathcal{P}$ where $Q$ and $\mathcal{P}$ are relatively prime integers. The cumulative phase in (2.3) can take $\mathcal{P}$ and $2\mathcal{P}$ different values when $Q$ is even and odd, respectively. When $Q$ is odd, only $\mathcal{P}$ values from $2\mathcal{P}$ possible values are available for $\varphi_k$ while the remaining $\mathcal{P}$ values become active on the next symbol interval for $\varphi_{k+1}$. Thus, CPM signal is represented by a time-varying and periodic trellis diagram with a period of $2T$ for odd $Q$ values. The total number of trellis states are $\mathcal{P}M^{L-1}$ and $2\mathcal{P}M^{L-1}$ for even and odd $Q$, respectively. There are $M$ branches starting from each trellis state which merge into $M$ different states, respectively, where each branch corresponds to a state transition that generates a different CPM signal.

Note that due to the non-linear relation in (2.1), the CPM signals are correlated in time. The direct computation of the corresponding autocorrelation function is difficult. However, for binary CPM, this function can be computed through Laurent's decomposition in [48], which represents (2.1) linearly in terms of $N_p = 2^{L-1}$ pulse amplitude modulation (PAM) waveforms as

$$c(t, \mathbf{x}_1^N) = \sum_{n=1}^{N} \sum_{i=0}^{N_p-1} d_{n,i} D_i(t - (n-1)T) \tag{2.6}$$

where $D_i(t)$ are the Laurent pulses, and

$$d_{n,i} = e^{jh\pi\left(\sum_{k=1}^{n} x_k - \sum_{k=1}^{L-1} x_{n-k}\varepsilon_{i,k}\right)}. \tag{2.7}$$

Here

$$i = \sum_{k=1}^{L-1} 2^{k-1}\varepsilon_{i,k} \qquad 0 \le i \le N_p - 1, \tag{2.8}$$

where $\varepsilon_{i,k} \in \{0, 1\}$ are the coefficients of the binary representation of $i$. Then, by assuming that the bits $x_k$ are equiprobable, the autocorrelation function for binary CPM is found in [48] as

$$\mathcal{R}(\tau) = \sum_{i=0}^{N_p-1}\sum_{j=0}^{N_p-1}\sum_{\rho=-\infty}^{\infty} [\cos(h\pi)]^{\Delta(i,j,\rho)} D_{ij}(\tau - \rho T) = \mathcal{R}(-\tau) \tag{2.9}$$

where $\mathcal{R}(\tau) = \mathrm{E}[c(t, \mathbf{x}_1^N)c^*(t+\tau, \mathbf{x}_1^N)]$ with

$$D_{ij}(\tau) = D_{ji}(-\tau) = \int_{-\infty}^{\infty} D_i(t)D_j(t+\tau)dt, \tag{2.10}$$

for $i, j = 0, \ldots, N_p - 1$, and

$$\Delta(i,j,\rho) = |\rho| + \sum_{k=1}^{L-1}(\varepsilon_{i,k} + \varepsilon_{j,k}) - 2\left[\sum_{\substack{k\le -\rho-1 \\ k\le L-1}}^{k\ge 1} \varepsilon_{i,k} + \sum_{\substack{k\le \rho-1 \\ k\le L-1}}^{k\ge 1} \varepsilon_{j,k} + \sum_{\substack{k\le L-1-\rho \\ k\le L-1}}^{\substack{k\ge 1 \\ k\ge 1-\rho}} \varepsilon_{i,k}\varepsilon_{j,k+\rho}\right]. \tag{2.11}$$

If $|\rho|$ is greater than $L - 1$, (2.11) becomes

$$\Delta(i,j,\rho) = |\rho + \Delta(i,j,\infty)| \qquad |\rho| \ge L \tag{2.12}$$

with

$$\Delta(i,j,\infty) = \sum_{k=1}^{L-1}(\varepsilon_{i,k} - \varepsilon_{j,k}). \tag{2.13}$$

The autocorrelation function in (2.9) is applicable for binary CPM schemes only. However, these results are also extended for $M$-ary CPM in [52].

In [6], the CPM modulator is presented as the combination of a CPE that is equivalent to a recursive convolutional encoder and a MM. The CPE considers a tilted-phase representation for CPM signals which results in a time-invariant trellis whether $Q$ is even or odd. Using (2.1), the tilted-phase CPM signal is expressed as

$$y(t, \mathbf{x}_1^k) = c(t, \mathbf{x}_1^k) e^{j\pi h(M-1)t/T} = e^{j\tilde{\varphi}(t, \mathbf{x}_1^k)} \tag{2.14}$$

implying that

$$\tilde{\varphi}(t, \mathbf{x}_1^k) = \varphi(t, \mathbf{x}_1^k) + \frac{\pi h(M-1)t}{T} \tag{2.15}$$

where $\tilde{\varphi}(t, \mathbf{x}_1^k)$ is

$$\tilde{\varphi}(t, \mathbf{x}_1^k) = 2\pi h \sum_{i=1}^{k-L} \tilde{x}_i + 4\pi h \sum_{i=k-L+1}^{k} \tilde{x}_i q\big(t-(i-1)T\big) + \pi h \mathcal{W}\big(t-(k-1)T\big) \tag{2.16}$$

for $(k-1)T \le t \le kT$ with $\tilde{x}_i = (x_i + M - 1)/2$, $\tilde{x}_i \in \{0, 1, \ldots, M-1\}$. The last term $\mathcal{W}(t)$ in (2.16) is independent of data symbols such that

$$\mathcal{W}(t) = (M-1)t/T - 2(M-1)\sum_{i=0}^{L-1} q(t+iT) + (M-1)(L-1), \qquad 0 \le t \le T. \tag{2.17}$$

The cumulative tilted-phase part in (2.16) is represented as

$$\tilde{\varphi}_k = 2\pi h \sum_{i=1}^{k-L} \tilde{x}_i \tag{2.18}$$

which can take $\mathcal{P}$ possible values. Thus, the trellis for CPE has $S = \mathcal{P}M^{L-1}$ states where the state transitions yield $\tilde{S} = \mathcal{P}M^L$ different tilted-phase CPM signals. Thus, the total number of states in the CPM tilted-phase trellis is $\mathcal{P}M^{L-1}$ which is less than

the number states in the CPM trellis when $Q$ is odd. Before transmitting the tilted-phase signals, the carrier frequency should be changed from $f_c$ to $f_c - h(M-1)/(2T)$ to compensate for the frequency shift in (2.14). Depending on the similarity of CPE to a recursive convolutional coder [6] where a length-$l_t$ tail sequence can be used to go from any state to the zero state represented as

$$\{\tilde{\varphi}_k = 0, \tilde{x}_{k-L+1} = 0, \ldots, \tilde{x}_{k-1} = 0\} \tag{2.19}$$

or to the following state represented as

$$\{\tilde{\varphi}_k = \pi, \tilde{x}_{k-L+1} = 0, \ldots, \tilde{x}_{k-1} = 0\} \tag{2.20}$$

if $\mathcal{P}$ is even. The only difference of the latter state compared to the zero state is the value of $\tilde{\varphi}_k$.

The multipath fading channels can be represented by a finite number of distinct propagation paths where each path has a time-varying complex gain and a certain propagation delay [49]-[51]. Depending on this representation, the time-varying multipath fading channel can be modelled as a tapped-delay-line filter denoted as

$$h(t,\tau) = \sum_{m=0}^{N_c-1} h_m(t)\delta(\tau - \tau_m(t)) \tag{2.21}$$

where $N_c$ is the number of paths, $h_m(t)$ and $\tau_m(t)$ are the time-varying fading coefficient and propagation delay for the $m$th path, respectively. Transmission of the CPM signal in (2.1) through the multipath fading channel in (2.21) yields

$$r(t) = \int_{-\infty}^{+\infty} h(t,\tau)c(t-\tau, \mathbf{x}_1^N)d\tau + v(t) = \sum_{m=0}^{N_c-1} h_m(t)c(t-\tau_m(t), \mathbf{x}_1^N) + v(t) \tag{2.22}$$

where $0 < t < NT$ and $v(t)$ is the AWGN.

In the dissertation, the multipath fading channel is assumed to be time-invariant

throughout a CPM signal block such that it can be modelled as [10, 23]

$$h(t) = \sum_{m=0}^{N_c-1} h_m \delta(t - \tau_m) \tag{2.23}$$

where $h_m$ and $\tau_m$ are the time-invariant fading coefficient and propagation delay for the $m$th path, respectively, and $h_m = \rho_m e^{j\theta_m}$ with $\rho_m$ and $\theta_m$ denoting the amplitude and the phase of the $m$th path, respectively. For practical purposes, CPM signal can be considered as band-limited to $|f| \leq W/2$. Then, choosing a sampling period, $T_s$, such that $T_s \leq 1/W$ and $T_s = T/n_s$ with $n_s \in \mathbb{Z}^+$, the path delays $\tau_m$ in (2.23) can be assumed as the integer multiples of $T_s$, approximately. Then, the channel impulse function in (2.23) can be described as fractionally spaced as in [10] where

$$h(t) = \sum_{l=0}^{L_c-1} \tilde{h}_l \delta(t - lT_s). \tag{2.24}$$

Here, $L_c = \tau_{N_c-1}/T_s + 1$, with $\tau_{N_c-1}$ being the maximum path delay, $\tilde{h}_l = h_m$ for $l = \tau_m/T_s$ and $\tilde{h}_l = 0$ for all other $l$ values. Then the received signal can be expressed as

$$r(t) = \int_{-\infty}^{+\infty} h(\tau) c(t - \tau, \mathbf{x}_1^N) d\tau + v(t) = \sum_{l=0}^{L_c-1} \tilde{h}_l c(t - lT_s, \mathbf{x}_1^N) + v(t) \tag{2.25}$$

where $0 < t < NT$ and $v(t)$ is the AWGN.

### 2.1.2. Approximation Methods for CPM

The number of matched filters required for the optimal detection of CPM is $M^L$ [2]. To reduce this number, several suboptimal methods are also proposed. Such methods depend on the approximation of the CPM signal by using a few basis functions. By modifying Laurents PAM decomposition in (2.6) for $M$-ary CPM in [52] the number of matched filters reduces to $(M-1)M^{L-1}$, and a further reduction is possible by using only a few most significant pulses for approximation. In [53], the aforementioned method is extended for $M$-ary multi-$h$ CPM. Number of pulses for the approximation

of $M$-ary CPM are reduced significantly in [54] and [55]. However, in all the aforementioned methods, the principle expansion pulses have a partial-response structure that does not allow simple signal processing at the receiver.

Inspired by Fourier series, it is also possible to use complex exponentials to approximate the CPM signal in (2.14) as

$$y(t, \mathbf{x}_1^k) \approx \frac{1}{\sqrt{T}} \sum_{i=1}^{N_b} a_{k,i} e^{j2\pi f_i (t-(k-1)T)}, \qquad (k-1)T \leq t \leq kT \tag{2.26}$$

where $N_b$ is the number of basis functions, and $f_i$ and $a_{k,i}$ denote the frequency and the complex coefficient for the $i$th pulse, respectively. Here, $N_b$ is assumed to be odd, and the coefficients $\{a_{k,i}\}$ are found by projecting the CPM signal at the $k$th symbolling interval onto $\frac{1}{\sqrt{T}}\, e^{j2\pi f_i t}$, $0 \leq t \leq T$, for $i = 1, \ldots, N_b$, respectively. The complex exponential bases in (2.26) admit simple signal processing since they do not have a partial-response structure. However, the frequencies $\{f_i\}$ must be set appropriately to achieve good approximation accuracy while applying a few basis functions. In [56], the frequencies are set as $f_i = f_s(i - \lceil N_b/2 \rceil)/T$ with $0 < f_s < 1$, where $\lceil \cdot \rceil$ denotes the ceiling operation. For a given value of $N_b$, the frequency separation, $f_s$, is optimized for each CPM waveform to minimize the MSE between the actual and approximate signal. Compared to the scenario where the signal frequencies are set with fixed separations as $f_i = (i - \lceil N_b/2 \rceil)/T$, same accuracy is achieved by a significant reduction in the number of basis functions. In both scenarios, equally spaced frequencies are considered where the latter frequency set results in orthogonal basis functions. Thus, the expansions using the former and latter set of frequencies are named as symmetric non-orthogonal exponential expansion (SnOEE) and symmetric orthogonal exponential expansion (SOEE), respectively. In [57], an alternative exponential expansion method is proposed with a different strategy to set the frequencies, which requires fewer basis functions than SOEE and SnOEE while attaining the same accuracy. This approach is called as non-symmetric non-orthogonal exponential expansion (nSnOEE) where the symmetric frequency constraint in SnOEE is removed. In nSnOEE, it is assumed that $-1/T \leq f_i \leq 1/T$ since most of the CPM signal energy is concentrated in the fre-

quency interval $[-1/T, 1/T]$ [2]. Finding the optimal set of frequencies that minimizes the MSE between the actual and approximate signals requires an exhaustive search [57]. It is still possible to obtain orthogonal bases from the aforementioned complex exponentials via the Gram-Schmidt orthogonalization such that

$$\phi_i(t) = \frac{1}{\sqrt{T}} \sum_{k=1}^{N_b} b_{i,k} e^{j2\pi f_k t}, \qquad 0 \le t \le T \tag{2.27}$$

for $i = 1, 2, \ldots, N_b$ where $b_{i,k}$ is the complex coefficient of the $k$th exponential waveform to compute the $i$th orthonormal basis function. Similar to (2.26), the CPM signal is approximated by the orthonormal basis functions in (2.27) as

$$y(t, \mathbf{x}_1^k) \approx \sum_{i=1}^{N_b} \tilde{a}_{k,i} \phi_i\big(t - (k-1)T\big), \qquad (k-1)T \le t \le kT \tag{2.28}$$

where

$$\tilde{a}_{k,i} = \int_{(k-1)T}^{kT} y(t, \mathbf{x}_1^k) \phi_i^*\big(t - (k-1)T\big) dt \tag{2.29}$$

for $i = 1, \ldots, N_b$, and $(\cdot)^*$ is the complex conjugate operation. There are $\tilde{S}$ possible tilted-phase CPM signals which yields $\tilde{S}$ different sets of complex projection coefficients. The set of projection coefficients for the $m$th tilted-phase CPM signal can be denoted as $\Lambda_m = \{\lambda_{m,1}, \lambda_{m,2}, \ldots, \lambda_{m,N_b}\}$ for $m = 1, 2, \ldots, \tilde{S}$, where $\lambda_{m,i}$ is found by projecting the $m$th tilted-phase signal to the $i$th basis function. Therefore, considering that the $m$th signal is generated on the $k$th symbol interval, it can be concluded that $\tilde{a}_{k,i} = \lambda_{m,i}$ for $i = 1, \ldots, N_b$.

## 2.2. Trellis Search Methods and Convergence Analysis for Turbo Decoding

The trellis search methods can be applied for different operations at the receiver, such as the decoding of a convolutional, demodulation of a trellis-based modulation scheme, or the equalization of a signal transmitted over a multipath fading channel. The Viterbi algorithm (VA) is a popular choice for the trellis search, which produces

hard decisions for the maximum likelihood estimation of a sequence [58]. For the inner and outer decoding of two convolutional codes, it can be possible to apply two serially-concatenated Viterbi decoders (VDs) at the receiver. However the error bursts from the inner VD deteriorate the performance of the outer VD. To prevent the error bursts, it is possible to apply deinterleaving between the inner and outer VD (and also interleaving after the outer encoder at the transmitter). However, by producing hard decisions only, the inner decoder results in some information loss which also degrades the performance of the outer decoder whether deinterleaving is applied or not. To circumvent this problem, the inner decoder can employ the modified VAs, such as the soft output VA (SOVA) [59] or the list output VA (LOVA) [60] which are capable of producing probabilistic (soft) information rather than the hard decisions.

It is possible to attain further performance gain by transferring the soft information at the output of the outer decoder back to the inner decoder which exploits this input information to produce a more reliable output information. This type of information exchange at the receiver is called as turbo (or iterative) processing. The blocks in a turbo receiver must employ SISO algorithms not only to produce *a posteriori* soft information but also to be able to process *a priori* soft information. One of the best-known SISO trellis search algorithms is the MAP or the BCJR algorithm [9]. This algorithm performs the optimal symbol-by-symbol detection of a received sequence rather than finding the most likely sequence. Because each symbol is detected by using all the previous and proceeding symbol information in the sequence, more complex computations are required compared to the aforementioned VAs. However, the intrinsic SISO nature of the BCJR algorithm makes its use attractive for the iterative receivers. The BCJR algorithm encounters some operational problems because of the numerical representation of the probabilities and non-linear functions in the computations and because of the mixed multiplications and additions of these values. To circumvent such problems in practice, log-domain implementations such as the suboptimal Max-Log-BCJR algorithm in [61] and the optimal Log-BCJR algorithm in [62] can be used.

In the rest of the dissertation, the Log-BCJR algorithm is applied when the trellis

search is necessary. However, if lower computational complexity is desired, it is also possible to employ the reduced state implementations as in [63] without imposing any architectural change on the proposed iterative receivers. In Section 2.2.1 the BCJR algorithm is described first and then the modifications for the Log-BCJR implementation are presented. Furthermore, application of the Log-BCJR algorithm for the SISO demodulation of CPM is shown in Section 2.2.2. The convergence analysis for the turbo receivers by exploiting EXIT charts is described in Section 2.2.3. The application of EXIT chart analysis on the iterative demodulation of coded CPM is presented in Section 2.2.4.

### 2.2.1. BCJR and Log-BCJR Algorithms

The BCJR algorithm can be employed by the turbo receiver in Figure 2.1 for the inner and outer decoding of the two cascaded convolutional codes with an interleaver

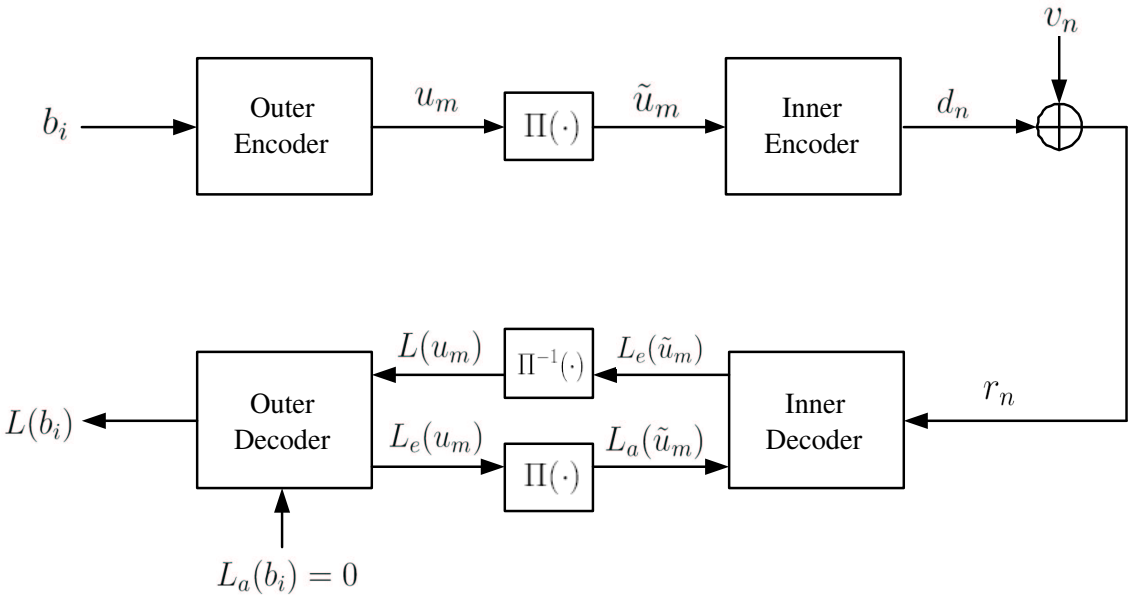



Figure 2.1. Turbo decoding of serially concatenated convolutional codes

in between. The interleaving and deinterleaving operations are denoted by $\Pi(.)$ and $\Pi^{-1}(.)$, respectively. At the transmitter, the length-$L_b$ data bit sequence with elements, $b_i \in \{-1, +1\}$, $i = 1, 2, \ldots, L_b$, is encoded by the rate-$1/m_o$ outer convolutional code with single input and $m_o$ outputs form the code bits $u_m \in \{-1, +1\}$, $m = 1, 2, \ldots, L_u$, where $L_u = m_o L_b$. The $i$th codeword produced by the outer encoder can be de-

noted as $\mathbf{u}_i$, $i = 1, 2, \ldots, L_b$, where the $\ell$th bit of this codeword is $\mathbf{u}_i(\ell) = u_{m_o i - m_o + \ell}$, $\ell = 1, \ldots, m_o$. Then, $u_m$ are interleaved to $\tilde{u}_m$, which are fed to the rate-$1/m_i$ inner convolutional encoder to form $d_n \in \{-1, +1\}$, $n = 1, 2, \ldots, L_d$, where $L_d = m_i L_u$. The $m$th codeword produced at the output of the inner encoder can be represented as $\mathbf{d}_m$, $m = 1, 2, \ldots, L_u$, where the $\ell$th bit of this codeword is $\mathbf{d}_m(\ell) = d_{m_i m - m_i + \ell}$, $\ell = 1, \ldots, m_i$. Denoting the inner and outer code memory lengths as $l_i$ and $l_o$, respectively, the number of trellis states for the inner convolutional code is $S_{\text{in}} = 2^{l_i}$ and it is $S_{\text{out}} = 2^{l_o}$ for the outer convolutional code. After the transmission through the AWGN channel, the output symbol sequence is denoted as $\mathbf{r}_1^{L_u} = \{\mathbf{r}_1, \mathbf{r}_2 \ldots \mathbf{r}_{N_0}\}$ where $\mathbf{r}_m(\ell) = r_{m_i m - m_i + \ell}$ is the $(m_i m - m_i + \ell)$th received symbol for $m = 1, 2, \ldots, L_u$ and $\ell = 1, 2, \ldots, m_i$, and

$$r_n = d_n + v_n, \qquad n = 1, 2, \ldots, L_d. \tag{2.30}$$

In (2.30) $v_n$ is a Gaussian random variable with zero mean and variance being equal to $\sigma_v^2$.

Given the received sequence, the inner decoder employs the BCJR algorithm to compute the *a-posteriori* information for the outer code bits by using the *a priori* information at its input. The *a-posteriori* information is generated as a log-likelihood ratio (LLR) which is represented as

$$L(\tilde{u}_m) = \log \frac{P(\tilde{u}_m = +1 | \mathbf{r}_1^{L_u})}{P(\tilde{u}_m = -1 | \mathbf{r}_1^{L_u})}. \tag{2.31}$$

Using the Bayes' rule, (2.31) is rewritten as

$$L(\tilde{u}_m) = \log \frac{P(\tilde{u}_m = +1, \mathbf{r}_1^{L_u})}{P(\tilde{u}_m = -1, \mathbf{r}_1^{L_u})}. \tag{2.32}$$

The probabilities in (2.32) can be expressed as

$$P(\tilde{u}_m = b, \mathbf{r}_1^{L_u}) = \sum_{S(\tilde{u}: \tilde{u}_m = a)} P(s_{m-1}, s_m, \mathbf{r}_1^{L_u}) \tag{2.33}$$

where $a \in \{-1, +1\}$ is the value of the outer code bit and $S(\tilde{u} : \tilde{u}_m = a)$ denotes the transitions in the inner code trellis from the state, $s_{m-1}$, at time $m-1$ to the state, $s_m$, at time $m$ when $\tilde{u}_m = a$. The probabilities in (2.33) can be expressed as

$$\begin{aligned} P(s_{m-1}, s_m, \mathbf{r}_1^{L_u}) &= P(s_{m-1}, s_m, \mathbf{r}_1^{m-1}, \mathbf{r}_m, \mathbf{r}_{m+1}^{L_u}), \\ &= P(s_{m-1}, \mathbf{r}_1^{m-1}) P(s_m, \mathbf{r}_m, \mathbf{r}_{m+1}^{L_u} | s_{m-1}, \mathbf{r}_1^{m-1}), \\ &= P(s_{m-1}, \mathbf{r}_1^{m-1}) P(s_m, \mathbf{r}_m, \mathbf{r}_{m+1}^{L_u} | s_{m-1}), \\ &= P(s_{m-1}, \mathbf{r}_1^{m-1}) P(s_m, \mathbf{r}_m | s_{m-1}) P(\mathbf{r}_{m+1}^{L_u} | s_{m-1}, s_m, r_m), \\ &= P(s_{m-1}, \mathbf{r}_1^{m-1}) P(s_m, \mathbf{r}_m | s_{m-1}) P(\mathbf{r}_{m+1}^{L_u} | s_m). \end{aligned} \tag{2.34}$$

Since it is possible to exactly determine $\mathbf{d}_m$ and the corresponding input symbol $\tilde{u}_m$ in case of the state transition from $s_{m-1}$ to $s_m$, the probability $P(s_m, \mathbf{r}_m | s_{m-1})$ in (2.34) is represented as

$$\begin{aligned} P(s_m, \mathbf{r}_m | s_{m-1}) &= P(\mathbf{r}_m | s_{m-1}, s_m) P(s_m | s_{m-1}) \\ &= P(\mathbf{r}_m | \mathbf{d}_m) P(\tilde{u}_m) \end{aligned} \tag{2.35}$$

where

$$P(\mathbf{r}_m | \mathbf{d}_m) = \frac{1}{(2\pi\sigma_v^2)^{m_i/2}} e^{-\frac{1}{2\sigma_v^2} \sum_{\ell=0}^{m_i-1} |\mathbf{r}_m(\ell) - \mathbf{d}_m(\ell)|^2}. \tag{2.36}$$

Then, (2.32) can be rewritten as

$$L(\tilde{u}_m) = \log \frac{\sum_{S(\tilde{u}:\tilde{u}_m=+1)} \alpha(s_{m-1}) \gamma(s_{m-1}, s_m) \beta(s_m)}{\sum_{S(\tilde{u}:\tilde{u}_m=-1)} \alpha(s_{m-1}) \gamma(s_{m-1}, s_m) \beta(s_m)}, \tag{2.37}$$

where $\alpha(s_{m-1})$, $\gamma(s_{m-1}, s_m)$, and $\beta(s_m)$ stand for the forward recursion term, transition

probability, and the reverse recursion term, respectively, which are defined as

$$\begin{aligned} \alpha(s_m) &:= P(s_m, \mathbf{r}_1^m), && (2.38)\\ \gamma(s_{m-1}, s_m) &:= P(s_m, \mathbf{r}_m | s_{m-1}) = P(\mathbf{r}_m|\mathbf{d}_m)P(\tilde{u}_m), && (2.39)\\ \beta(s_m) &:= P(\mathbf{r}_{m+1}^{L_u}|s_m). && (2.40) \end{aligned}$$

Using (2.39), the LLR in (2.37) can be represented as

$$L(\tilde{u}_m) = \underbrace{\log \frac{\sum_{S(\tilde{u}:\tilde{u}_m=+1)} \alpha(s_{m-1})P(\mathbf{r}_m|\mathbf{d}_m)\beta(s_m)}{\sum_{S(\tilde{u}:\tilde{u}_m=-1)} \alpha(s_{m-1})P(\mathbf{r}_m|\mathbf{d}_m)\beta(s_m)}}_{L_e(\tilde{u}_m)} + \underbrace{\log \frac{P(\tilde{u}_m=+1)}{P(\tilde{u}_m=-1)}}_{L_a(\tilde{u}_m)} \qquad (2.41)$$

where the LLRs $L_e(\tilde{u}_m)$ and $L_a(\tilde{u}_m)$ are the extrinsic information at the output of the inner decoder and the *a priori* information from the outer decoder, respectively, as also shown in Figure 2.1. Depending on (2.41), the extrinsic information is computed as $L_e(\tilde{u}_m) = L(\tilde{u}_m) - L_a(\tilde{u}_m)$ so that it does not depend on the *a priori* information from the outer decoder.

The relationship between the consecutive forward recursion terms is found as

$$\begin{aligned} \alpha(s_m) &= \sum_{s_{m-1}} P(s_{m-1}, s_m, \mathbf{r}_1^m),\\ &= \sum_{s_{m-1}} P(s_{m-1}, \mathbf{r}_1^{m-1}) P(s_m, \mathbf{r}_m | s_{m-1}, \mathbf{r}_1^{m-1}),\\ &= \sum_{s_{m-1}} P(s_{m-1}, \mathbf{r}_1^{m-1}) P(s_m, \mathbf{r}_m | s_{m-1}),\\ &= \sum_{s_{m-1}} \alpha(s_{m-1})\gamma(s_{m-1}, s_m). \qquad (2.42) \end{aligned}$$

Starting with the zero state, the forward recursion term is initialized as

$$\alpha(s_0) = \begin{cases} 1 & \text{for} \quad s_0 = 0, \\ 0 & \text{for} \quad s_0 = s, \qquad s = 1, 2, \ldots, S_{\text{in}} - 1. \end{cases} \qquad (2.43)$$

For the reverse recursion term,

$$\begin{aligned}
\beta(s_m) &= \sum_{s_{m+1}} P(s_{m+1}, \mathbf{r}_{m+1}^{L_u} | s_m) \\
&= \sum_{s_{m+1}} P(s_{m+1}, \mathbf{r}_{m+1} | s_m) P(\mathbf{r}_{m+2}^{L_u} | s_m, s_{m+1}, \mathbf{r}_{m+1}) \\
&= \sum_{s_{m+1}} P(s_{m+1}, \mathbf{r}_{m+1} | s_m) P(\mathbf{r}_{m+2}^{L_u} | s_{m+1}) \\
&= \sum_{s_{m+1}} \gamma(s_m, s_{m+1}) \beta(s_{m+1}). \qquad (2.44)
\end{aligned}$$

Assuming that the trellis is terminated at the zero state, the reverse recursion term is initialized as

$$\beta(s_{L_u}) = \begin{cases} 1 & \text{for} \quad s_{L_u} = 0, \\ 0 & \text{for} \quad s_{L_u} = s, \qquad s = 1, 2, \ldots, S_{\text{in}} - 1. \end{cases} \qquad (2.45)$$

The BCJR algorithm first performs the the initializations in (2.43) and (2.45). Then $\gamma(s_{m-1}, s_m)$ and $\alpha(s_m)$ are computed depending on (2.39) and (2.42), respectively, while the channel outputs are being received, and are stored throughout the forward recursion. After the entire sequence $\mathbf{r}_1^{L_u}$ is received, the $\beta(s_m)$ terms are computed by applying the reverse recursion in (2.44). Then, $L(\tilde{u}_m)$ is computed as in (2.37) and the extrinsic information $L_e(\tilde{u}_m)$ in (2.41) is obtained by subtracting $L_a(\tilde{u}_m)$ from $L(\tilde{u}_m)$ and is used as the soft output (reliability information) by the outer decoder.

The Log-BCJR algorithm carries the expressions above to the logarithmic domain so that

$$\tilde{\alpha}(s_m) := \log \alpha(s_m), \qquad (2.46)$$

$$\tilde{\gamma}(s_{m-1}, s_m) := \log \gamma(s_{m-1}, s_m), \qquad (2.47)$$

$$\tilde{\beta}(s_m) := \log \beta(s_m) \qquad (2.48)$$

where

$$\tilde{\alpha}(s_m) = \log \sum_{s_{m-1}} e^{\,\tilde{\alpha}(s_{m-1})+\tilde{\gamma}(s_{m-1},s_m)}, \tag{2.49}$$

$$\tilde{\beta}(s_m) = \log \sum_{s_{m+1}} e^{\,\tilde{\beta}(s_{m+1})+\tilde{\gamma}(s_m,s_{m+1})}. \tag{2.50}$$

Then the extrinsic information $L_e(\tilde{u}_m)$, $m = 1, 2 \ldots, L_u$, in (2.41) is computed by the Log-BCJR algorithm as

$$L_e(\tilde{u}_m) = \underbrace{\log \frac{\sum_{S(\tilde{u}:\tilde{u}_m=+1)} e^{\tilde{\alpha}(s_{m-1})+\tilde{\gamma}(s_{m-1},s_m)+\tilde{\beta}(s_m)}}{\sum_{S(\tilde{u}:\tilde{u}_m=-1)} e^{\tilde{\alpha}(s_{m-1})+\tilde{\gamma}(s_{m-1},s_m)+\tilde{\beta}(s_m)}}}_{L(\tilde{u}_m)} - L_a(\tilde{u}_m). \tag{2.51}$$

The soft information $L(u_m)$ for the outer decoder is found by deinterleaving $L_e(\tilde{u}_m)$. As shown in Figure 2.1, the outer decoder produces the LLRs $L(b_i)$ and $L_e(u_m)$ as the reliability information for the data bit $b_i$ and the code bit $u_m$, respectively. The *a priori* information for the data bits is zero so that $P(b_i = +1) = P(b_i = -1) = 0.5$ and, therefore, $L_a(b_i) = 0$. Similar to (2.51), the outer decoder computes $L(b_i)$, $i = 1, 2, \ldots, L_b$, by using the Log-BCJR algorithm as

$$L(b_i) = \log \frac{\sum_{S(b:b_i=+1)} e^{\tilde{\alpha}(s_{i-1})+\tilde{\gamma}(s_{i-1},s_i)+\tilde{\beta}(s_i)}}{\sum_{S(b:b_i=-1)} e^{\tilde{\alpha}(s_{i-1})+\tilde{\gamma}(s_{i-1},s_i)+\tilde{\beta}(s_i)}} \tag{2.52}$$

where

$$\begin{aligned} \tilde{\gamma}(s_{i-1}, s_i) &= \log P(s_i, \mathbf{u}_k | s_{i-1}) = \log P(\mathbf{u}_i | s_{i-1}) P(s_k | s_{k-1}) \\ &= \log P(\mathbf{u}_i) + \log P_a(b_i) \end{aligned} \tag{2.53}$$

with

$$\log P(\mathbf{u}_i) = \sum_{\ell=1}^{m_o} \log P(u_{m_o(i-1)+\ell}). \tag{2.54}$$

Using the property that $u_m \in \{-1, +1\}$, a new quantity can be defined as

$$\begin{aligned} \log^* P(u_m) &:= \log P(u_m) - \frac{1}{2}\log P(u_m = +1) - \frac{1}{2}\log P(u_m = -1) \\ &= \frac{1}{2} u_m \log \frac{P(u_m = +1)}{P(u_m = -1)} \\ &= \frac{1}{2} u_m L(u_m) \end{aligned} \tag{2.55}$$

for $m = 1, 2, \ldots, L_u$. Similarly, it is found that

$$\log^* P_a(b_i) := \frac{1}{2} b_i L_a(b_i) = 0, \qquad i = 1, 2, \ldots, L_b. \tag{2.56}$$

Using the representations in (2.55) and (2.56), (2.53) can be modified as

$$\begin{aligned} \tilde{\gamma}(s_{i-1}, s_i) &= \sum_{\ell=1}^{m_o} \log^* P(u_{m_o(i-1)+\ell}) + \log^* P_a(b_k) \\ &= \frac{1}{2} \sum_{\ell=1}^{m_o} u_{m_o i - m_o + \ell} L(u_{m_o(i-1)+\ell}). \end{aligned} \tag{2.57}$$

Employing the new $\tilde{\gamma}(s_{i-1}, s_i)$ term above does not result in any change in the value of $L(b_i)$ since such a modification yields that the same quantities are subtracted from the exponents at both the numerator and the denominator of the LLR in (2.52). Using the representation in (2.57), it is found that

$$L(b_i) = \frac{\sum_{S(b:b_i=+1)} e^{\tilde{\alpha}(s_{i-1}) + \frac{1}{2}\sum_{\ell=1}^{m_o} u_{m_o i - m_o + \ell} L(u_{m_o i - m_o + \ell}) + \tilde{\beta}(s_i)}}{\sum_{S(b:b_i=-1)} e^{\tilde{\alpha}(s_{i-1}) + \frac{1}{2}\sum_{\ell=1}^{m_o} u_{m_o i - m_o + \ell} L(u_{m_o i - m_o + \ell}) + \tilde{\beta}(s_i)}}. \tag{2.58}$$

Furthermore, the extrinsic information for the $(m_o i - m_o + j)$th outer code bit is computed as

$$L_e(u_{m_o i - m_o + j}) = \frac{\sum_{S(\mathbf{u}:\mathbf{u}_i(j)=+1)} e^{\tilde{\alpha}(s_{i-1}) + \frac{1}{2}\sum_{\ell \neq j} u_{m_o i - m_o + \ell} L(u_{m_o i - m_o + \ell}) + \tilde{\beta}(s_i)}}{\sum_{S(\mathbf{u}:\mathbf{u}_i(j)=-1)} e^{\tilde{\alpha}(s_{i-1}) + \frac{1}{2}\sum_{\ell \neq j} u_{m_o i - m_o + \ell} L(u_{m_o i - m_o + \ell}) + \tilde{\beta}(s_i)}} \tag{2.59}$$

where $i = 1, \ldots, L_b$, $j = 1, \ldots, m_o$, and $S(\mathbf{u} : \mathbf{u}_i(j) = +1)$ denotes the transitions from $s_{i-1}$ to $s_i$ generating the codewords with the $j$th bit being equal to $+1$. The

representation in (2.57) enables the direct use of the LLRs at the input of the decoder while computing the forward and reverse recursion terms and the reliability information in (2.58) and (2.59). As shown in Figure 2.1, turbo decoding is performed by exchanging the corresponding LLRs for the outer code bits between the inner and outer decoder. After several number of iterations, estimates for the data bit are found by taking the sign of the LLRs in (2.58).

### 2.2.2. Demodulation of CPM Using Log-BCJR Algorithm

As described in Section 2.1.1, the CPM modulator can be decomposed into the CPE and MM blocks, where the CPE is represented by a time-invariant trellis and is equivalent to a convolutional encoder [6]. Then the system model in Figure 2.1 is also applicable for coded CPM where the CPM modulation and demodulation operations are assigned to the inner encoder and decoder blocks, respectively. After the interleaving at the transmitter, the outer code bits, $\{\tilde{u}_m\}$, are divided into $N_c = L_u/m_c$ subsets where $m_c = \log_2 M$. The $\ell$th subset denoted as $\tilde{\mathbf{u}}_\ell = \{\tilde{u}_{m_c\ell-m_c+1}, \tilde{u}_{m_c\ell-m_c+2}, \ldots, \tilde{u}_{m_c\ell}\}$ is mapped to $\tilde{x}_\ell$ where $\tilde{x}_\ell \in \{0, 1, \ldots, M-1\}$ and $\ell = 1, \ldots, N_c$. The $M$-ary symbols are exploited by the CPE to perform the phase modulation in (2.16) and the MM compensates for the frequency shift in (2.14) to produce $c(t, \mathbf{x}_1^{N_c})$. After the transmission through the AWGN channel, the received signal is represented as

$$r(t) = c(t, \mathbf{x}_1^{N_c}) + v(t), \qquad 0 \le t \le N_c T \tag{2.60}$$

where $v(t)$ is the zero-mean complex AWGN. After ideal low-pass filtering with a two-sided bandwidth of $1/T_s$ Hertz, the discrete representation for the received signal is obtained by sampling the filter output every $T_s = T/n_s$ seconds where $T_s$ is adjusted properly to prevent aliasing while maintaining the whiteness of the additive noise [10]. The discrete-time signal is found as

$$r_n = c_n + v_n, \qquad n = 0, 1, \ldots, n_s N_c - 1 \tag{2.61}$$

where $r_n := r(nT_s)$, $c_n := c(nT_s, \mathbf{x}_1^{N_c})$, and $v_n := v(nT_s)$. Applying the frequency shift in (2.14), the tilted-phase representation is computed as

$$\tilde{r}_n := r_n e^{j\pi h(M-1)n/n_s} = y_n + \tilde{v}_n, \qquad n = 0, 1, \ldots, n_s N_c - 1, \tag{2.62}$$

where $y_n := y(nT_s, \mathbf{x}_1^{N_c})$ and $\tilde{v}_n = v_n e^{j\pi h(M-1)n/n_s}$ is the AWGN term with zero mean and variance being equal to $\sigma_v^2$. The received and actual discrete-time tilted-phase CPM signals at the $\ell$th symbol interval are represented as $\tilde{\mathbf{r}}_\ell$ and $\mathbf{y}_\ell$, respectively, where $\tilde{\mathbf{r}}_\ell(i) = \tilde{r}_{n_s\ell - n_s + i}$ and $\mathbf{y}_\ell(i) = y_{n_s\ell - n_s + i}$ denote the sampling values at time instant $(n_s\ell - n_s + i)T_s$ for $\ell = 1, 2, \ldots, N_c$ and $i = 0, 1, \ldots, n_s - 1$. The $i$th discrete-time signal at each symbol interval belong to the finite-alphabet $\mathcal{Y}_i = \{Y_{i,0}, Y_{i,1}, \ldots, Y_{i,\tilde{S}}\}$ where $i = 0, 1, \ldots, n_s - 1$ and $Y_{i,p}$ is the value of the $p$th tilted-phase CPM signal at time instant $iT_s$ over the symbol interval $[0, T]$. Assuming that the $p$th tilted-phase CPM signal is generated during the state transition from $s_{\ell-1}$ to $s_\ell$ in the CPE trellis, the inner decoder compute $\tilde{\gamma}(s_{\ell-1}, s_\ell)$ as

$$\begin{aligned} \tilde{\gamma}(s_{\ell-1}, s_\ell) &= \log P(\tilde{\mathbf{r}}_\ell | \mathbf{y}_\ell) + \log^* P(\tilde{\mathbf{u}}_\ell) \\ &= \log P(\tilde{\mathbf{r}}_\ell | \mathbf{y}_\ell) + \frac{1}{2} \sum_{i=1}^{m_c} \tilde{u}_{m_c\ell - m_c + i} L(\tilde{u}_{m_c\ell - m_c + i}) \end{aligned} \tag{2.63}$$

where

$$P(\tilde{\mathbf{r}}_\ell | \mathbf{y}_\ell) = \frac{1}{(\pi\sigma_v^2)^{n_s}} e^{-\frac{1}{\sigma_v^2} \sum_{i=0}^{n_s-1} |\tilde{\mathbf{r}}_\ell(i) - Y_{i,p}|^2}. \tag{2.64}$$

Using (2.63), the extrinsic information for the $(m_c\ell - m_c + j)$th outer code bit is calculated as

$$L_e(\tilde{u}_{m_c\ell - m_c + j}) = \frac{\sum_{S(\tilde{\mathbf{u}}: \tilde{\mathbf{u}}_\ell(j) = +1)} e^{\tilde{\alpha}(s_{\ell-1}) + \log P(\tilde{\mathbf{r}}_\ell | \mathbf{y}_\ell) + \frac{1}{2} \sum_{i \neq j} \tilde{u}_{m_c\ell - m_c + i} L(\tilde{u}_{m_c\ell - m_c + i}) + \tilde{\beta}(s_\ell)}}{\sum_{S(\tilde{\mathbf{u}}: \tilde{\mathbf{u}}_\ell(j) = -1)} e^{\tilde{\alpha}(s_{\ell-1}) + \log P(\tilde{\mathbf{r}}_\ell | \mathbf{y}_\ell) + \frac{1}{2} \sum_{i \neq j} \tilde{u}_{m_c\ell - m_c + i} L(\tilde{u}_{m_c\ell - m_c + i}) + \tilde{\beta}(s_\ell)}} \tag{2.65}$$

where $\ell = 1, \ldots, N_c$ and $j = 1, 2, \ldots, m_c$. Here $S(\tilde{\mathbf{u}} : \tilde{\mathbf{u}}_\ell(j) = +1)$ denotes the state transitions where the $j$th bit $\tilde{u}_{m_c\ell - m_c + j}$ in the bit sequence $\tilde{\mathbf{u}}_\ell$ that is mapped to the $M$-ary transition symbol $\tilde{x}_\ell$ is equal to $+1$. For binary CPM where $M = 2$ and $m_c = 1$,

the LLR in (2.65) simplifies to

$$L_e(\tilde{u}_\ell) = \frac{\sum_{S(\tilde{u}:\tilde{u}_\ell=+1)} e^{\tilde{\alpha}(s_{\ell-1})+\log P(\tilde{\mathbf{r}}_\ell|\mathbf{y}_\ell)+\tilde{\beta}(s_\ell)}}{\sum_{S(\tilde{u}:\tilde{u}_\ell=-1)} e^{\tilde{\alpha}(s_{\ell-1})+\log P(\tilde{\mathbf{r}}_\ell|\mathbf{y}_\ell)+\tilde{\beta}(s_\ell)}} \tag{2.66}$$

where $\ell = 1, \ldots, L_u$.

### 2.2.3. Convergence Analysis using EXIT Charts

The EXIT chart is proposed as a semi-analytical tool in [46] to determine the convergence behavior of a turbo receiver where the extrinsic information is exchanged between the receiver components in the form of LLRs as in Figure 2.1. In the EXIT chart analysis, the receiver modules are modelled as mapping devices transferring input LLRs to the output LLRs and the exchange of extrinsic information is visualized as a decoding trajectory between the transfer functions of the constituent modules.

In [46], it is determined by the simulations that the extrinsic LLRs produced by the decoders at a turbo receiver have a distribution that approaches to Gaussian as the number of iterations increases. Depending on the information exchange, the extrinsic outputs from one decoder become the *a priori* inputs for the constituent decoder. It is also observed that increasing the interleaver size reduces the correlations between the input LLRs and yields better separation of the decoders. Motivated by these results, an AWGN channel model is used to represent the *a priori* information for each decoder. Depending on this model, it is assumed that an independent Gaussian random variable $v$ with zero mean and variance being equal to $\sigma_v^2$ is added to $x$ yielding $r = x + v$ where $x$ is the bit information that the input LLR is associated with. The conditional probability density function (pdf) for $r$ is denoted as

$$P(r|x) = \frac{1}{\sqrt{2\pi\sigma_v^2}} e^{-\frac{|r-x|^2}{2\sigma_v^2}} \tag{2.67}$$

where $x \in \{-1, +1\}$. Using (2.67), the LLR is computed as

$$\mathcal{L} = \log \frac{P(r|x=+1)}{P(r|x=-1)} = \frac{2}{\sigma_v^2} r = \frac{2}{\sigma_v^2}(x+v) \tag{2.68}$$

which is a Gaussian random variable with mean and variance being equal to $2x/\sigma_v^2$ and $4/\sigma_v^2$, respectively, assuming that $x$ is given. Defining $\sigma_{\mathcal{L}}^2 := 4/\sigma_v^2$, the analysis in [46] shows that the input LLRs can be assumed to be independent and identically distributed (i.i.d.) random variables with a single parameter ($\sigma_{\mathcal{L}}$) conditional pdf denoted as

$$P(\mathcal{L}|x) = \frac{1}{\sqrt{2\pi\sigma_{\mathcal{L}}^2}} e^{-\frac{|\mathcal{L}-\sigma_{\mathcal{L}}^2 x/2|^2}{2\sigma_{\mathcal{L}}^2}}. \tag{2.69}$$

In the EXIT chart analysis, the input LLRs (which are $\{L_a(\tilde{u}_m)\}$ and $\{L(u_m)\}$ for the inner and outer decoder in Figure 2.1, respectively) are generated as i.i.d. random variables as in (2.68) according to the Gaussian distribution in (2.69) for a given bit sequence ($x = \tilde{u}_m$ and $x = u_m$ for the inner and outer decoders in Figure 2.1, respectively) and $\sigma_{\mathcal{L}}$ value [46]. For the inner decoder in Figure 2.1, the channel outputs $\{r_n\}$ in (2.30) are also generated for a given signal-to-noise ratio (SNR) depending on the Gaussian model in (2.36). Then the artificially generated LLRs are used as the *a priori* information by the corresponding decoder (in conjunction with the channel outputs for the inner decoder) while producing the output information. The distribution for the output LLRs are determined experimentally by using the histogram measurements. For different values of $\sigma_{\mathcal{L}}$, the mutual information between the bits and the LLRs is computed at both the input and output of each decoder as [46]

$$\begin{aligned} I(\mathcal{L};x) &= \frac{1}{2} \sum_{b=-1,+1} \int_{-\infty}^{+\infty} P(\mathcal{L}|x=b) \\ &\times \log_2 P(\mathcal{L}|x=b) \frac{2P(\mathcal{L}|x=b)}{P(\mathcal{L}|x=-1) + P(\mathcal{L}|x=+1)} d\mathcal{L} \end{aligned} \tag{2.70}$$

where the pdf in (2.69) and the pdf found by histogram measurements are plugged into (2.70), respectively, and $0 \leq I(\mathcal{L};x) \leq 1$. Then the transfer characteristic curve of each

decoder is determined separately as a mapping function between the input and output mutual information. For the turbo receiver in Figure 2.1, the transfer characteristic curve for the inner decoder and the inverse of the transfer characteristic curve for the outer decoder constitute the corresponding EXIT chart, where the decoding trajectory of the receiver is visualized as a zigzag path confined between these curves. Using the EXIT chart analysis, it is possible to observe the three typical scenarios for the BER performance of a turbo receiver [46]. 1) The decoder transfer characteristics intersect at low mutual information with the trajectory getting stuck. This corresponds to high BER and negligible turbo gain at the receiver which is observed especially at low SNRs. 2) There is a narrow tunnel (or bottleneck) between the transfer curve and the inverse transfer curve so that the trajectory does not stuck. In this case, the convergence to low BERs is slow but possible since the decoder transfer characteristics do not intersect anymore. The SNR value that overcomes the intersection is referred to as the SNR threshold of the turbo receiver. 3) In the EXIT chart, a wide-open region is observed between the transfer curve and the inverse transfer curve at high SNRs, which allows the fast convergence of the trajectory. This behavior is observed as a water fall in the BER performance plot of a turbo receiver.

### 2.2.4. Convergence Analysis for Iterative Demodulation of CPM

In this section, the convergence analysis for the turbo demodulation and decoding of coded CPM on AWGN channel is presented using EXIT charts. Furthermore, it is shown that the simulation results for the BER performance match the outcomes of the corresponding EXIT chart analysis. The turbo demodulation and decoding of coded CPM is applied as described in Section 2.2.2 where the inner and outer decoders in Figure 2.1 are considered as the CPM demodulator and channel decoder, respectively. In both the convergence analysis and the BER simulations, the binary 3RC CPM scheme of [2] with the main lobe width of $L$ symbol duration is employed where $L = 3$ and $h = 0.5$. A low-pass filter with a two-sided bandwidth of $2/T$ is applied at the reciever so that more than 99.9 percent of the signal energy is recovered [2]. Then the filter output is sampled to obtain the discrete-time representation in (2.61) where the number of samples per symbol is $n_s = 2$ and the sampling period is $T_s = T/2$.

A rate-1/2 convolutional code with generator polynomial $(64, 74)_8$ is used for channel coding [64]. In the BER simulations, random interleaving is applied and the length of the outer code bit sequence used for CPM modulation is 256.

In Figure 2.1, the inner decoder for CPM demodulation transforms the *a priori* information $\{L_a(\tilde{u}_m)\}$ for the interleaved code bits from the channel decoder to $\{L_e(\tilde{u}_m)\}$, given the received signal from the AWGN channel. In order to determine

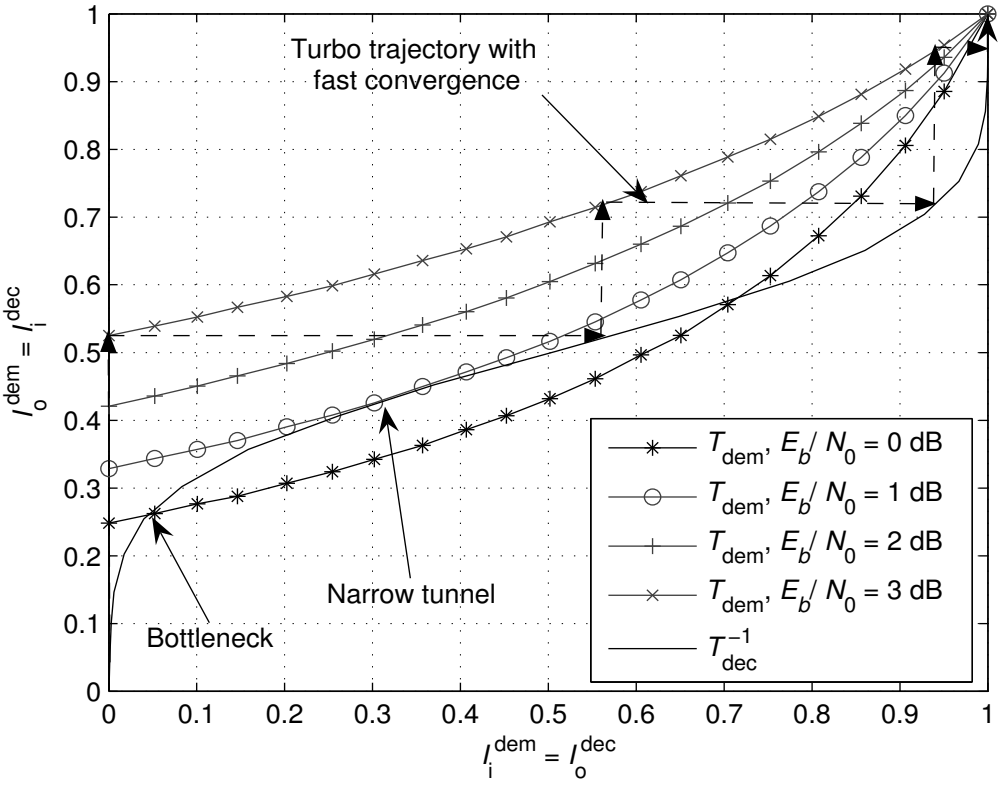



Figure 2.2. Receiver EXIT charts for the turbo demodulation and decoding of coded CPM

the EXIT chart for the demodulator, the input LLRs $\{L_a(\tilde{u}_m)\}$ are generated artificially given $\{\tilde{u}_m\}$ depending on the model in (2.68), and the values for the input mutual information $I_{\mathrm{i}}^{\mathrm{dem}} = I(L_a(\tilde{u}_m); \tilde{u}_m)$ are computed as in (2.70) using the conditional PDF in (2.69) belonging to this model, where $\mathcal{L} = L_a(\tilde{u}_m)$ and $x = \tilde{u}_m$. The artificially-generated $\{L_a(\tilde{u}_m)\}$ are exploited by the CPM demodulator to generate $\{L_e(\tilde{u}_m\}$ as described in Section 2.2.2. After the conditional PDF for $\{L_e(\tilde{u}_m\}$ is determined by the histogram measurements, the output mutual information $I_{\mathrm{o}}^{\mathrm{dem}} = I(L_e(\tilde{u}_m); \tilde{u}_m)$ is computed in the same way employed to find $I_i$. Thus, the transfer characteristics of

the demodulator can be denoted as $I_{\mathrm{o}}^{\mathrm{dem}} = T_{\mathrm{dem}}(I_{\mathrm{i}}^{\mathrm{dem}}|\sigma_v^2)$ where $T_{\mathrm{dem}}(.|.)$ denotes the transfer characteristic function for the demodulator which convert $I_{\mathrm{i}}^{\mathrm{dem}}$ to $I_{\mathrm{o}}^{\mathrm{dem}}$ given the variance $\sigma_v^2$ for the AWGN. Similar procedure can be applied for the outer decoder used for the channel decoding where the transfer characteristic function for the channel decoder is denoted as $T_{\mathrm{dec}}(.)$ where $I_{\mathrm{o}}^{\mathrm{dec}} = T_{\mathrm{dec}}(I_{\mathrm{i}}^{\mathrm{dec}})$, and $I_{\mathrm{i}}^{\mathrm{dec}}$ and $I_{\mathrm{o}}^{\mathrm{dec}}$ are the input and output mutual information for the channel decoder, respectively.

The EXIT chart for the turbo receiver under different SNR scenarios is shown

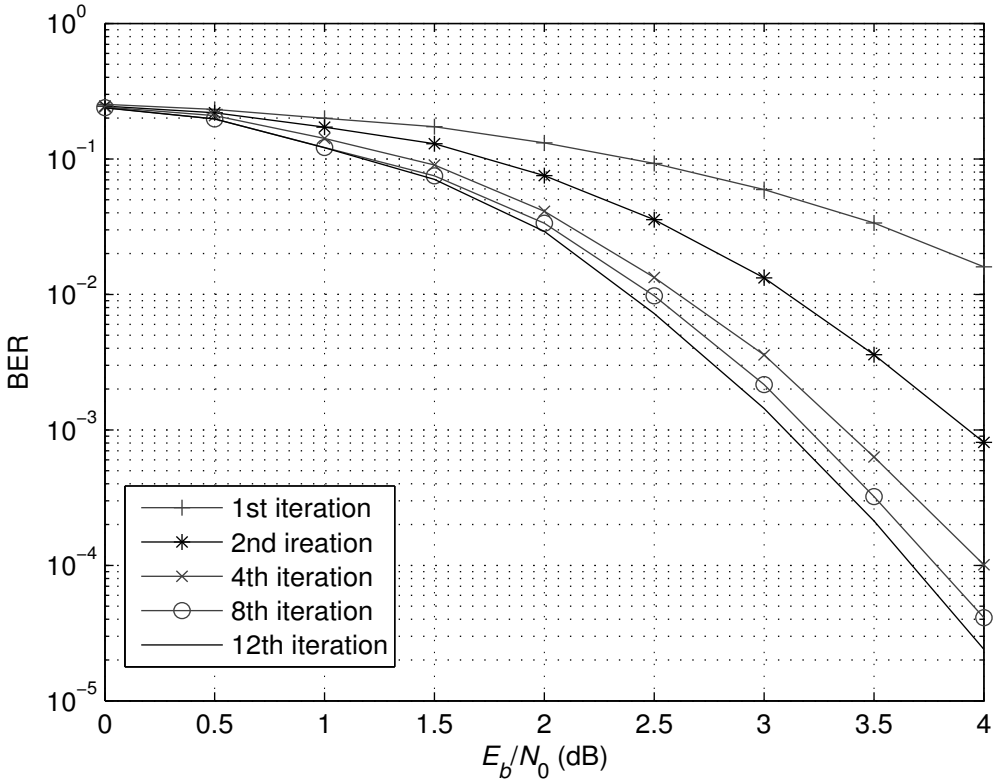



Figure 2.3. BER performance for the turbo demodulation and decoding of coded CPM

in Figure 2.2. A bottleneck is observed at $E_b/N_0 = 0$ dB so that the turbo trajectory gets stuck and the convergence is not possible. At $E_b/N_0 = 1$ dB, a narrow tunnel is observed so that the convergence is possible after performing many iterations. After $E_b/N_0 = 1$ dB, there is a huge gap between the demodulator and decoder characteristics curves which corresponds to the fast convergence and a water fall behavior in the BER performance as described in Section 2.2.3.

In Figure 2.3, the BER performance of the turbo receiver for the joint demodulation and decoding of coded CPM on AWGN channel is illustrated where twelve iterations are executed between the demodulator and the decoder. There is no considerable turbo gain before $E_b/N_0 = 1$ dB and a water fall behavior is observed after $E_b/N_0 = 1$ dB, which are consistent with the results observed in the EXIT chart analysis.

# 3. DOUBLE TURBO EQUALIZATION OF CPM WITH TIME DOMAIN PROCESSING

For coded data over narrowband channels, the channel encoding and CPM modulation operations are viewed as the serial concatenation of two finite state machines separated by an interleaver, and joint demodulation and decoding is performed iteratively by the soft information exchange between a SISO CPM demodulator and a SISO channel decoder [8]. Similarly, in the presence of multipath fading, one can couple the CED described in Section 1.2 with the back-end channel decoder to implement a turbo-type receiver which can be named as turbo APP equalizer (TAE). However, CED employs a single super trellis for optimal joint equalization/demodulation [10] where the size of the joint trellis is prohibitively large when the modulation and/or channel memory is long, making even non-iterative equalization practically unwieldy. For this reason, a suboptimal but low-complexity receiver is proposed in this chapter for the turbo equalization of CPM over multipath fading channels, which relies on separating the channel equalization, CPM demodulation, and channel decoding operations, and on employing a doubly-iterative processing scheme where the demodulator is coupled with either the equalizer or the decoder alternatively.

The proposed receiver consists of a SIC/MMSE time-domain equalizer at its front-end, a central SISO CPM demodulator and a SISO channel decoder at its back-end. Both the demodulator and the decoder can be implemented by the Log-BCJR algorithm [62] as in the aforementioned turbo processing applications mentioned at the beginning of Section 1.2 for linear constellations. On the other hand, the SIC/MMSE equalizer design is not a direct extension of its counterparts for linear modulation as inherent characteristics of CPM such as non-linearity and modulation memory must be taken into consideration. For instance, the transmitted signals are often assumed uncorrelated in receiver design for linearly modulated signals, which is not the case in CPM due to its non-linearity and the number of symbols correlated with each other is determined by the modulation memory. Therefore, the equalizer design has to include

the successive symbol correlations whose direct computation is difficult, but possible with Laurent's decomposition [48] of binary CPM as in (2.9) which can also be extended for $M$-ary CPM as described in [52]. The proposed receiver uses the doubly-iterative structure for the joint equalization, demodulation, and decoding, where each front-end iteration for SIC/MMSE equalization is followed by several back-end iterations for CPM demodulation and channel decoding to improve *a priori* information for the next front-end iteration. Two and three-dimensional EXIT charts as in [47] are used to analyze the convergence behavior of the proposed doubly serially concatenated receiver. In addition, bit error rate (BER) performance is simulated under different channel conditions and with different receiver configurations. Both the EXIT charts and the simulation results indicate that performing a few back-end demodulation/decoding iterations within each front-end equalization iteration not only yields faster convergence to low BERs but also reduces the overall computational complexity by reducing the number of equalization passes.

The organization of this chapter is as follows. In Section 3.1, structure of the transmitter and the discrete-time signal representation employed at the receiver are described first. Remainder of the section consecutively presents the doubly-iterative architecture, SIC/MMSE equalization algorithm, and complexity comparisons of the proposed and conventional methods. In Section 3.2, convergence behavior of the doubly-iterative receiver is analyzed. The simulation results are presented in Section 3.3.

## 3.1. Doubly-Iterative Equalization with Time Domain Processing

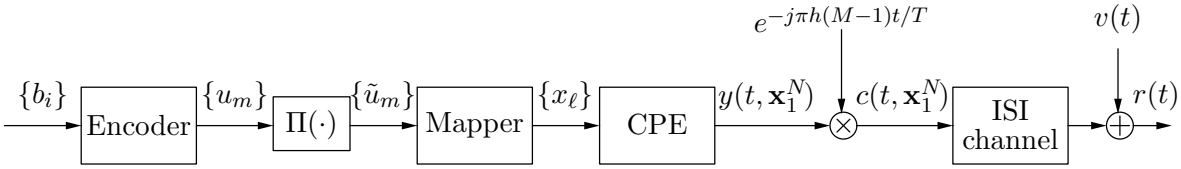



Figure 3.1. The transmitter for the bit-interleaved coded CPM and the channel

At the transmitter in Figure 3.1 where $\Pi(\cdot)$ denotes the interleaving operation, a length-$L_b$ data bit sequence with elements $b_i \in \{0, 1\}$, $i = 1, \ldots, L_d$, is encoded by a rate-$L_b/L_u$ convolutional code to form $u_m \in \{-1, +1\}$ where $m = 1, \ldots, L_u$. Then, $u_m$ are interleaved to $\tilde{u}_m$, which are mapped onto the $M$-ary symbols $x_\ell$ defined

in Section 2.1.1 where $\ell = 1, \ldots, N$ with $N = L_u/\log_2 M$. To produce the tilted-phase signal in (2.14), the CPE applies the phase modulation in (2.16) where $\tilde{x}_\ell = (x_\ell + M - 1)/2$ as described in Section 2.1.1. At the output of CPE, the MM operation is employed to convert the tilted-phase signal to the CPM signal depending on the relation in (2.14) where $y(t, \mathbf{x}_1^N)$ is multiplied with $e^{-j\pi h(M-1)t/T}$ as shown in Figure 3.1. After the transmission through the ISI channel, the signal in (2.25) is received at the baseband. The number of matched filters for the optimal detection of CPM is $M^L$ as described at the beginning of Section 2.1.2. However, it is also possible to obtain a discrete representation for detection by appropriate low-pass filtering and sampling of the received signal rather than applying a bank of matched filters with high complexity. After ideal low-pass filtering with a two-sided bandwidth of $1/T_s$ Hertz, the discrete representation for the received signal is obtained by sampling the filter output every $T_s = T/n_s$ seconds where $T_s$ is adjusted properly to prevent aliasing while maintaining the whiteness of the additive noise [10]. The discrete-time signal obtained from the received signal in (2.25) is denoted as

$$r_n = \sum_{l=0}^{L_c-1} \tilde{h}_l c_{n-l} + v_n, \qquad n = 0, 1, \ldots, \tilde{N} - 1, \tag{3.1}$$

where $r_n := r(nT_s)$, $c_n := c(nT_s, \mathbf{x}_1^N)$, $v_n := v(nT_s)$, and $\tilde{N} := n_s N$.

### 3.1.1. Receiver Overview

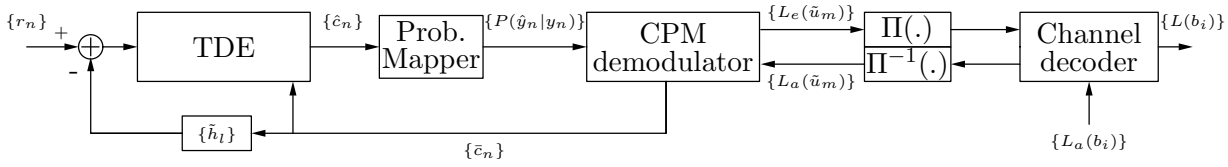



Figure 3.2. Doubly-iterative receiver with TDE

The doubly-iterative receiver consists of three serially concatenated blocks as shown in Figure 3.2, where $\Pi^{-1}(\cdot)$ is the deinterleaving operation, $y_n$ denotes the $n$th sample for the CPM tilted-phase signal, $\bar{c}_n$ is the mean-value of the $n$th CPM signal sample, $\hat{c}_n$ and $\hat{y}_n$ stand for the $n$th equalizer output for the CPM signal and its equivalent for the tilted-phase CPM signal, respectively, $L_a(\tilde{u}_m)$ and $L_e(\tilde{u}_m)$ denote

the *a priori* and extrinsic LLRs for the interleaved code bits, $\{L_a(b_i)\}$ are the *a priori* LLRs for the data bits which are always zero, and $\{L(b_i)\}$ are the output LLRs used for the data bit decisions. Initially, because no *a priori* information is available for any of the receiver blocks, the equalization iteration starts with the MMSE equalization without the soft interference cancellation. Each discrete-time symbol at the output of this process is then mapped onto a $\tilde{S}$-ary vector of extrinsic probabilities on the CPM signals with tilted phase where $\tilde{S} = \mathcal{P}M^L$ as described in Section 2.1.1. This vector forms the input for the back-end demodulation/decoding iteration between the CPM demodulator and the channel decoder both implemented by the Log-BCJR algorithm as described in Section 2.2. The central CPM demodulator is capable of generating soft information on both the interleaved code bits $\{\tilde{u}_m\}$ in the form of LLRs $\{L_e(\tilde{u}_m)\}$ and the discrete-time CPM symbols $\{c_n\}$ in the form of $\tilde{S}$-ary extrinsic probability vectors. The former is used within the soft-information exchange of the back-end iteration, where the latter can be used to compute the expected values $\{\bar{c}_n\}$ to be fed-back to the front-end SIC/equalizer after any number of back-end iterations as the *a priori* information to start the next equalization iteration. The doubly-iterative processing is achieved by this dual coupling of the demodulator with both the equalizer and the decoder. Aforementioned expected interference is not computed using the extrinsic information for the encoded bits from either the demodulator or decoder because the mean values for the discrete-time CPM symbols obtained by exploiting the bit probabilities over the demodulator trellis quickly converge to zero, as shown in Appendix A, and no soft interference cancellation takes place.

The demodulator is implemented by the Log-BCJR algorithm as in Section 2.2.2 where soft outputs are generated on both interleaved code bits and tilted-phase CPM signals for the use of the channel decoder and the front-end equalizer, respectively. The extrinsic information on the interleaved code bits is found as in (2.65) which leads to

$$L_e(\tilde{u}_{m_c\ell-m_c+j}) = \frac{\sum_{S(\tilde{\mathbf{u}}:\tilde{\mathbf{u}}_\ell(j)=+1)} e^{\tilde{\alpha}(s_{\ell-1})+\log P(\hat{\mathbf{y}}_\ell|\mathbf{y}_\ell)+\frac{1}{2}\sum_{l\neq j}\tilde{u}_{m_c\ell-m_c+l}L(\tilde{u}_{m_c\ell-m_c+l})+\tilde{\beta}(s_\ell)}}{\sum_{S(\tilde{\mathbf{u}}:\tilde{\mathbf{u}}_\ell(j)=-1)} e^{\tilde{\alpha}(s_{\ell-1})+\log P(\hat{\mathbf{y}}_\ell|\mathbf{y}_\ell)+\frac{1}{2}\sum_{l\neq j}\tilde{u}_{m_c\ell-m_c+l}L(\tilde{u}_{m_c\ell-m_c+l})+\tilde{\beta}(s_\ell)}} \tag{3.2}$$

where $\ell = 1, \ldots, N$, $j = 1, 2, \ldots, m_c$, $N = L_u/m_c$, and $m_c = \log_2 M$. Here $\hat{\mathbf{y}}_\ell(i) =$

$\hat{y}_{n_s\ell-n_s+i}$ and $\mathbf{y}_\ell(i) = y_{n_s\ell-n_s+i}$ for $\ell = 1, \ldots, N$, and $i = 0, 1, \ldots, n_s - 1$, and given that the state transition from $s_{\ell-1}$ to $s_\ell$ produces the $p$th tilted-phase CPM signal out of $\tilde{S}$ signals, $P(\hat{\mathbf{y}}_\ell|\mathbf{y}_\ell)$ is found as

$$P(\hat{\mathbf{y}}_\ell|\mathbf{y}_\ell) = \frac{\prod_{i=0}^{n_s-1} P(\hat{y}_{n_s\ell-n_s+i}|y_{n_s\ell-n_s+i} = Y_{i,p})}{\sum_{m=0}^{\tilde{S}-1}\prod_{i=0}^{n_s-1} P(\hat{y}_{n_s\ell-n_s+i}|y_{n_s\ell-n_s+i} = Y_{i,m})} \tag{3.3}$$

where $p = 0, 1, \ldots, \tilde{S} - 1$ and $P(\hat{y}_{n_s\ell-n_s+i}|y_{n_s\ell-n_s+i} = Y_{i,p})$ denotes the extrinsic probability from the equalizer for the $i$th sample at the $\ell$th symbol interval assuming that the $p$th tilted-phase signal is generated by CPE. It is defined in Section 2.2.2 that $Y_{i,p} \in \mathcal{Y}_i$ where $i = 0, 1, \ldots, n_s - 1$. The state transition term in (2.63) is also modified as

$$\tilde{\gamma}(s_{\ell-1}, s_\ell) = \log P(\hat{\mathbf{y}}_\ell|\mathbf{y}_\ell) + \frac{1}{2}\sum_{i=1}^{m_c} \tilde{u}_{m_c\ell-m_c+i} L(\tilde{u}_{m_c\ell-m_c+i}) \tag{3.4}$$

for $\ell = 1, \ldots, N$.

Furthermore, the demodulator produces the soft information on the samples for the tilted-phase CPM signal as

$$P_e(y_{n_s\ell-n_s+i} = Y_{i,p}) = \sum_{S(\mathbf{y}:\mathbf{y}_\ell(i)=Y_{i,p})} e^{\,\tilde{\alpha}(s_{\ell-1})+\frac{1}{2}\sum_{j=1}^{m_c}\tilde{u}_{m_c\ell-m_c+j}L(\tilde{u}_{m_c\ell-m_c+j})+\tilde{\beta}(s_\ell)} \tag{3.5}$$

where $\ell = 1, \ldots, N$, $i = 0, 1, \ldots, n_s - 1$, $p = 0, 1, \ldots, \tilde{S} - 1$ and $S(\mathbf{y} : \mathbf{y}_\ell(i) = Y_{i,p})$ denotes the state transition from $s_{\ell-1}$ to $s_\ell$ that generates the $p$th tilted-phase CPM signal out of $\tilde{S}$ signals. By normalizing (3.5), the sample probabilities are obtained as

$$P(y_{n_s\ell-n_s+i} = Y_{i,p}) = \frac{P_e(y_{n_s\ell-n_s+i} = Y_{i,p})}{\sum_{m=0}^{\tilde{S}-1} P_e(y_{n_s\ell-n_s+i} = Y_{i,m})} \tag{3.6}$$

where $\ell = 1, \ldots, N$, $i = 0, 1, \ldots, n_s - 1$, and $p = 0, 1, \ldots, \tilde{S} - 1$. Then, using the relation in (2.14), the mean values exploited by the SIC and TDE are computed as

$$\bar{c}_{n_s\ell-n_s+i} = e^{-j\pi h(M-1)(n_s\ell-n_s+i)/n_s} \sum_{p=0}^{\tilde{S}-1} Y_{i,p}\, P(y_{n_s\ell-n_s+i} = Y_{i,p}) \tag{3.7}$$

for $\ell = 1, \ldots, N$ and $i = 0, 1, \ldots, n_s - 1$.

The detailed presentation of the operation of the channel decoder using the Log-BCJR algorithm is given in Section 2.2.1. After performing the aforementioned double iterations, the estimates for the data bits are computed by taking the sign of the LLRs in (2.58).

### 3.1.2. SIC/MMSE TDE

Assuming that the MMSE equalization is performed with a time-invariant $L_f$-tap linear filter whose coefficients are collected in the vector at time-$n$ $\mathbf{f}_n$ as

$$\mathbf{f}_n := \begin{bmatrix} f_{n,-F} & f_{n,-F+1} & \ldots & f_{n,0} & \ldots & f_{n,B-1} & f_{n,B} \end{bmatrix}^T \tag{3.8}$$

where $n = 0, 1, \ldots, \tilde{N} - 1$, $F > 0$, $B > 0$, $L_f = F + B + 1$, and defining

$$\begin{aligned} \mathbf{r}_n &= \begin{bmatrix} r_{n+F} & r_{n+F-1} & \ldots & r_{n-B+1} & r_{n-B} \end{bmatrix}^T, \\ \mathbf{c}_n &= \begin{bmatrix} c_{n+F} & \ldots & c_{n+1} & c_n & c_{n-1} & \ldots & c_{n-B-L_c+1} \end{bmatrix}^T, \\ \mathbf{v}_n &= \begin{bmatrix} v_{n+F} & v_{n+F-1} & \ldots & v_{n-B+1} & v_{n-B} \end{bmatrix}^T, \end{aligned} \tag{3.9}$$

we can express the received signal model in block form as

$$\mathbf{r}_n = \tilde{\mathbf{H}}\mathbf{c}_n + \mathbf{v}_n, \tag{3.10}$$

where

$$\tilde{\mathbf{H}} = \begin{bmatrix} \tilde{h}_0 & \ldots & \tilde{h}_{L_c-1} & 0 & \ldots & 0 \\ 0 & \tilde{h}_0 & \ldots & \tilde{h}_{L_c-1} & \ddots & \vdots \\ \vdots & \ddots & \ddots & \ddots & \ddots & 0 \\ 0 & \ldots & 0 & \tilde{h}_0 & \ldots & \tilde{h}_{L_c-1} \end{bmatrix} \tag{3.11}$$

is the $L_f \times (L_f + L_c - 1)$ channel convolution matrix that contains the channel coefficients.

Note that before the equalization, the expected interference computed using the channel matrix in (3.11) and the expected discrete-time CPM signal vector

$$\bar{\mathbf{c}}_n := \left[ \begin{array}{ccccccc} \bar{c}_{n+F} & \dots & \bar{c}_{n+1} & 0 & \bar{c}_{n-1} & \dots & \bar{c}_{n-B-L_c+1} \end{array} \right]^T \tag{3.12}$$

is removed from the received samples in SIC so as to form the following discrete-time signal with reduced interference,

$$\tilde{\mathbf{r}}_n = \tilde{\mathbf{H}} \left[ \mathbf{c}_n - \bar{\mathbf{c}}_n \right] + \mathbf{v_n}. \tag{3.13}$$

In (3.12), the mean value at time $n$ is set as zero to prevent the cancellation of the sample to be detected.

The signal at the output of the MMSE equalizer can be expressed as

$$\hat{c}_n = \mathbf{f}_n^H \left( \tilde{\mathbf{H}} \left[ \mathbf{c}_n - \bar{\mathbf{c}}_n \right] + \mathbf{v}_n \right). \tag{3.14}$$

The equalizer coefficient vector that minimizes the MSE cost function

$$J_{\mathrm{MSE}}(\mathbf{f}) = \mathrm{E} \left[ \left| \mathbf{f}^H \left( \tilde{\mathbf{H}} \left[ \mathbf{c}_n - \bar{\mathbf{c}}_n \right] + \mathbf{v}_n \right) - c_n \right|^2 \right] \tag{3.15}$$

can be computed as

$$\mathbf{f}_n = \left( \tilde{\mathbf{H}} \mathrm{E} \left[ (\mathbf{c}_n - \bar{\mathbf{c}}_n)(\mathbf{c}_n - \bar{\mathbf{c}}_n)^H \right] \tilde{\mathbf{H}}^H + \mathbf{\Sigma}_v \right)^{-1} \mathbf{s} = \left( \tilde{\mathbf{H}} \left[ \mathfrak{R} - \bar{\mathbf{c}}_n \bar{\mathbf{c}}_n^H \right] \tilde{\mathbf{H}}^H + \mathbf{\Sigma}_v \right)^{-1} \mathbf{s} \tag{3.16}$$

where

$$\mathfrak{R} = \mathrm{E}[\mathbf{y}_n \mathbf{y}_n^H] = \begin{bmatrix} \mathcal{R}_0 & \mathcal{R}_1 & \dots & \mathcal{R}_{L_c+L_f-2} \\ \mathcal{R}_1 & \mathcal{R}_0 & \dots & \mathcal{R}_{L_f+L_c-3} \\ \mathcal{R}_2 & \mathcal{R}_1 & \ddots & \mathcal{R}_{L_f+L_c-4} \\ \vdots & \ddots & \ddots & \vdots \\ \mathcal{R}_{L_f+L_c-2} & \dots & \dots & \mathcal{R}_0 \end{bmatrix} \tag{3.17}$$

and $\mathbf{\Sigma}_v$ are the CPM and noise autocorrelation matrices, respectively. In (3.17), $\mathcal{R}_i = \mathcal{R}(iT_s)$ where $\mathcal{R}(\tau)$ denotes the autocorrelation function for the CPM signal in (2.9). Also the $(L_f + L_c - 1) \times 1$ vector $\mathbf{s}$ is

$$\mathbf{s} = \tilde{\mathbf{H}}\mathbf{q} - \tilde{\mathbf{H}}\bar{\mathbf{c}}_n \bar{c}_n^* \tag{3.18}$$

with

$$\mathbf{q} = \mathrm{E}\left[\mathbf{c}_n c_n^*\right] = \begin{bmatrix} \mathcal{R}_F & \dots & \mathcal{R}_1 & \mathcal{R}_0 & \mathcal{R}_1 & \dots & \mathcal{R}_{B+L_c-1} \end{bmatrix}^T. \tag{3.19}$$

Note that in most linear modulation examples, the transmitted symbols are assumed uncorrelated and independent so that $\mathfrak{R} - \bar{\mathbf{c}}_n \bar{\mathbf{c}}_n^H$ reduces to a diagonal matrix as well as $\mathbf{s} = \tilde{\mathbf{H}}^H \begin{bmatrix} \mathbf{0}_{1\times F} \; 1 \; \mathbf{0}_{1\times(B+L_c-1)} \end{bmatrix}^T$ where $\mathbf{0}_{1\times X}$ is an all-zero row vector with length $X$. However, the autocorrelation values for the CPM signals must be taken into account, and each $\mathcal{R}_i$, for $0 \le i \le L_f + L_c - 2$, needs to be re-computed in the presence of different *a priori* information, which also requires the equalizer coefficients to be updated at each time instant.

Note that the computation of the CPM autocorrelations and the matrix inversion in (3.16) make the MMSE equalizer almost as complex as its trellis-based counterpart. To simplify the receiver, time-invariant equalizer coefficients can be computed under either no *a priori* information or complete *a priori* information assumptions as presented in [15]. Under zero *a priori* information (ZAI) assumption, $\bar{c}_i = 0$ for all

$n - B - L_c + 1 \leq i \leq n + F$, and the equalizer vector in (3.16) reduces to

$$\mathbf{f}_{\text{ZAI}} = \left(\tilde{\mathbf{H}}\mathfrak{R}\tilde{\mathbf{H}}^H + \mathbf{\Sigma}_v\right)^{-1}\tilde{\mathbf{H}}\mathbf{q} \tag{3.20}$$

where the autocorrelations $\mathcal{R}_i$ in $\mathfrak{R}$ and $\mathbf{q}$ are computed by using (2.9) for binary CPM which is extended for $M$-ary CPM in [6] and whose derivation is based on uniformly-distributed modulating bits and thus no *a priori* information. In the full *a priori* information (FAI) scenario, $\bar{c}_i = c_i$ for all $n - B - L_c + 1 \leq i \leq n + F$ and the equalizer coefficient vector becomes

$$\mathbf{f}_{\text{FAI}} = \left(\tilde{\mathbf{H}}\mathbf{e}\mathbf{e}^H\tilde{\mathbf{H}}^H + \mathbf{\Sigma}_v\right)^{-1}\tilde{\mathbf{H}}\mathbf{e} \tag{3.21}$$

where $\mathbf{e} = \begin{bmatrix} \mathbf{0}_{1\times F}\ 1\ \mathbf{0}_{1\times(B+L_c-1)} \end{bmatrix}^T$. As presented in the receiver overview, each equalization operation at the front-end is followed by a few back-end CPM demodulation/decoding iterations so that the soft inputs for the equalizer are improved. Thus implementing the equalizer with time-invariant coefficients by assuming no *a priori* information in the initial equalization iterations and then switching to full *a priori* information coefficients in the subsequent iterations is a feasible solution instead of employing the exact implementation of (3.16).

In cases of both the exact and the approximate implementations, extrinsic information for the CPM demodulator needs to be extracted from the MMSE equalizer output. For this purpose, the probability mapper in Figure 3.2 finds the discrete-time representation for the tilted-phase CPM signal using the relation in (2.14) as

$$\hat{y}_n = \hat{c}_n e^{j\pi h(M-1)n/n_s}. \tag{3.22}$$

The equalizer output $\hat{y}_n$ is assumed as the output of an additive Gaussian noise channel with input $y_n$ so that

$$\hat{y}_n = \mu y_n + \upsilon_n \tag{3.23}$$

with $\mu$ as the gain of the symbol to be detected and $\upsilon_n$ as the complex Gaussian noise term [13, 15]. Here, the gain of $c_n$ in (3.14) is expressed as

$$\mu = \mathrm{E}\left[\hat{c}_n c_n^*\right] = \mathbf{f}^H \tilde{\mathbf{H}} \mathrm{E}\left[(\mathbf{c}_n - \bar{\mathbf{c}}_n) c_n^*\right] \tag{3.24}$$

where $\mathrm{E}\left[(\mathbf{c}_n - \bar{\mathbf{c}}_n) c_n^*\right]$ leads to either $\mathbf{q}$ or $\mathbf{e}$ depending on whether the ZAI or FAI information scenario is considered, respectively. Then, the variance of the decision at time $n_s\ell - n_s + i$ is computed as

$$\sigma^2_{n_s\ell - n_s + i} = \sum_{p=0}^{\tilde{S}-1} P_{n_s\ell - n_s + i, p} \left| \hat{y}_{n_s\ell - n_s + i} - \mu Y_{i,p} \right|^2 \tag{3.25}$$

for $\ell = 1, \ldots, N$, and $i = 0, \ldots, n_s - 1$, where all $P_{n_s\ell - n_s + i, p}$ values are set as $1/\tilde{S}$ under ZAI assumption, and the probabilities $P(y_{n_s\ell - n_s + i} = Y_{i,p})$ in (3.6) from the demodulator are taken into account in the FAI scenario so that $P_{n_s\ell - n_s + i, p} = P(y_{n_s\ell - n_s + i} = Y_{i,p})$. Note that the squared distances between the equalizer output and $\tilde{S}$ possible sample values are considered equal-likely under the former assumption, whereas (3.25) reduces to the distance between the equalizer output and the corresponding sample of the transmitted signal for the latter scenario as expected, when the transmitted signal probability is one. Under both assumptions, a time-invariant variance is computed by averaging the instantaneous values over all symbols as

$$\bar{\sigma}^2 = \frac{1}{\tilde{N}} \sum_{n=0}^{\tilde{N}-1} \sigma_n^2. \tag{3.26}$$

Then, using (3.24) and (3.26), the sample probabilities are calculated as

$$P(\hat{y}_{n_s\ell - n_s + i} | y_{n_s\ell - n_s + i} = Y_{i,p}) = \frac{e^{-\frac{|\hat{y}_n - \mu Y_{i,p}|^2}{\bar{\sigma}^2}}}{\sum_{m=0}^{\tilde{S}-1} e^{-\frac{|\hat{y}_n - \mu Y_{i,m}|^2}{\bar{\sigma}^2}}} \tag{3.27}$$

for $\ell = 1, \ldots, N$, $i = 0, 1, \ldots, n_s - 1$, and $p = 0, 1, \ldots, \tilde{S} - 1$, where (3.27) is employed by the CPM demodulator to compute (3.3).

### 3.1.3. Complexity Comparison

The implementation with time-invariant equalizer coefficients is considered here for both the complexity analysis and simulation results. The filtering vectors in (3.20) and (3.21) are time-invariant, and are computed only once to find all the equalizer outputs at each iteration. Thus, the computational load of the SIC/equalizer is very low. At each time instant $n$, the vector $\tilde{\mathbf{H}}\bar{\mathbf{c}}_n$ has to be computed for the interference cancellation. This can be found by using the results of the convolution of the sequence $\{\bar{c}_n\}$ with the channel impulse response $\{h_l\}$, and removing the terms related to the symbol to be found using $\tilde{\mathbf{H}}\left[\begin{array}{ccc}\mathbf{0}_{1\times F} & \bar{c}_n & \mathbf{0}_{1\times(B+L_c-1)}\end{array}\right]^T$. Assuming complex-valued ISI channel coefficients, number of real multiplications and real additions required for these operations are $8L_c$ and $4L_c-2$, respectively, per sample. After the interference cancellation with $2L_f$ real additions, the equalizer filter is applied to obtain the discrete-time output, where the required number of real multiplications and additions for this operation are $4L_f$ and $4L_f-2$, respectively. Then, the total number of real multiplications and additions per equalizer output are $4L_f+8L_c$ and $6L_f+4L_c-4$, respectively. Here, the filter length $L_f$ changes linearly with $L_c$. Thus, considering that $\mathbf{f}$ and the sequence $\{\bar{c}_n\}$ are available as in [15], the computational complexity of the SIC/MMSE equalizer to find each discrete-time output is increasing linearly with $L_c$. Furthermore, since the CPE trellis has $S=\mathcal{P}M^{L-1}$ states with $\tilde{S}=\mathcal{P}M^{L}$ state transitions, the complexity of the CPM demodulator at each trellis instant $\ell$ regarding the computation of $\tilde{\gamma}_(s_{\ell-1},s_\ell)$, $\tilde{\alpha}(s_{\ell-1})$, and $\tilde{\beta}(s_\ell)$ terms as described in Section 2.2 and the soft information in (3.2) and (3.5) is $O(\mathcal{P}M^L)$ per back-end iteration. Thus, the total complexity introduced by the SIC/TDE while computing the equalizer outputs and the CPM demodulator while applying the Log-BCJR algorithm becomes $O(\tilde{N}L_f)+O(L_u\mathcal{P}M^L)$ per iteration with an additional complexity of $O(L_f^3)$ to compute the equalizer coefficients in (3.20) and (3.21) at the initial equalizer iteration.

In the aforementioned conventional TAE receiver, an APP decoder is employed for combined equalization and demodulation, which is again followed by the channel decoder. The SISO equalization/demodulation block and the channel decoder exchange soft information regarding the encoded bits. The state of the combined trellis for the

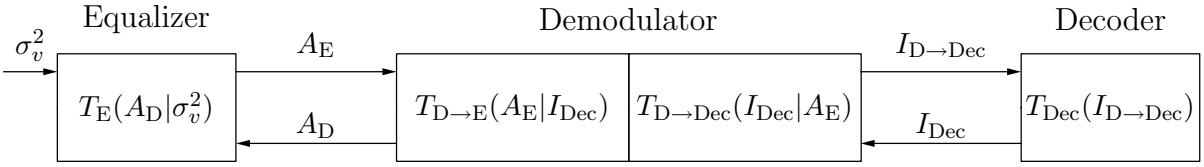
ISI channel and CPE is

$$s_\ell = [\tilde{\varphi}_\ell, \tilde{x}_{\ell-M_c-L+2}, \ldots, \tilde{x}_{\ell-M_c+1}, \ldots, \tilde{x}_{\ell-1}] \tag{3.28}$$

where $M_c := \lfloor L_c/n_s \rfloor + 1$ with $\lfloor \cdot \rfloor$ being the floor operator. The complexity per trellis instant is $O(\mathcal{P}M^{M_c+L-1})$ [15] which grows exponentially in case of longer channel responses, whereas the corresponding complexity increases linearly for the proposed receiver. Complexity from the channel decoder is omitted above because it is common to both receivers.

Depending on the doubly-iterative nature of the proposed receiver, the number of front-end iterations can also be reduced if it is possible to improve the soft information to the SIC/MMSE equalizer sufficiently with several number of back-end iterations. On the other hand, TAE should employ the APP decoder for combined equalization and demodulation at every iteration, where even non-iterative processing is difficult due to a very large super trellis with high memory requirements for $\tilde{\gamma}$ and $\tilde{\alpha}$ terms. Moreover, considering channels with very long impulse responses or higher modulation memory for partial-response CPM, the conventional method becomes impractical because of super trellises with huge number of states, which is not the case for the proposed receiver.

## 3.2. EXIT Chart Analysis




| Transfer Function | From | To | SISO Block | Input Information | Output Information | Depends on |
|---|---|---|---|---|---|---|
| $T_{\mathrm{E}}(\cdot\|\cdot)$ | $\{\bar{c}_n\}$ | $\{\hat{c}_n\}$ | Equalizer | $A_{\mathrm{D}}$ | $A_{\mathrm{E}}$ | $\sigma_v^2$ |
| $T_{\mathrm{D}\to\mathrm{E}}(\cdot\|\cdot)$ | $\{\hat{c}_n\}$ | $\{\bar{c}_n\}$ | Demodulator | $A_{\mathrm{E}}$ | $A_{\mathrm{D}}$ | $I_{\mathrm{Dec}}$ |
| $T_{\mathrm{D}\to\mathrm{Dec}}(\cdot\|\cdot)$ | $\{L_a(\tilde{u}_m)\}$ | $\{L_e(\tilde{u}_m)\}$ | Demodulator | $I_{\mathrm{Dec}}$ | $I_{\mathrm{D}\to\mathrm{Dec}}$ | $A_{\mathrm{E}}$ |
| $T_{\mathrm{Dec}}(\cdot\|\cdot)$ | $\{L_a(u_m)\}$ | $\{L_e(u_m)\}$ | Decoder | $I_{\mathrm{D}\to\mathrm{Dec}}$ | $I_{\mathrm{Dec}}$ | – |

Figure 3.3. Transfer characteristics of the doubly-iterative receiver

In this section, convergence behavior of the proposed doubly-iterative receiver is analyzed. The transfer characteristic functions for the system in Figure 3.2 are shown in Figure 3.3. At the back-end of the receiver, CPM demodulator and the channel decoder exchange soft information for the encoded bits, and the convergence behavior between these modules can be observed by using EXIT chart analysis. Here, a two dimensional graph as in [46] can be obtained by considering constant *a priori* information from the equalizer to the demodulator, whereas a three dimensional graph as in [47] can also be illustrated to observe the convergence behavior while the *a priori* information from the equalizer improves. In this section, both graphs are obtained by considering the mutual information between the encoded bits and the LLRs at the output of the demodulator/decoder as described in Section 2.2.3. On the other hand, at the front-end, deinterleaving is not applicable between the equalizer and the demodulator to conduct an EXIT chart analysis as in [46] and [47]. Therefore, simulated trajectories between these modules and the corresponding transfer characteristic curves are obtained using some average information, as described later in this section, and it is shown that performing more than one iteration between the equalizer and the demodulator does not result in any preferable turbo gain, as long as the *a priori* information from the decoder to the demodulator remains unchanged. Furthermore, switching condition from the ZAI to FAI scenario is determined by using the corresponding equalizer transfer characteristic curves.

In the convergence analysis (and in the BER simulations of the next section), the binary three raised cosine (3RC) CPM scheme of [2] with the main lobe width of $L$ symbol duration is employed where $L = 3$ and $h = 0.5$. The channel resolution is $T_s = T/2$, number of samples per symbol period is $n_s = 2$, and the two-sided bandwidth of the low-pass filter is $2/T$ so that more than 99.9 percent of the signal energy is recovered [2]. A rate-1/2 convolutional code with generator polynomial $(64, 74)_8$ is used for channel coding [64]. For multipath fading, eleven-tap quasi-static channels where the tap coefficients are zero-mean complex white Gaussian random variables with exponentially decaying power profile [65] are taken into account. For the quasi-static channels, the variance of the $l$th path coefficient is $e^{-l/2}/\left(\sum_{m=0}^{10} e^{-m/2}\right)$ and the corresponding path delay is $lT_s$ for $l = 0, 1, \ldots, 10$. The TDE is implemented with

filter parameters $F = 11$,$B = 10$, and $L_f = 22$. The complex channel noise is assumed AWGN with zero mean and variance $\sigma_v^2$.

Both the equalizer and the demodulator generate a length-$\tilde{S}$ probability vector as the soft output at each symbol interval. Since the corresponding CPM signals are symmetric so that each signal is equal to the negative of one of the other $\tilde{S} - 1$ signals, the first equalizer iteration starts with zero interference cancellation by assuming equal symbol probabilities from the demodulator. Then, the soft information at the output of these modules is improved by employing doubly-iterative processing so that the probability of the actually transmitted CPM signal at each symbolling interval approaches 1, where the probabilities for the other $\tilde{S} - 1$ signals go to zero. Considering unit-amplitude signals as in (2.1), the amplitudes of the mean values computed by these probabilities also vary from zero to one because of the symmetry conditions, as the probabilities of the actual signals approach 1. Thus, in order to obtain the char-

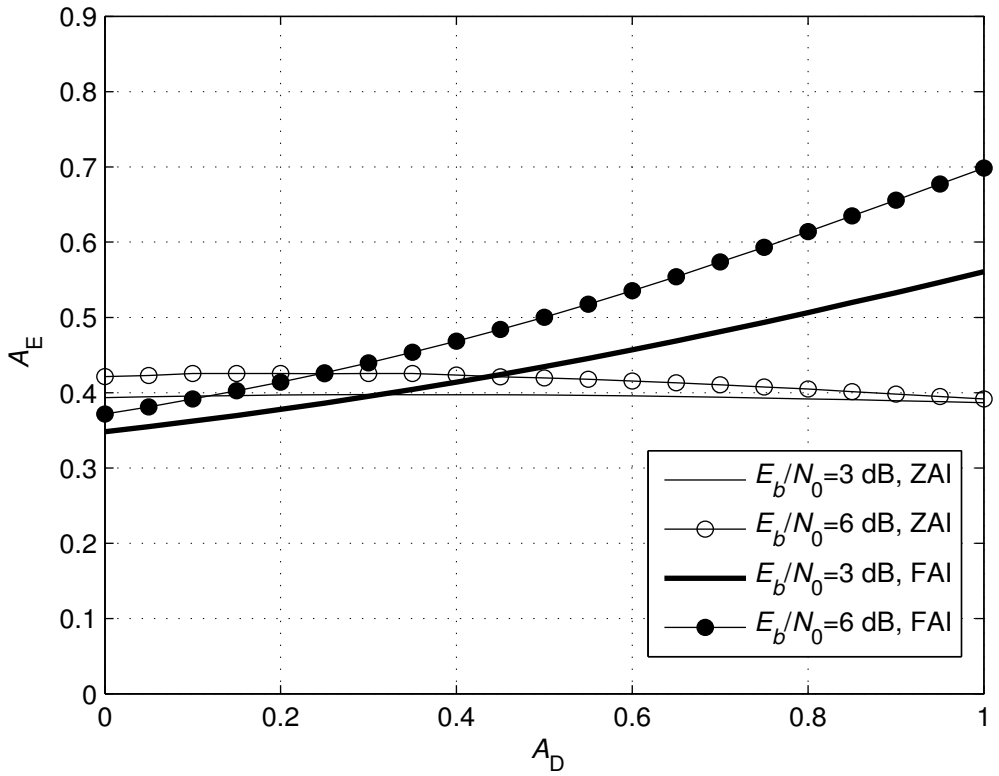



Figure 3.4. Transfer characteristic curves for the SIC/TDE at $E_b/N_0 = 3$ and 6 dB

acteristic curves and the simulated trajectories for the equalizer and the demodulator,

the average of the amplitudes of the mean values at the output of the equalizer and the demodulator are considered, which are denoted by $A_{\mathrm{E}}$ and $A_{\mathrm{D}}$, respectively. Here, using the signal probabilities in (3.6) and (3.27), $A_{\mathrm{D}}$ and $A_{\mathrm{E}}$ are computed as

$$A_{\mathrm{D}} = \frac{1}{\tilde{N}} \sum_{\ell=1}^{N} \sum_{i=0}^{n_s-1} \left| \sum_{p=0}^{\tilde{S}-1} Y_{i,p} P(y_{n_s\ell-n_s+i} = Y_{i,p}) \right|, \tag{3.29}$$

$$A_{\mathrm{E}} = \frac{1}{\tilde{N}} \sum_{\ell=1}^{N} \sum_{i=0}^{n_s-1} \left| \sum_{p=0}^{\tilde{S}-1} Y_{i,p} P(\hat{y}_{n_s\ell-n_s+i} | y_{n_s\ell-n_s+i} = Y_{i,p}) \right|, \tag{3.30}$$

respectively.

The transfer characteristic curves of the equalizers under the ZAI and FAI assumptions by averaging the results for the aforementioned eleven-tap quasi-static multipath fading channels are shown in Figure 3.4, where $E_b/N_0 = 3$ and 6 dB. Given that the $p$th signal transmitted at the $\ell$th symbol interval, sample probabilities $P(y_{n_s\ell-n_s+i} = Y_{i,p})$ from the demodulator are generated artificially for all $Y_{i,p} \in \mathcal{Y}_i$ by setting the probabilities of the samples corresponding to the $p$th signal as $p_t$ and the rest of the probabilities as $(1-p_t)/(\tilde{S}-1)$, where $1/\tilde{S} \leq p_t \leq 1$, $\ell = 1, \ldots, N$, and $i = 0, \ldots, N_s-1$. Then, $A_{\mathrm{D}}$ is computed by (3.29) so that it converges from zero to one as $p_t \to 1$. Furthermore, the computed mean values are also employed for the soft interference cancellation, and $A_{\mathrm{E}}$ is found by (3.30) using the probabilities generated by the equalizer. Notice that the correlation coefficients are computed using Laurent's decomposition with the assumption that all bits are equally-likely. For the equalizer operating under ZAI assumption, this is nearly the case at low $A_{\mathrm{D}}$ values. However, as $A_{\mathrm{D}}$ values approach 1, the case converges to the perfect interference cancellation state, implying that the cross correlations decrease gradually and become eventually zero. Therefore, using symbol correlations in this case at high $A_D$'s causes a slight performance degradation. On the other hand, the equalizer assuming full *a priori* information assumption and employing (3.21) has a monotonically increasing characteristic curve with better gain, but its performance under inadequate interference cancellation is worse compared to zero information scenario. Moreover the performance gain at high SNRs as $A_D$ increases is more significant than its zero *a priori* information counterpart. Therefore,

a feasible hybrid strategy for best achievable performance is to employ the former equalizer initially, and then to switch to the latter one as the *a priori* information to

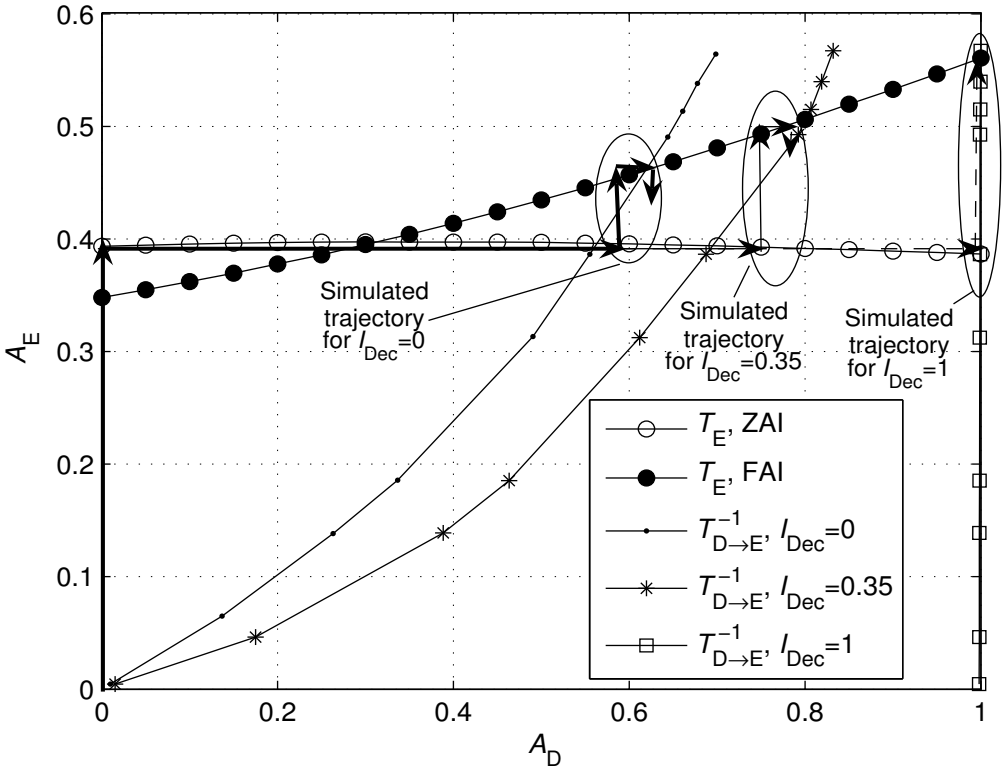



Figure 3.5. Comparison of the simulated trajectories and the characteristic curves for the TDE and the demodulator at $E_b/N_0$=3 dB

the equalizer is improved. In Figure 3.5, the simulated trajectories at $E_b/N_0 = 3$ dB between the equalizer and the demodulator are illustrated for three different sets of *a priori* knowledge from the decoder, where the equalizer coefficients are set as (3.21) for $A_{\mathrm{D}}$ values less than 0.4 and as (3.20) for greater values. As proposed in [46], the LLRs $\{L_a(\tilde{u}_m)\}$ are generated according to the single-parameter Gaussian model in (2.68) and $I_{\mathrm{Dec}}$ values are computed as the mutual information between the encoded bits and the LLRs as in (2.70), by using the conditional PDFs in (2.69) belonging to this model. In Figure 3.5, simulated trajectories tend to follow the path confined between the equalizer and demodulator characteristic curves so that the simulated and semi-analytical results are almost consistent. The transfer characteristic curves for the equalizer are obtained as in Figure 3.4, where the demodulator characteristic curves are found by generating the equalizer outputs artificially. For this purpose, the model

for the equalizer output in (3.14) is considered as

$$\hat{c}_n = \mathbf{f}^H \tilde{\mathbf{r}}_n := \mathbf{f}^H \tilde{\mathbf{H}}\mathbf{e}\, c_n + \mathbf{f}^H \mathbf{d}_n, \tag{3.31}$$

where $\mathbf{d}_n$, defined similar to the channel noise vector $\mathbf{v}_n$ in (3.9) as,

$$\mathbf{d}_n = \begin{bmatrix} d_{n+F} & d_{n+F-1} & \dots & d_{n-B+1} & d_{n-B} \end{bmatrix}^T \tag{3.32}$$

contains the i.i.d. additive Gaussian noise terms each with zero-mean and variance $\sigma_d^2$. Because channel noise terms after low-pass filtering and sampling are assumed to be white at the beginning of this section, the elements of $\mathbf{d}_n$ are also generated as white Gaussian random variables. Note that each $d_i$ $(i = n+F, \dots, n-B)$ contains the corresponding channel noise sample $v_i$ as well as the uncancelled interference for the symbol $c_n$. Therefore it is assumed that $\sigma_v^2 \leq \sigma_d^2$ where the equality holds in the case of perfect interference cancellation. Here $D_{\min}$ in (3.30) corresponds to the average squared distance where the parameters for the model in (3.31) are set as $\sigma_d^2 = \sigma_v^2$ and $\mathbf{f} = \mathbf{f}_{\text{FAI}}$. Then the equalizer output at each time instant is artificially generated by (3.31), and the symbol probabilities are computed using (3.24), (3.25), and (3.27). Afterwards, these probabilities are fed to the demodulator. Using the same switching condition considered to obtain the simulated trajectories, the discrete-time symbols that give $A_{\text{E}}$ values (computed by (3.30)) from zero to the output of the equalizer's characteristic curve for $A_{\text{D}} = 0.4$ under no *a priori* information assumption are found by employing (3.20) in (3.31), where the symbols that result in greater $A_{\text{E}}$ values are generated by inserting (3.21) into (3.31) so that $A_{\text{E}}$ converges to one as $\sigma_d^2$ approaches $\sigma_v^2$. As shown in Figure 3.5, it is not possible to improve the equalizer outputs for $A_{\text{D}} < 0.4$ due to the lower gain of the equalization method using (3.20). Moreover, for larger $A_{\text{D}}$ values, it is observed that the equalizer outputs are getting worse after several equalizer/demodulator iterations (see the trajectory for $I_{\text{Dec}} = 0.35$). This is because the equalizer outputs are correlated, and deinterleaving is not possible since the interleaving after the CPM modulation destroys the phase continuity [8]. Therefore, it is more convenient to enhance the *a priori* information from the demodulator to get better equalizer outputs by performing a couple of demodulator/decoder itera-

tions (which improve $I_{\text{Dec}}$), instead of employing more than one equalizer/demodulator iteration with the same $I_{\text{Dec}}$.

In case of back-end iterations, the demodulator transforms the *a priori* information $\{L_a(\tilde{u}_m)\}$ for the interleaved code bits from the channel decoder to $\{L_e(\tilde{u}_m)\}$, given the tilted-phase CPM signal probabilities from the equalizer. LLRs $\{L_a(\tilde{u}_m)\}$ are

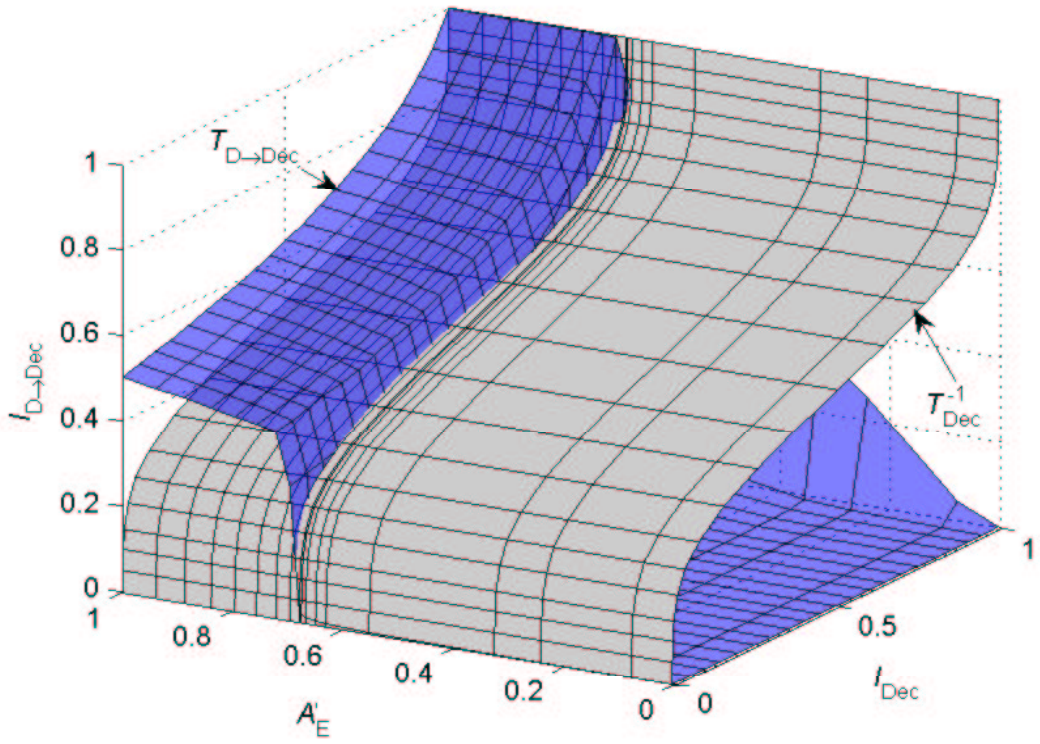



Figure 3.6. EXIT chart analysis for the back-end iterations of the doubly-iterative receiver with TDE

generated depending on the model in (2.68), and $I_{\text{Dec}}$ values are computed as in (2.70) using the conditional PDFs in (2.69) belonging to this model, as previously stated. After the output conditional PDFs are determined by histogram measurements, $I_{\text{D}\rightarrow\text{ Dec}}$ is computed in the same way, as the mutual information between the encoded bits and the LLRs at the output of the demodulator [46]. Similar procedure is followed to compute $I_{\text{D}\rightarrow\text{ Dec}}$ and $I_{\text{Dec}}$ at the input and output of the channel decoder, respectively. The three-dimensional plot in Figure 3.6 illustrates the EXIT behavior for eleven-tap quasi-static channels at $E_b/N_0 = 3$ dB between the demodulator (upper surface) and the decoder for varying information from the equalizer. The tilted-phase CPM sig-

nal probabilities from the equalizer to the demodulator are generated according to the model in (3.31). The switching condition to decide on employing either (3.20) or (3.21) is the same as in Figure 3.5 while generating the equalizer outputs artificially. Since $A_{\mathrm{E}}$ values reach to one only at high SNRs, $A'_{\mathrm{E}} = A_{\mathrm{E}}/\max(A_{\mathrm{E}})$ is used in Figure 3.6 instead of $A_{\mathrm{E}}$ for better presentation purposes, where $\max(A_{\mathrm{E}})$ gives the maximum value for $A_{\mathrm{E}}$. As shown in Figure 3.6, the gap between the demodulator and decoder surfaces becomes wider as better information is provided by the equalizer, and no bottlenecks are encountered after $A'_{\mathrm{E}} = 0.68$. Thus, it is necessary for convergence to terminate

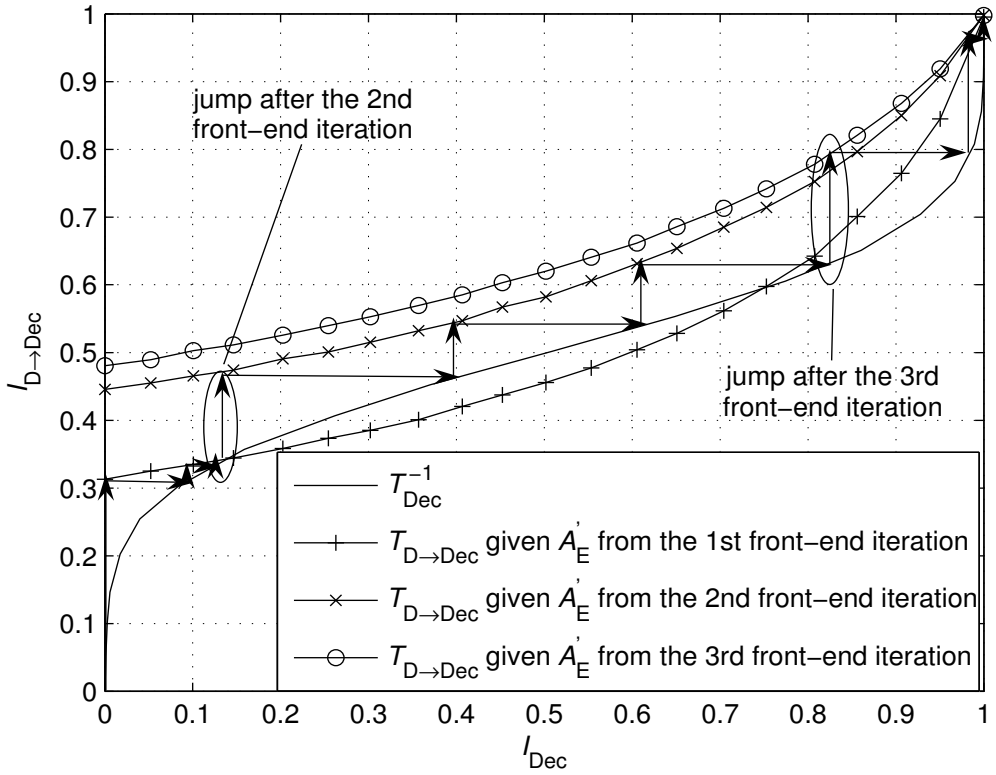



Figure 3.7. Analysis for the front-end and back-end iterations of the doubly-iterative receiver with TDE

back-end iterations after a bottleneck is encountered, and then to perform a new front-end iteration to have a wider gap between the demodulator and decoder curves. In Figure 3.7, starting with the $\sigma_d^2$ value under ZAI assumption that corresponds to the first equalizer iteration with no interference cancellation, three back-end iterations can be performed up to the bottleneck, at which the demodulator produces the inputs to the equalizer that generates better signal probabilities for the next set of back-end iterations, where FAI scenario is considered for $A_{\mathrm{D}} > 0.4$. By updating the probabilities

from the equalizer following each set of back-end iterations, the convergence is achieved after three front-end iterations.

### 3.3. Simulation Results

In this section, the BER performance of the doubly-iterative receiver with TDE is presented for different number of front- and back-end iterations. Moreover, the BER performance of the proposed receiver is compared to that of the TAE and the case without ISI, as well. As decribed at the beginning of this chapter, in TAE implementation, soft information is exchanged between the optimal CED and the channel decoder where both modules apply the Log-BCJR algorithm. The parameters used in the BER simulations are selected as those in the EXIT chart analysis so that binary 3RC CPM with $L = 3$ and $h = 0.5$ is considered. Before applying CPM, bits are encoded by rate-1/2 convolutional code with generator polynomial $(64, 74)_8$. Each data packet consists of 256 bits. Random interleaving is applied since it results in high performance as shown in [8]. The channel resolution is $T_s = T/2$, number of samples per symbol period is $n_s = 2$, and the two-sided bandwidth of the low-pass filter is $2/T$ so that more than 99.9 percent of the signal energy is recovered [2]. The static ISI channel is selected as Proakis' A [66] with channel tap weights [0.04 -0.05 0.07 -0.21 -0.5 0.72 0.36 0.00 0.21 0.03 0.07]. The filter parameters are set as $F = 11$ and $B = 10$ which lead to $L_f = 22$. The channel coefficients are normalized to have unit total energy. The BER performance is also observed in case of eleven-tap quasi-static multipath fading channels (channel I) changing independently at each packet transmission. The channel coefficients are generated as complex Gaussian random variables with exponentially decaying power profile. Here, $\tilde{h}_l$ as the $l$th path gain is a zero-mean complex Gaussian random variable with variance being equal to $e^{-l/2}/\big(\sum_{m=0}^{10} e^{-m/2}\big)$ and the corresponding path delay is $lT_l$ where $l = 0, 1, \ldots, 10$. Furthermore, the six-tap typical urban channel (channel II) model in [22] is considered, where the variances of the complex Gaussian path coefficients are [0.189 0.379 0.255 0.090 0.055 0.032] and the corresponding path delays are [0 $T_s$ $2T_s$ $8T_s$ $12T_s$ $25T_s$]. In the legends of the figures for the BER performance, the abbreviations FIT and BIT are used to denote the front-end iterations and the back-end iterations, respectively. For instance, "4th FIT

w/ 3 BIT" denotes the fourth execution of one SIC/TDE iteration followed by three demodulator/decoder iterations at the back-end. In consistency with Section 3.2, $A_{\mathrm{D}}$

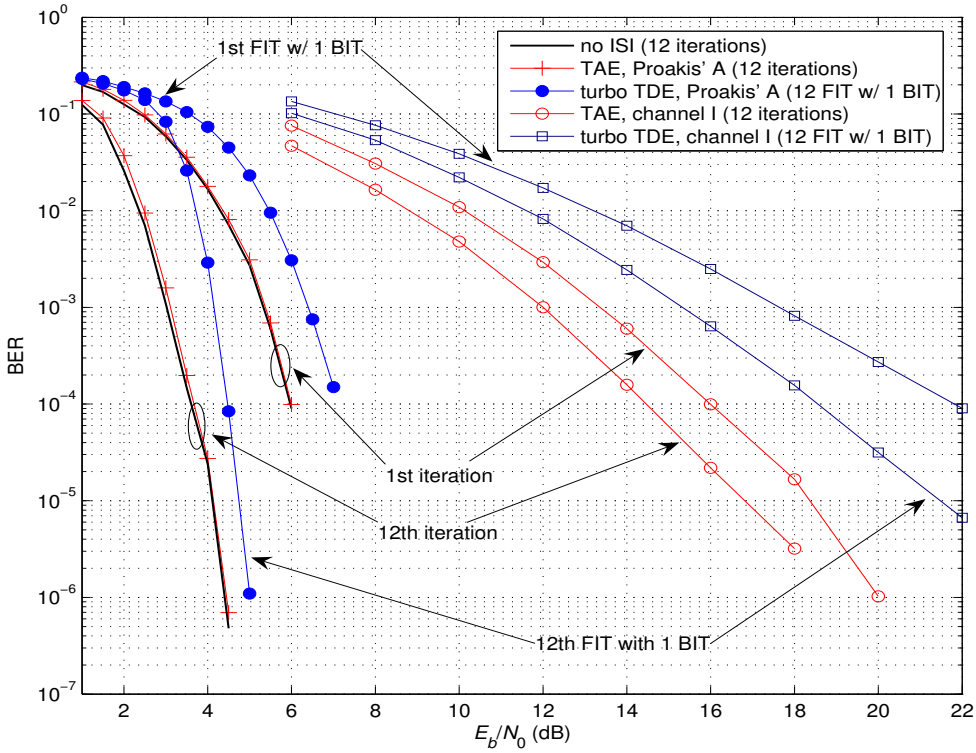



Figure 3.8. BER performance for no ISI, Proakis' A channel, and channel I

is computed as in (3.29) before each equalizer iteration, and (3.20) is replaced with (3.21) for $A_{\mathrm{D}}$ values greater than 0.4.

The BER performance of the proposed receiver and TAE in Proakis' A channel and eleven-tap quasi-static channels, and the iterative demodulation and decoding in AWGN channel are presented in Figure 3.8. When the ISI channel is not present, the receiver consists of a CPM demodulator followed by the channel decoder. Both the demodulator and the channel decoder employ the Log-BCJR algorithm. Twelve iterations are run for the turbo CPM demodulation and channel decoding. For doubly-iterative equalization, twelve executions of one FIT followed by one BIT are performed. The TAE performs twelve iterations between CED and the channel decoder. Due to the suboptimality of the proposed receiver, the BER for the first front-end + back-end iteration is below $10^{-5}$ only after 21 dB, for Proakis' A channel. Thus, after twelve passes of one FIT with one BIT, performance gain is about 15 dB. As shown in Figure

3.8, performance of the proposed receiver is very close to that of TAE in Proakis' A channel.

The receiver may encounter bottlenecks on convergence without performing more

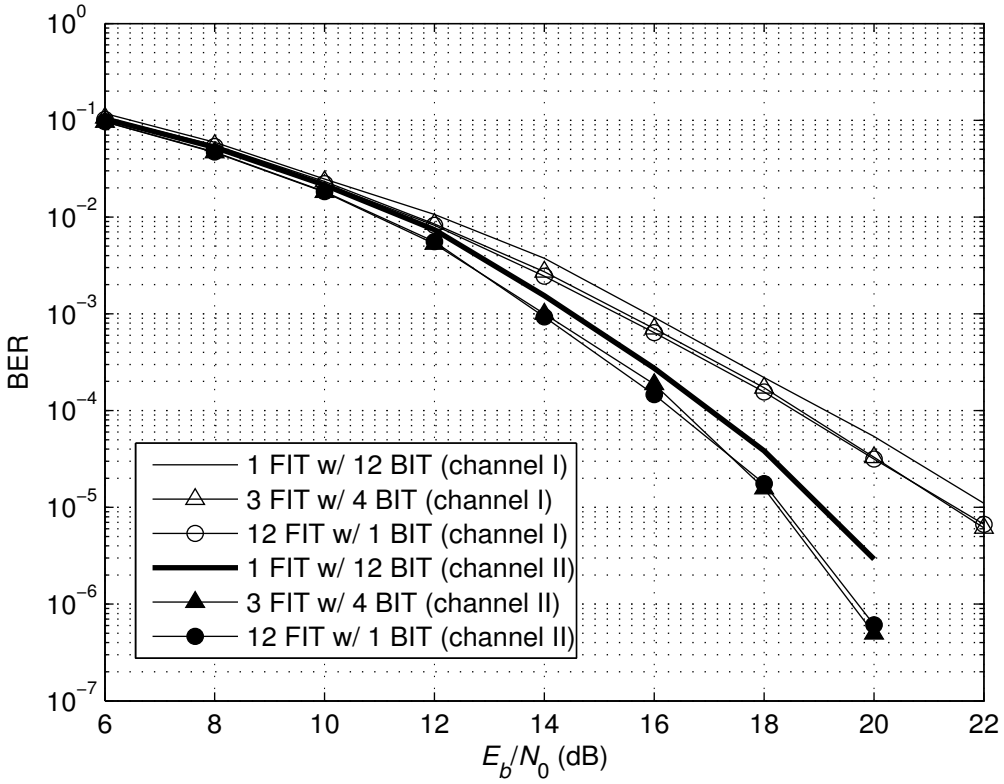



Figure 3.9. BER performance in channels I and II

than one front-end equalizer iteration, as also observed in Section 3.2. This behavior can be observed in Figure 3.9, as well. Here, by performing twelve passes of one front-end iteration followed by one back-end iteration, BER values below $10^{-5}$ are observed after 21 dB and 18 dB in channel I channel II scenarios, respectively, where the performance gain compared to performing only one front-end iteration followed by twelve back-end iterations is around 0.7 dB and 1 dB respectively. However, it is not always necessary to employ many equalizer iterations since running sufficient number of back-end iterations improves the *a priori* information for SIC and reduces the number of the front-end iterations. In Figure 3.9, by employing four front-end iterations, where each is followed by three back-end iterations, similar performance is observed compared to twelve passes of one front-end iteration with one back-end

iteration, where the number of equalizer iterations is three times less in the former scenario.

# 4. DOUBLE TURBO EQUALIZATION OF CPM WITH FREQUENCY DOMAIN PROCESSING

In order to alleviate the high complexity of the CED module in [10] which uses a single super trellis for the optimal detection of CPM over the multipath fading channels and motivated by the near-optimum error performance of the iterative receivers, an alternative CPM receiver is proposed in Chapter 3 where the equalization, CPM demodulation, and channel decoding operations are assigned to three separate SISO blocks and the central demodulator is coupled with both the front-end equalizer and the back-end decoder in a doubly-iterative architecture. The most important feature of this receiver is that a soft-information-aided MMSE TDE is used at its front-end instead of a trellis-based algorithm, which presents a low complexity alternative while still achieving a performance close to the "no interference" bound. Notice that computing the MMSE TDE coefficients requires some cumbersome matrix inversions causing the computational load to be still relatively large in long channel responses. As presented in [19]-[21], by doing the equalization in the frequency domain the complexity can be reduced further while attaining the same and often better performance.

The FDE approach has also been extended to the equalization of CPM in [22], where the FDE is not equipped with any SISO capability and thus is not suitable for turbo processing. The advantages of frequency-domain processing and iterative information exchange are combined in [23], where a SISO BFDE is followed by the SISO CPM demodulator and channel decoder modules in the proposed TLE structure. Here, the soft CPM signal information to start the subsequent equalization iterations are computed from the code bit probabilities obtained from the back-end channel decoder. However, this produces long error bursts due to the inherent modulation memory and thus, the CPM signal probabilities are delivered to BFDE only at certain epoches to break up the error propagation at the expense of obtaining only a slight turbo gain. Moreover, because the proposed FDE operates on blocks of information, it still involves matrix inversions which result in an increased computational cost. For this

reason, herein a soft-information-aided FDE for CPM is proposed which overcomes the disadvantages of that in [23] and replaces the front-end TDE in Figure 3.2, so as to achieve a better error performance with lower computational complexity compared to the methods in both Chapter 3 and [23] .

In the proposed receiver, the frequency-domain processing of CPM signals is made possible by inserting a cyclic guard interval longer than the channel memory while maintaining the phase continuity of CPM. The FDE is equipped with an *a priori* SIC and an APP mapper to generate soft information for the central CPM demodulator. As described in Chapter 3, the decoder used for demodulation computes extrinsic information at its output on both the discrete-time CPM signals and the coded bits. Then, these two soft outputs are employed in a doubly-iterative information exchange where the CPM demodulator is coupled with both the front-end FDE and the back-end decoder. Because the CPM signal probabilities are not computed from the code bit probabilities, the error bursts of [23] due to the modulation memory are not encountered, which results in a significant performance improvement. Moreover, because its implementation does not involve any matrix inversion, the proposed SISO FDE is computationally less complex than the linear equalizers in Chapter 3 and [23]. The doubly-iterative CPM receiver with the FDE is also more feasible compared to the TLE in [23] in attaining faster convergence to low BERs because the number of front-end iterations are decreased by performing several demodulation/decoding iterations per each equalization iteration to improve the equalizer *a priori* information. This behavior can be justified by two and three dimensional EXIT charts analysis similar to the approach in Section 3.2 presented for the doubly-iterative receiver with TDE.

The rest of the chapter is organized as follows. In Section 4.1, the cyclic guard insertion, the doubly-iterative receiver with FDE, the proposed soft-information-aided FDE algorithm, and the complexity comparisons with alternative receiver structures are presented. A similar comparison in terms of BER simulations is given in Section 4.3 after the convergence analysis in Section 4.2.

### 4.1. Doubly-Iterative Equalization with Frequency Domain Processing

At the transmitter, a length-$L_b$ data bit sequence with elements $b_i \in \{0, 1\}$, $i = 1, \ldots, L_d$, is encoded by a rate-$L_b/L_u$ convolutional code to form $u_m \in \{-1, +1\}$ where $m = 1, \ldots, L_u$. Then $u_m$ are interleaved to $\tilde{u}_m$, which are mapped onto the $M$-ary symbols $x_\ell$ defined in Section 2.1.1 where $\ell = 1, \ldots, N$ with $N = L_u/\log_2 M$. Using these symbols, CPM waveforms are generated and transmitted throughout the multipath fading channel. The receiver observes a noisy linear convolution of the transmitted signals with the multipath fading channel. To make frequency-domain processing possible , the transmitter structure in Figure 3.1 needs to be modified by deploying a new module in between the symbol mapper and the CPE to append a cyclic prefix to the transmitted signal sequence at the expense of an increased redundancy. Here the length of the cyclic prefix, $G$, is chosen as the minimum number of symbol

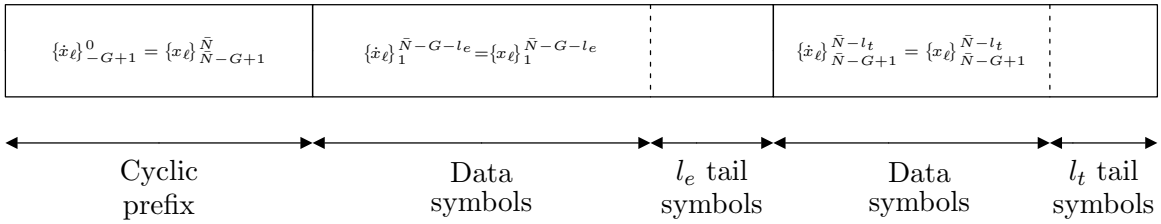



Figure 4.1. Modulating sequence with the cyclic prefix

periods to avoid interblock interference due to the multipath channel effects. However, the transmission of CPM signals also requires the preservation of phase continuity within each transmitted block and between consecutive transmitted blocks. Observing the similarity of the CPE to a recursive convolutional encoder, this phase continuity can be attained by inserting two sets of tail symbols of lengths $l_e$ and $l_t$ after the first $N - G + l_t$ modulating symbols and to the end of the whole symbol sequence, respectively. After setting the initial state for the CPE trellis as the zero state in (2.19) before applying the modulating symbol sequence, by choosing $l_t$ as the minimum number of symbols to return to the zero state from any trellis state and $l_e \geq l_t$ as the number of symbols to return to and stay at the zero state, it is assured that the CPE trellis path returns to the zero state at $n = N - G + l_t + l_e$ and $n = N + l_t + l_e$. The symbol sequence with tail symbols becomes $\{x_\ell\}_1^{\bar{N}}$ where $\bar{N} = N + l_t + l_e$. Then, the length-$G$ cyclic prefix, selected as the last $G$ symbols, is appended to the beginning

of the symbol block as depicted in Figure 4.1 and the new symbol sequence becomes $\dot{x}_\ell = x_{(\ell-1)_{\bar{N}}+1}$, $\ell = -G+1, \ldots, -1, 0, 1, \ldots, \bar{N}$, where $(\cdot)_{\bar{N}}$ stands for the modulo-$\bar{N}$ operation. The CPE employs the new symbol sequence $\dot{\mathbf{x}}_{-G+1}^{\bar{N}} = \{\dot{x}_\ell\}_{-G+1}^{\bar{N}}$ to generate the tilted-phase signal $y(t, \dot{\mathbf{x}}_{-G+1}^{\bar{N}})$ so that $y(t, \dot{\mathbf{x}}_{-G+1}^{\bar{N}}) = y(t+\bar{N}T, \dot{\mathbf{x}}_{-G+1}^{\bar{N}})$ on the interval $-GT < t < 0$. By compensating for the frequency shift in (2.14), the CPM signal is obtained as

$$c(t, \dot{\mathbf{x}}_{-G+1}^{\bar{N}}) = y(t, \dot{\mathbf{x}}_{-G+1}^{\bar{N}}) e^{-j\pi h(M-1)t/T}, \qquad -GT < t < \bar{N}T. \tag{4.1}$$

Note that this new sequence ensures that the CPE trellis path for each packet begins and ends at the zero state and therefore no phase discontinuities are encountered during the transitions between consecutive packets. Furthermore, within each packet, the trellis path returns to the zero state after the first $G$ symbols so that the cyclic guard interval does not disrupt the phase continuity. When $l_e$ is chosen properly such that $h\bar{N}$ is an even integer, (4.1) yields that $c(t, \dot{\mathbf{x}}_{-G+1}^{\bar{N}}) = c(t + \bar{N}T, \dot{\mathbf{x}}_{-G+1}^{\bar{N}})$ on the interval $-GT < t < 0$ since $e^{-j\pi h(M-1)(t+\bar{N}T)/T} = e^{-j\pi h(M-1)t/T}$.

After the transmission through the ISI channel, the received signal at the base-band using the similar representation in (2.25) is denoted as

$$r(t) = \sum_{l=0}^{L_c-1} \tilde{h}_l c(t - lT_s, \dot{\mathbf{x}}_{-G+1}^{\bar{N}}) + v(t), \qquad -GT < t < \bar{N}T, \tag{4.2}$$

where $v(t)$ is the zero-mean AWGN term. After the removal of the prefix and low-pass filtering with a two-sided bandwidth of $1/T_s$ Hertz, the discrete symbols are obtained by sampling the filter output every $T_s$ seconds such that the additive noise is still white and there is no aliasing. After sampling, (4.2) becomes

$$r(nT_s) = \sum_{\ell=0}^{L_c-1} \tilde{h}_\ell c(nT_s - \ell T_s, \dot{\mathbf{x}}_{-G+1}^{\bar{N}}) + v(nT_s), \qquad n = 0, \ldots, \tilde{N}-1, \tag{4.3}$$

where $\tilde{N} = n_s\bar{N}$. Then, defining $r_n := r(nT_s)$, $c_n := c(nT_s, \dot{\mathbf{x}}_{-G+1}^{\bar{N}})$, $v_n := v(nT_s)$, $\tilde{\mathbf{h}}_0^{\tilde{N}-1} := \{\tilde{h}_n\}_0^{\tilde{N}-1}$ that is obtained through zero padding after the first $L_c$ terms, and

$\mathbf{c}_0^{\tilde{N}-1} := \{c_n\}_0^{\tilde{N}-1}$, (4.3) can be rewritten as

$$r_n = \sum_{\ell=0}^{L_c-1} \tilde{h}_\ell c_{(n-\ell)_{n_s\tilde{N}}} + v_n = [\tilde{\mathbf{h}} \star \mathbf{c}]_n + v_n, \qquad n = 0, \ldots, \tilde{N}-1. \tag{4.4}$$

Here $[\tilde{\mathbf{h}} \star \mathbf{c}]_n$ denotes the $n$th element of the circular convolution of the sequences $\tilde{\mathbf{h}}_0^{\tilde{N}-1}$ and $\mathbf{c}_0^{\tilde{N}-1}$ whose indices are dropped for notational simplicity.

### 4.1.1. Receiver Overview

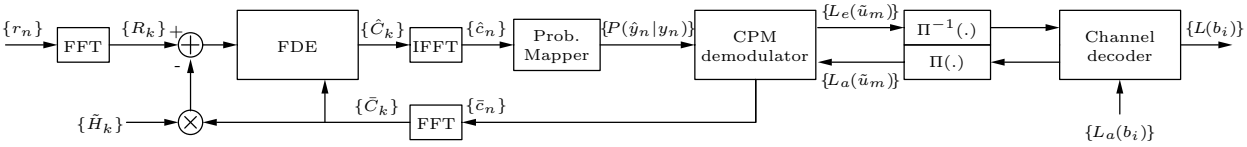



Figure 4.2. Doubly-iterative receiver with FDE

The proposed doubly-iterative CPM receiver with FDE is shown in Figure 4.2. Here $\hat{c}_n$ is the equalizer output at time $n$ where $\hat{y}_n$ corresponds to its tilted-phase counterpart. Furthermore $y_n$ denotes the $n$th sample for the tilted-phase CPM signal and $\bar{c}_n$ is the mean-value of the $n$th CPM signal sample. The *a priori* and extrinsic LLRs for the interleaved code bits are denoted as $L_a(\tilde{u}_m)$ and $L_e(\tilde{u}_m)$, respectively. For the data bits, $\{L_a(b_i)\}$ are the *a priori* LLRs which are always zero and $\{L(b_i)\}$ are the output LLRs used for the bit decisions. $\{R_k\}$, $\{\hat{C}_k\}$, $\{\bar{C}_k\}$, and $\{\tilde{H}_k\}$ are the $\tilde{N}$-point discrete Fourier transforms (DFTs) of $\{r_n\}$, $\{\hat{c}_n\}$, $\{\bar{c}_n\}$, and $\{\tilde{h}_n\}$, respectively. Initially the FDE iteration starts with no *a priori* information, and no interference cancellation takes place. At the output of this process, within each symbol interval, $n_s$ samples are mapped onto a $\tilde{S}$-ary vector of extrinsic probabilities so as to start the back-end iterations between the CPM demodulator and the channel decoder as described in Section 3.1.1. The demodulator generates extrinsic information on both the coded bits $c_n$ in the form of LLRs as in (3.2) and the tilted-phase CPM signals in the form of $\tilde{S}$-ary vectors as in (3.6) which are used to compute $\{\bar{c}_n\}$ as in (3.7). The former is exchanged within the back-end iterations, where the latter is used to compute the expected values, $\bar{y}_n$, to start the next equalization iteration after any number of back-end iterations. The detailed presentation of the operation of the channel decoder using

the Log-BCJR algorithm is given in Section 2.2.1. After performing the aforementioned double iterations, the estimates for the data bits are computed by taking the sign of the LLRs in (2.58).

The front-end equalizer applies DFT, SIC/FDE, and inverse DFT (IDFT) operations consecutively to obtain the outputs from which the soft information to the demodulator is calculated by the probability mapper.

### 4.1.2. SIC/MMSE FDE

The derivation of the SIC/FDE algorithm is described by presenting its time-domain equivalent first and then the corresponding representation in the frequency domain afterwards. Defining $\mathbf{w} := \{w_n\}_0^{\tilde{N}-1}$, $\bar{\mathbf{c}} := \{\bar{c}_n\}_0^{\tilde{N}-1}$, and $\mathbf{v} := \{v_n\}_0^{\tilde{N}-1}$ length-$\tilde{N}$ sequences collecting the equalizer coefficients, the mean values for the discrete CPM symbols, and the noise samples, respectively, and after applying the SIC and equalization filtering to (4.4), the discrete-time output corresponding to the sample at $t = nT_s$ of the transmitted signal $c(t, \dot{\mathbf{x}}_{-G+1}^{\bar{N}})$ is found as

$$\hat{c}_n = [\mathbf{w} \star \tilde{\mathbf{h}} \star \mathbf{c}]_n + [\mathbf{w} \star \mathbf{v}]_n - [\mathbf{w} \star \tilde{\mathbf{h}} \star \bar{\mathbf{c}}]_n + \mu \bar{c}_n \tag{4.5}$$

where $\mu = \sum_{\ell=0}^{\tilde{N}-1} w_\ell \tilde{h}_{\tilde{N}-\ell}$ is the symbol gain of the $c_n$ terms in $[\mathbf{w} \star \tilde{\mathbf{h}} \star \mathbf{c}]_n$ and $\mu \bar{c}_n$ prevents the cancellation of the symbol information at time $n$. The gain $\mu$ can be computed in both the time-domain and frequency-domain by employing Plancherel's Theorem, which leads to

$$\mu = \sum_{\ell=0}^{\tilde{N}-1} w_\ell \tilde{h}_{\tilde{N}-\ell} = \frac{1}{\tilde{N}} \sum_{k=0}^{\tilde{N}-1} W_k \tilde{H}_k \tag{4.6}$$

where $W_k$ and $\tilde{H}_k$, $k = 0, 1, \ldots, \tilde{N}-1$, are the $\tilde{N}$-point DFTs of $w_n$ and $\tilde{h}_n$, respectively. The equalization method proposed in this section is the frequency-domain equivalent of the time-domain equalization in (4.5). In the frequency domain, the equalization

operation in (4.5) corresponds to

$$\hat{C}_k = W_k R_k - W_k \tilde{H}_k \bar{C}_k + \mu \bar{C}_k, \qquad k = 0, 1, \ldots, \tilde{N}-1, \tag{4.7}$$

where $R_k = \tilde{H}_k C_k + V_k$ and $\hat{C}_k$, $\bar{C}_k$, $R_k$, and $V_k$ are the $\tilde{N}$-point DFTs of $c_n$, $\hat{c}_n$, $\bar{c}_n$, $r_n$, and $v_n$, respectively. Here, the frequency-domain filter coefficients $\{W_k\}$ having the MMSE solution are computed by minimizing

$$\mathrm{E}\left[\left|C_k - \hat{C}_k\right|^2\right] = \mathrm{E}\left[\left|C_k - W_k R_k + W_k \tilde{H}_k \bar{C}_k - \mu \bar{C}_k\right|^2\right]. \tag{4.8}$$

Notice that the $W_k$ values need to be updated at each equalizer iteration since different $\bar{C}_k$ values are delivered from the CPM demodulator at each front-end iteration, as shown in detail in Appendix B. This complexity can be reduced by computing two different sets of equalizer coefficients under ZAI or FAI assumptions as in [13] and by starting the initial equalizer iterations with the ZAI coefficients and then switching to the FAI coefficients after a few iterations.

The optimum coefficients minimizing (4.8) for the ZAI and FAI cases which correspond to $\bar{C}_k = 0$ and $\bar{C}_k = C_k$ assumptions, respectively, are derived in Appendix B as

$$W_k^{\mathrm{ZAI}} = \frac{\mathrm{E}\left[|C_k|^2\right] \tilde{H}_k^*}{\tilde{N}\sigma_v^2 + \mathrm{E}\left[|C_k|^2\right] |\tilde{H}_k|^2}, \tag{4.9}$$

$$W_k^{\mathrm{FAI}} = \frac{\left(1 - \frac{1}{\tilde{N}} \sum_{\ell=0}^{\tilde{N}-1} W_\ell \tilde{H}_\ell\right) \mathrm{E}\left[|C_k|^2\right] \tilde{H}_k^*}{\tilde{N}^2 \sigma_v^2} = \frac{(1-\mu)\mathrm{E}\left[|C_k|^2\right] \tilde{H}_k^*}{\tilde{N}^2 \sigma_v^2}, \tag{4.10}$$

where $*$ denotes the complex conjugation. Notice that, for simplicity, $\mathrm{E}\left[|C_k|^2\right]$ terms in (4.9) and (4.10) can be replaced by the average

$$\frac{1}{\tilde{N}} \sum_{k=0}^{\tilde{N}-1} |C_k|^2 = \frac{1}{\tilde{N}} \sum_{k=0}^{\tilde{N}-1} \sum_{n=0}^{\tilde{N}-1} \sum_{\ell=0}^{\tilde{N}-1} c_n c_\ell^* e^{-j2\pi(n-\ell)k/\tilde{N}} = \tilde{N}, \tag{4.11}$$

which is independent of the index $k$ and obtained through the symmetry of the DFT

operation and the unit-amplitude CPM signals. Then, using this replacement and the joint solution of (4.6) and (4.10) for $\mu$ together, the equalizer coefficients in (4.9) and (4.10) for the ZAI and FAI cases simplify to

$$W_k^{\mathrm{ZAI}} = \frac{\tilde{H}_k^*}{\sigma_v^2 + |\tilde{H}_k|^2}\,, \tag{4.12}$$

$$W_k^{\mathrm{FAI}} = \frac{\tilde{H}_k^*}{\tilde{N}\sigma_v^2 + (1/\tilde{N})\sum_{\ell=0}^{\tilde{N}-1}|\tilde{H}_\ell|^2}\,, \tag{4.13}$$

respectively.

The SIC exploits the mean values, $\{\bar{c}_n\}$, which are calculated by the demodulator as shown in (3.7). After performing the DFT operations on (3.7) and (4.4), and computing the frequency-domain outputs with (4.7) by either using (4.12) or (4.13), the time-domain outputs, $\{\hat{c}_n\}$, are found by the IDFT operation. Then, the soft information for CPM demodulator is computed by the probability mapper. For this purpose, the equalizer output with the tilted-phase is found as $\hat{y}_n = \hat{c}_n e^{j\pi h(M-1)n/n_s}$, $n = 0, 1, \ldots, \tilde{N}-1$, which can be viewed as $\hat{y}_n = \mu y_n + \upsilon_n$ as in (3.23) where $\mu$ is the symbol gain presented in (4.6) and $\upsilon_n$ is the zero-mean complex additive Gaussian noise [13, 15]. The probability mapper calculates the sample probabilities delivered to the demodulator as

$$P(\hat{y}_{n_s\ell-n_s+i}|y_{n_s\ell-n_s+i} = Y_{i,p}) = \frac{e^{-\frac{|\hat{y}_n-\mu Y_{i,p}|^2}{\bar{\sigma}^2}}}{\sum_{m=0}^{\tilde{S}-1} e^{-\frac{|\hat{y}_n-\mu Y_{i,m}|^2}{\bar{\sigma}^2}}} \tag{4.14}$$

for $\ell = 1, \ldots, \bar{N}$, $i = 0, 1, \ldots, n_s-1$, $p = 0, 1, \ldots, \tilde{S}-1$, and $Y_{i,p} \in \mathcal{Y}_i$ as described in Section 2.1.1, where $\bar{\sigma}^2$ is the average variance for $\upsilon_n$ computed at each equalizer iteration as in (3.26) using the symbol gain in (4.6) and the FDE outputs.

### 4.1.3. Complexity Comparison

The SIC/FDE employs fast Fourier transform (FFT) and inverse FFT (IFFT) operations. Considering that $\tilde{N}$ is an integer power of two, FFT or IFFT requires

$\tilde{N}\log_2\tilde{N}$ complex multiplications and approximately those many complex additions [67]. Thus, the number of real multiplications and the real additions (approximately) to obtain all $R_k$ and $\bar{C}_k$ values is equal to $8\tilde{N}\log_2\tilde{N}$, by assuming that the mean values $\bar{c}_n$ from the CPM decoder are available. Then, given $W_k$, $\tilde{H}_k$, and $\mu$, (4.7) leads to $8\tilde{N}$ real multiplications and $6\tilde{N}$ real additions, and the time-domain symbol estimates are obtained after $4\tilde{N}\log_2\tilde{N}$ real multiplications and additions. Thus, the total number of real multiplications and additions per SIC/equalizer iteration are $12\tilde{N}\log_2\tilde{N}+8\tilde{N}$ and approximately $12\tilde{N}\log_2\tilde{N}+6\tilde{N}$, respectively. Moreover, at the initial equalization iteration, $\tilde{H}_k$ values are computed by at most $4\tilde{N}\log_2\tilde{N}$ real multiplications and additions, whereas the computation of $W_k$ and $\mu$ for the ZAI and FAI scenarios require $10\tilde{N}+4$ real multiplications and $5\tilde{N}$ real additions.

Table 4.1. Complexity of the SISO Modules Used by the Proposed Receiver, the Receivers in Chapter 3 and [23], and TAE

| | FDE | TDE | BFDE [23] | CED [10] | CPM Demodulator | Channel Decoder |
|---|---|---|---|---|---|---|
| Real multiplications and additions | $O(U)+$ $O(n_iU\log_2U)+$ $O(n_iU\mathcal{P}M^L)$ | $O(L_f^3)+$ $O(n_iUL_f)+$ $O(n_iU\mathcal{P}M^L)$ | $O(n_iU^3)+$ $O(n_iU\mathcal{P}M^L)$ | $O(n_iU\mathcal{P}M^{L+M_c-1})$ | $O(n_iU\mathcal{P}M^L)$ | $O(n_iU2^{l_c+1})$ |

$U$, $n_i$, $L_f$, $M_c$, $L$, $M$, $\mathcal{P}$, and $l_c$ denote the block length, number of iterations, length of the TDE filter, length of the multipath channel in terms of symbol intervals, memory length of CPM, modulation order, denominator of the modulation index, and the memory length of the convolutional code, respectively.

The approximate computational complexity for the proposed FDE is presented in Table 4.1, along with the TDE proposed in Chapter 3, the BFDE in [23] and the optimal CED in [10] using the Log-BCJR algorithm. Also included in the table are the complexities of the SISO CPM demodulator and the channel decoder so that the complexity comparisons of different turbo architectures using these blocks can be obtained. Here $n_i$, $M_c=\lfloor L_c/n_s\rfloor+1$, $l_c$, and $L_f$ denote the number of iterations, length of the multipath channel in terms of symbol intervals with $\lfloor . \rfloor$ being the floor operator, the memory length of the convolutional code, and the length of the TDE filters in (3.20) and (3.21) which depend on $L_c$ linearly, respectively. The example below presents the approximate number of real multiplications and additions required throughout a signal block for the proposed turbo receiver with FDE (turbo FDE) in Figure 4.2, the turbo receiver with TDE (turbo TDE) in Figure 3.2 replacing the front-end FDE in Figure

4.2 by the SISO TDE filter introduced in Section 3.1.2, the TLE in [23] in which the BFDE is followed by the CPM demodulator and the channel decoder modules, and the aforementioned TAE which exchanges soft information between the optimal CED module and the channel decoder where both SISO modules employ the Log-BCJR algorithm.

*Example*: It is assumed that $L_d = 126$ data bits are encoded by a rate-1/2 convolutional code so that $L_b = 252$ code bits are obtained, where the memory length of the convolutional code is $l_c = 3$. The parameters for the CPM scheme is $M = 2$, $L = 3$ and $h = 0.5$ with $P = 2$. To apply the proposed turbo FDE and the TLE in [23], a cyclic guard interval is added to the transmitted block. For this purpose, four tail symbols are inserted as shown in Figure 4.1 where $l_e = 2$ and $l_t = 2$, and the length of the modulating sequence is $\bar{N} = 256$. The turbo receivers with time-domain equalization methods in Chapter 3 and [10] do not require tail symbols and cyclic guard addition so that the length of the modulating sequence is $N = 252$. For the multipath fading channel, it is assumed that $L_c = 11$, the channel resolution is $T_s = T/2$ with

Table 4.2. Computational Complexity per Signal Block for the Proposed Receiver, the Turbo Equalizers in Chapter 3 and [23], and TAE

| Receiver | Computational Complexity |
|---|---|
| Turbo FDE with $n_f$ front-end and $n_i$ back-end iterations | $O(n_s\bar{N}) + O(n_f n_s \bar{N} \log_2 n_s\bar{N}) + O(n_f n_s \bar{N}\mathcal{P}M^L) + O(n_i L_b \mathcal{P} M^L) + O(n_i L_b 2^{l_c+1})$ |
| Turbo TDE with $n_f$ front-end and $n_i$ back-end iterations | $O(L_f^3) + O(n_f n_s N L_f) + O(n_f n_s N \mathcal{P} M^L) + O(n_i L_b \mathcal{P} M^L) + O(n_i L_b 2^{l_c+1})$ |
| TLE [23] with $n_i$ iterations | $O(n_i n_s^3 \bar{N}^3) + O(n_i n_s \bar{N} \mathcal{P} M^L) + O(n_i L_b \mathcal{P} M^L) + O(n_i L_b 2^{l_c+1})$ |
| TAE with $n_i$ iterations | $O(n_i N \mathcal{P} M^{L+M_c-1}) + O(n_i L_b 2^{l_c+1})$ |

$N$, $\bar{N}$, $n_s$, $L_f$, $M_c$, $L$, $M$, $\mathcal{P}$, and $l_c$ denote the length of the modulation sequence, length of the modulation sequence with tail symbols, number of samples per symbol period, length of the TDE filter, length of the multipath channel in terms of symbol intervals, memory length of CPM, modulation order, denominator of the modulation index, and the memory length of the convolutional code, respectively.

$n_s = 2$, and, therefore, the maximum tap delay is $5T$. After the addition of the cyclic guard interval, the duration of the transmitted packet is $261T$ with $G = 5$. Thus, the number of extra tail and guard symbols employed by the frequency-domain methods is only $l_e + l_t + G = 9$ compared to the time-domain methods. The computational load for the aforementioned turbo receivers are presented in Table 4.2 by using the approximate complexity values in Table 4.1 for the SISO modules deployed by these

receivers. At the first and second rows of Table 4.2, the complexity values for the turbo FDE and turbo TDE are given, respectively. Using the doubly-iterative structure of these receivers, each of the $n_f$ FITs is followed by $n_i/n_f$ BITs so that $n_i$ BITs are performed in total. As in Section 3.3, the TDE filter length is $L_f = 2L_c$. Because the TLE and TAE cannot perform double iterations, all the SISO modules at these receivers are employed throughout $n_i$ iterations, as presented at the third and fourth rows of Table 4.2, respectively. The number of iterations are set as $n_f = 4$ and $n_i = 12$, which are same as the values used for the BER simulations in the present chapter and Section 3.3.

By using the aforementioned parameter values in Table 4.2, it is observed that the number of computations for the proposed turbo FDE at the first row is fewer than the ones for the turbo TDE at the second row, respectively, by adding only nine extra symbols to the transmitted packet. This is because of the cube complexity that comes from the matrix inversion operation in (3.20) and (3.21) for TDE and the dependency of the filter length $L_f$ on the channel length $L_c$. Note that the redundancy for turbo FDE to add the cyclic prefix increases linearly in longer channel impulse responses without any computational change whereas the turbo TDE encounters higher cube complexity. The complexity of TLE does not depend on the length of the channel impulse response. However it is computationally more demanding compared to the proposed turbo FDE as shown at the third row of Table 4.2, depending on the matrix inversions required by the BFDE at each iteration. Moreover, it is not possible to perform double iterations at this receiver to reduce the complexity for equalization. Last row of Table 4.2 shows that the TAE is also more complex compared to the proposed method. Here the complexity of the optimal CED in [10] applied by TAE increases exponentially with the length of the channel impulse response. For the proposed turbo FDE, the length of channel impulse response does not have impact on the complexity in the expense of adding redundancy which increases linearly with the channel memory length. Furthermore, performance of the turbo FDE is better compared to the turbo TDE and TLE and is close to that of TAE, as shown in Section 4.3.

## 4.2. EXIT Chart Analysis

Convergence behavior of the proposed doubly-iterative receiver with FDE is analyzed using the same method in Section 3.2. The transfer characteristic functions for the SISO modules in Figure 4.2 are shown in Figure 3.3. The method described in Section 2.2.3 to obtain the transfer functions of the SISO decoders at a turbo receiver depends on the availability of uncorrelated *a priori* information at the input of these SISO modules and, therefore, requires the use of an interleaver between the corresponding encoders at the transmitter. However, because interleaving after the CPM modulation destroys the phase continuity, deinterleaving is not applicable between the FDE and CPM demodulator in Figure 4.2. Therefore, the transfer characteristic curve for the FDE is obtained by using the aforementioned average quantities in Section 3.2 which are computed as

$$A_{\mathrm{D}} = \frac{1}{\tilde{N}} \sum_{\ell=1}^{N} \sum_{i=0}^{n_s-1} \left| \sum_{p=0}^{\tilde{S}-1} Y_{i,p} P(y_{n_s\ell-n_s+i} = Y_{i,p}) \right|, \tag{4.15}$$

$$A_{\mathrm{E}} = \frac{1}{\tilde{N}} \sum_{\ell=1}^{N} \sum_{i=0}^{n_s-1} \left| \sum_{p=0}^{\tilde{S}-1} Y_{i,p} P(\hat{y}_{n_s\ell-n_s+i} | y_{n_s\ell-n_s+i} = Y_{i,p}) \right|. \tag{4.16}$$

In (4.16), the probabilities in (4.14) are used where $\mu$ is the symbol gain in (4.6) and $\{\hat{y}_n\}$ are the tilted-phase equalizer outputs obtained from $\{\hat{c}_n\}$ which correspond to the $\tilde{N}$-point IDFT of the FDE outputs $\{\hat{C}_k\}$ in (4.7). $A_{\mathrm{D}}$ and $A_{\mathrm{E}}$ are used as the information measures at the input and output of the equalizer. To obtain the equalizer transfer characteristic curves, sample probabilities $P(y_{n_s\ell-n_s+i} = Y_{i,p})$ in (3.6) from the demodulator are generated artificially for all $Y_{i,p} \in \mathcal{Y}_i$ as described in Section 3.2 by setting the probabilities of the samples corresponding to the $p$th signal as $p_t$ and the rest of the probabilities as $(1-p_t)/(\tilde{S}-1)$ given that the $p$th signal transmitted at the $\ell$th symbol interval, where $1/\tilde{S} \leq p_t \leq 1$, $\ell = 1, \ldots, N$, and $i = 0, \ldots, N_s - 1$. Then $A_{\mathrm{D}}$ is calculated in (4.15). Furthermore, the computed mean values are also employed for the soft interference cancellation, and $A_{\mathrm{E}}$ is found by (4.16) using the FDE outputs. The FDE coefficients are set as (4.12)and (4.13) to obtain the transfer characteristic curves for the zero and perfect *a priori* information scenarios, respectively, which are used

to determine the switching condition between these scenarios. For the demodulator transfer characteristic curves, the FDE outputs in (4.7) are generated artificially as

$$\hat{C}_k := \frac{C_k}{N} \sum_{\ell=0}^{\tilde{N}-1} W_\ell \tilde{H}_\ell + W_k D_k, \tag{4.17}$$

where $\{C_k\}$ multiplied by the gain in (4.6) denote the $\tilde{N}$-point DFT of the signal samples $\{c_n\}$. The FDE coefficients in either (4.12) or (4.13) are used in (4.17) while producing the equalizer outputs artificially. $\{D_k\}$ are the $\tilde{N}$-point DFT of $\{d_n\}$ which are defined similar to the channel noise samples $\{v_n\}$ in (4.4) as the i.i.d. additive Gaussian noise terms each with zero-mean and variance $\sigma_d^2$. Because channel noise terms after low-pass filtering and sampling are assumed to be white at the beginning of this chapter, the elements of $\mathbf{d}_n$ are also generated as white Gaussian random variables. Note that each $d_n$ contains the corresponding channel noise sample $v_n$ as well as the uncancelled interference for the symbol $c_n$. Therefore it is assumed that $\sigma_v^2 \leq \sigma_d^2$ where the equality holds in the case of perfect interference cancellation. The inputs $\{\hat{c}_n\}$ to the probability mapper in Figure 4.2 are obtained by taking the $\tilde{N}$-point IDFT of $\{C_k\}$ generated using the model in (4.17), which are used to obtain the probabilities in (4.14) to be delivered to the demodulator and to compute $A_{\mathrm{E}}$ in (4.16).

As previously shown in Section 3.2, it is more effective in the doubly-iterative architecture to perform back-end demodulator/decoder iterations after each equalizer iteration to improve the demodulator outputs for the next equalizer iteration rather than applying equalizer/demodulator iterations with constant information from the channel decoder. At the back-end of the receiver, CPM demodulator and the channel decoder exchange soft information for the encoded bits, and the convergence behavior between these modules can be observed by using EXIT chart analysis. A two dimensional graph as in [46] can be obtained by considering constant *a priori* information from the equalizer to the demodulator.Moreover, a three dimensional graph as in [47] can also be illustrated to observe the convergence behavior while the *a priori* information from the equalizer improves. In this section, both graphs are obtained by considering the mutual information between the encoded bits and the LLRs at the

output of the demodulator/decoder as described in Section 2.2.3.

In the convergence analysis (and in the BER simulations of the next section), binary 3RC CPM scheme with $L = 3$ and $h = 0.5$ is considered, which employs RC filtering with main lobe width of $L$ symbol duration, as described in [2]. The channel resolution is $T_s = T/2$, number of samples per symbol period is $n_s = 2$, and the two-sided bandwidth of the low-pass filter is $2/T$ so that more than 99.9 percent of the signal energy is recovered [2]. A rate-1/2 convolutional code with generator

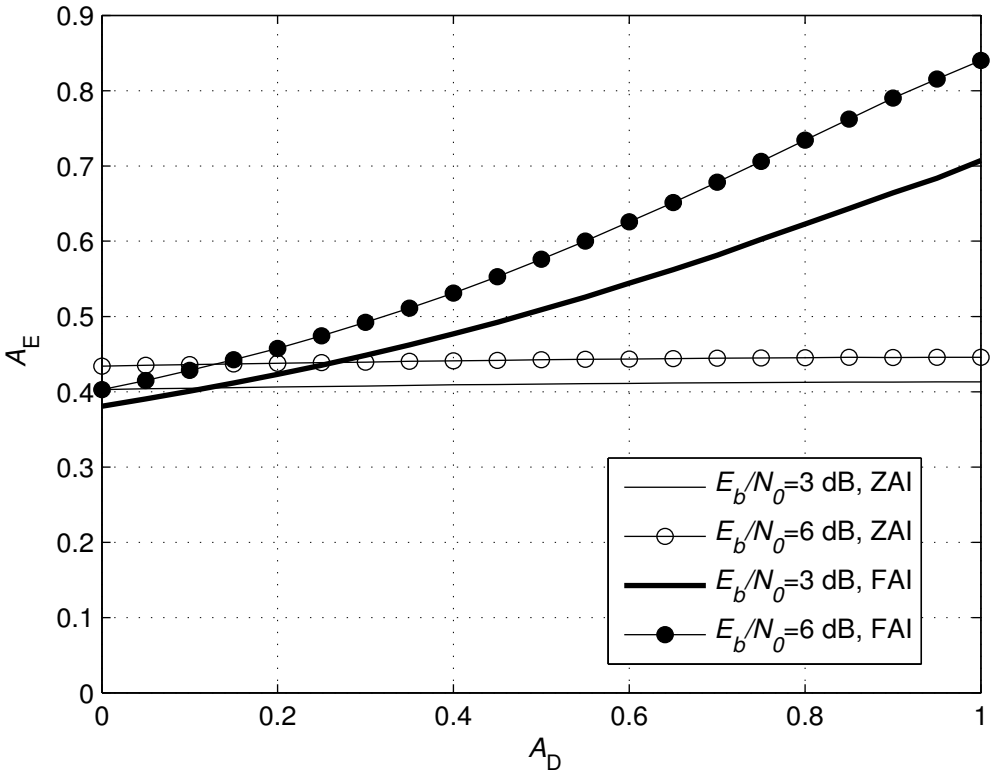



Figure 4.3. Transfer characteristic curves for the SIC/FDE at $E_b/N_0 = 3$ and 6 dB

polynomial $(64, 74)_8$ is used for channel coding [64]. For multipath fading, eleven-tap quasi-static channels where the tap coefficients are zero-mean complex white Gaussian random variables with exponentially decaying power profile are taken into account. The variance of the $l$th path coefficient is $e^{-l/2}/\left(\sum_{m=0}^{10} e^{-m/2}\right)$ and the corresponding path delay is $lT_s$ for $l = 0, 1, \ldots, 10$. The complex channel noise is assumed AWGN with zero mean and variance $\sigma_v^2$.

The transfer characteristic curves of the equalizers under the ZAI and FAI assumptions by averaging the results for the aforementioned eleven-tap quasi-static multipath fading channels are shown in Figure 4.3, where $E_b/N_0 = 3$ and 6 dB. Notice that the FDE coefficients are computed by setting $\bar{C}_k = 0$ under ZAI assumption which is nearly the case at low $A_{\mathrm{D}}$ values. However, as $A_{\mathrm{D}}$ values approach 1, the case converges to the perfect interference cancellation state, implying that $\bar{C}_k = C_k$ eventually. Therefore, the FDE assuming ZAI results in more accurate outputs at low $A_{\mathrm{D}}$'s which becomes the case for the FDE employing (3.21) at high $A_{\mathrm{D}}$'s, as illustrated in Figure 4.3. Therefore, a feasible hybrid strategy for best achievable performance is to employ the former equalizer initially, and then to switch to the latter one as the *a priori* information to the equalizer is improved.

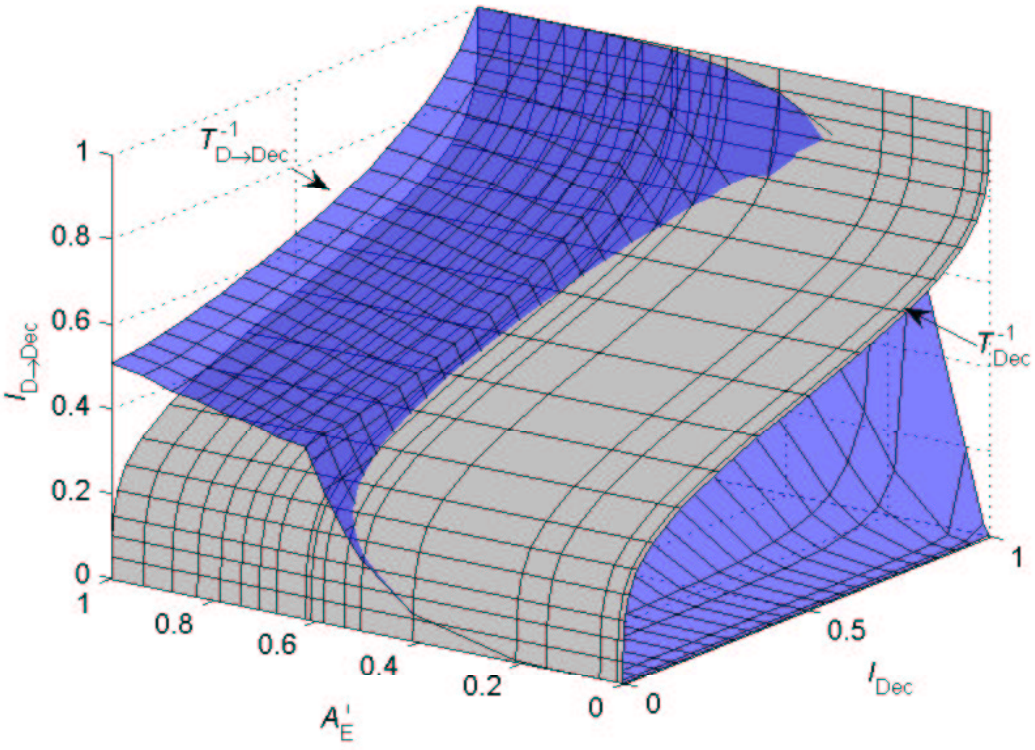



Figure 4.4. EXIT chart analysis for the back-end iterations of the doubly-iterative receiver with FDE

In case of back-end iterations, the demodulator transforms the *a priori* information $\{L_a(\tilde{u}_m)\}$ for the interleaved code bits from the channel decoder to $\{L_e(\tilde{u}_m)\}$, given the tilted-phase CPM signal probabilities from the FDE. LLRs $\{L_a(\tilde{u}_m)\}$ are generated

depending on the model in (2.68), and $I_{\mathrm{Dec}}$ values are computed as in (2.70) using the conditional PDFs in (2.69) belonging to this model, as previously mentioned. After the output conditional PDFs are determined by histogram measurements, $I_{\mathrm{D}\rightarrow\,\mathrm{Dec}}$ is computed in the same way, as the mutual information between the encoded bits and

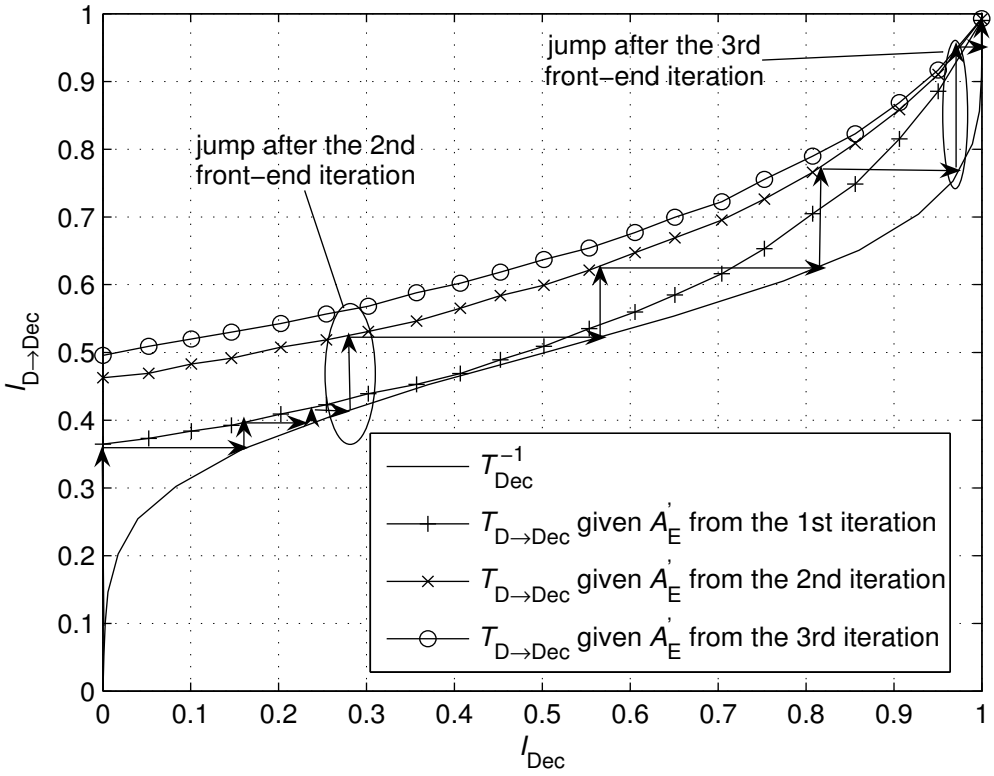



Figure 4.5. Analysis for the front-end and back-end iterations of the doubly-iterative receiver with FDE

the LLRs at the output of the demodulator [46]. Similar procedure is followed to compute $I_{\mathrm{D}\rightarrow\,\mathrm{Dec}}$ and $I_{\mathrm{Dec}}$ at the input and output of the channel decoder, respectively. The three-dimensional plot in Figure 4.4 illustrates the EXIT behavior at $E_b/N_0 = 3$ dB between the demodulator (upper surface) and the decoder for varying information from the FDE. The tilted-phase CPM signal probabilities from the equalizer to the demodulator are computed by using the FDE outputs generated according to the model in (4.17). The switching condition to decide on employing either (4.12) or (4.13) is the same as in Figure 4.3 while generating the equalizer outputs artificially. Since $A_{\mathrm{E}}$ values reach to one only at high SNRs, $A_{\mathrm{E}}^{'} = A_{\mathrm{E}}/\max(A_{\mathrm{E}})$ is used in Figure 4.4 instead of $A_{\mathrm{E}}$ for better presentation purposes, where $\max(A_{\mathrm{E}})$ gives the maximum value for $A_{\mathrm{E}}$. As shown in Figure 4.4, the gap between the demodulator and decoder

surfaces becomes wider as better information is provided by the equalizer, and no bottlenecks are encountered after $A_{\mathrm{E}} = 0.6$. Thus, it is necessary for convergence to terminate back-end iterations after a bottleneck is encountered, and then to perform a new front-end iteration to have a wider gap between the demodulator and decoder curves. In Figure 4.5, starting with the $\sigma_d^2$ value under zero information assumption that corresponds to the first equalizer iteration with no interference cancellation, three back-end iterations can be performed up to the bottleneck, at which the demodulator produces the inputs to the equalizer that generates better signal probabilities for the next set of back-end iterations, where FAI scenario is considered for $A_{\mathrm{D}} > 0.3$. By updating the probabilities from the equalizer following each set of back-end iterations, the convergence is achieved after four front-end iterations.

## 4.3. Simulation Results

In this section, the BER performance of the proposed turbo FDE is presented for different number of front- and back-end iterations, and is also compared to those of the TAE employing the CED in [10], the turbo TDE in Chapter 3, the TLE in [23], and the performance in AWGN channel. The binary 3RC CPM with $L = 3$ and $h = 0.5$ is considered as in [2] with $n_s = 2$, the two-sided bandwidth of the low-pass filter is $2/T$, and the channel resolution is $T_s = T/2$, as in [23]. The rate-1/2 convolutional code with generator polynomial $(64, 74)_8$ is used, and random interleaving is applied. First, the performance gap between the optimal and the proposed receiver is observed in a mild Proakis' A channel with coefficients [0.04 -0.05 0.07 -0.21 -0.5 0.72 0.36 0.00 0.21 0.03 0.07], where the delay of the $m$th path is $mT_s$ for $m = 0, 1, \ldots, 10$. The channel coefficients are normalized to have unit total energy. The aforementioned receivers are also compared in a more severe eleven-tap quasi-static channel (channel I) environment with deep spectral nulls, where the tap coefficients are zero-mean complex white Gaussian random variables with exponentially decaying power profile such that the variance of the $m$th path coefficient is $e^{-m/2}/\left(\sum_{l=0}^{10} e^{-l/2}\right)$ and the corresponding path delay is $mT_s$ for $m = 0, 1, \ldots, 10$. Furthermore, the six-tap typical urban channel (channel II) model in [22] is considered, where the variances of the complex Gaussian path coefficients are [0.189 0.379 0.255 0.090 0.055 0.032] and the corresponding path

delays are $[0\ T_s\ 2T_s\ 8T_s\ 12T_s\ 25T_s]$. For all the scenarios considered, the information packets start and terminate at the zero state and consist of 256 symbols including the tail coefficients with $l_e = 2$ and $l_t = 2$. For channel I and II, the duration of the cyclic guard intervals is $G = 5$ and $G = 13$ symbol periods, respectively. The switching condition between ZAI and FAI coefficients is determined by using the corresponding transfer characteristic curves of the FDE in Figure 4.3.

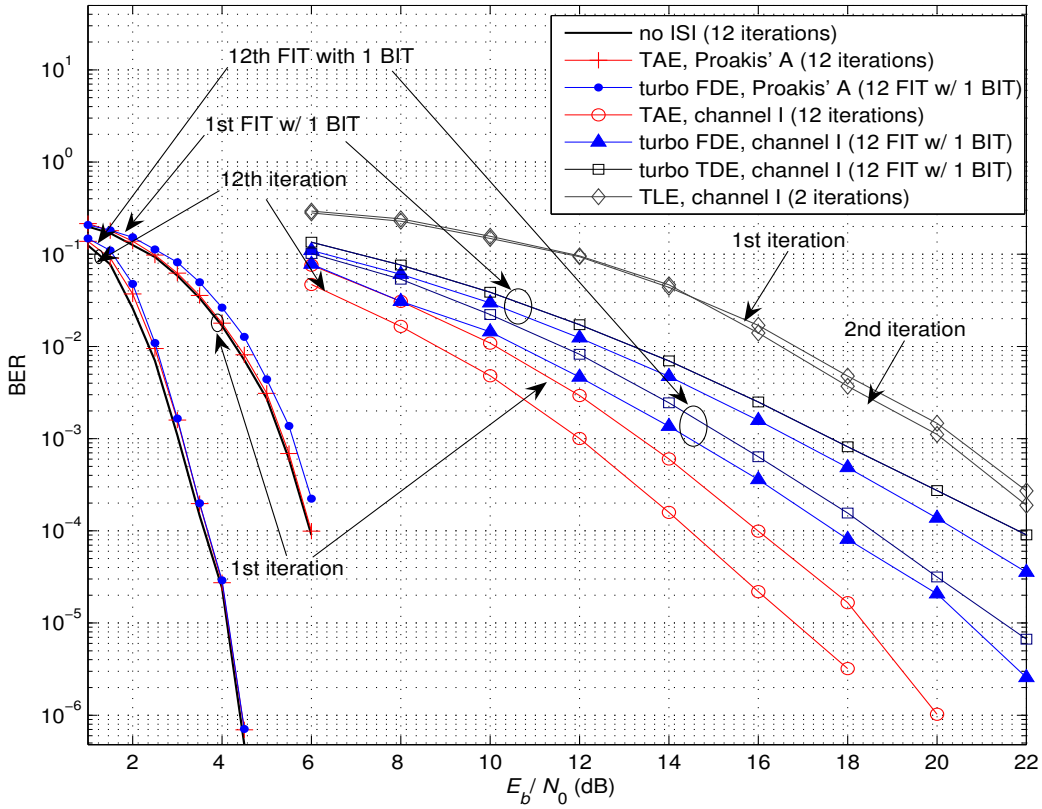



Figure 4.6. BER performance for no ISI, Proakis' A channel and channel I

In Figure 4.6, the BER performance of turbo FDE with respect to TAE is depicted for Proakis' A channel and channel I. Moreover, the performance of turbo FDE in channel I is compared to those of turbo TDE and TLE. Both turbo FDE and TDE exploit double iterations where each FIT is followed by one BIT between the CPM demodulator and the channel decoder. For TLE, the channel decoder feeds soft information to the front-end at each iteration, where there is no significant turbo gain after two iterations, as also described in [23]. The TAE conducts twelve iterations between

the optimal CED and the channel decoder. In AWGN channel scenario, the demodulator and the decoder exchange soft information by performing twelve iterations. The proposed receiver yields very close performance compared to TAE in the mild Proakis' A channel. In more severe channels with deep spectral nulls such as the ones in channel I scenario, TAE performs much better at the expense of large complexity as shown by the last row of Table 4.2. The turbo FDE performs better than turbo TDE and TLE with less computations which can be verified by comparing the computational load at the first row with those at the second and third rows of Table 4.2, respectively, as also described by the example at the end of Section 4.1.3.

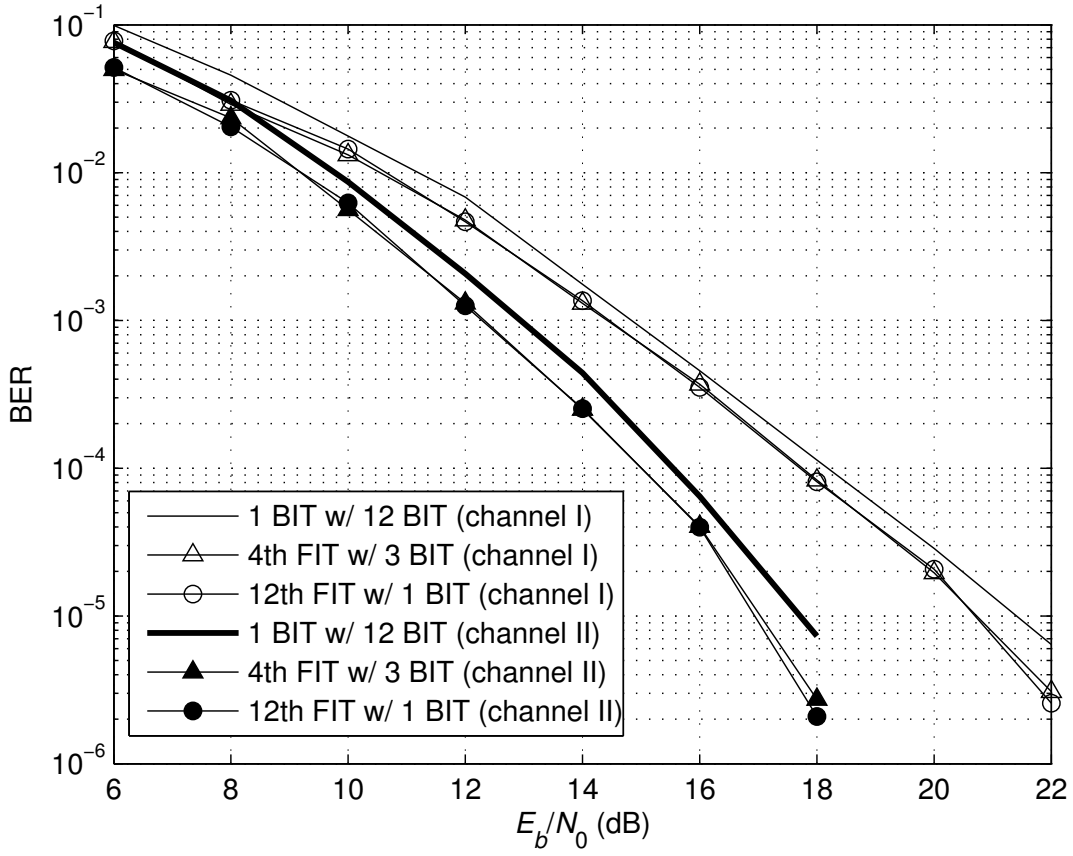



Figure 4.7. BER performance of turbo FDE in channels I and II

The complexity of the proposed receiver can be further reduced by feeding *a priori* information to the SIC/equalizer after a few back-end iterations, as shown in Figure 4.7. For both channel I and II, four FITs where each one is followed by three BITs result in the same performance compared to twelve FITs where each one is followed

by one FIT, while the equalizer complexity is three times less for the former scenario. Moreover, by exploiting the SISO capability of FDE, the performance gain of the aforementioned scenarios compared to one FIT followed by twelve BITs is about 1 dB after BER$= 1 \times 10^{-5}$ in both channels I and II.

# 5. ORTHOGONAL ST BLOCK CODING OF CPM ON MULTIPATH FADING CHANNELS

This chapter presents an ST block coding scheme which preserves the spectral efficiency of CPM perfectly and results in significant diversity gain for the frequency-domain equalization of CPM signals transmitted over the multipath fading channels. Contrary to the methods in [24]-[29] which operate in flat fading channels and depend on the ST coding of the information symbols before the CPM modulation to maintain the phase continuity, the proposed method apply ST block coding to CPM waveforms by assuming slowly-varying multipath fading channels which are almost constant throughout two signal blocks. For this purpose, the scheme in [31] is enhanced to maintain the bandwidth efficiency of CPM so that tail symbols are used to prevent the phase discontinuities during the interblock transitions. Depending on the orthogonality of the proposed scheme, the receiver complexity remains unchanged whereas extra computations are required at the receiver for the methods in [24]-[29] which can be viewed to be equivalent to ST trellis codes. Similar to the proposed method, ST coding in [30] is also applied directly to the CPM waveforms rather than the information symbols. However, the method in [30] is not applicable in multipath fading channels and it cannot attain the exact phase continuity during the interblock transitions which yields that the spectral efficiency cannot be maintained perfectly.

The proposed scheme employs two transmit antennas. After the appropriate low-pass filtering and sampling, the doubly-iterative receiver with FDE in Chapter 4 is applied as in case of single antenna transmissions depending on the orthogonal ST combining. As shown in Figure 4.2, the receiver consists of a front-end soft-information aided linear FDE filter, a central CPM demodulator, and a back-end channel decoder. The demodulator computes soft information on both the CPM signals and the code bits. Then, these two soft outputs are employed in a doubly-iterative information exchange where the demodulator is coupled with both the FDE filter and the decoder. The aforementioned receiver is preferred for its higher performance and lower complexity

compared to its counterpart in [23]. By using only one more transmit antenna to apply the proposed ST block coding, it also attains superior performance and less complexity than TAE coupling the optimal CED module in [10] with a back-end SISO decoder for the turbo equalization of the coded CPM, as also verified by BER simulations.

The remainder of this chapter is organized as follows. Section 5.1 describes the proposed ST block coding scheme and presents the orthogonal combining at the receiver with the corresponding FDE filter coefficients. The simulation results are in Section 5.2.

## 5.1. Orthogonal ST Block Coding of CPM for Frequency-Domain Equalization

The method in [31] combines the ST block coding with frequency-domain equalization for linear modulations by modifying the Alamouti scheme proposed in [68]. Denoting $\mathbf{s}_{i,b}(n)$ as the $n$th symbol at the $b$th block transmitted from the $i$th antenna with $n = 0, 1, \ldots, N-1$, $b = 0, 2, 4, \ldots$, and $i \in \{1, 2\}$, the aforementioned scheme is applied as

$$\begin{aligned} \mathbf{s}_{1,b+1}(n) &= -\mathbf{s}^*_{2,b}((-n)_N), \\ \mathbf{s}_{2,b+1}(n) &= \mathbf{s}^*_{1,b}((-n)_N) \end{aligned} \tag{5.1}$$

where $(\cdot)^*$ and $(\cdot)_N$ are the complex conjugate and modulo$-N$ operations, respectively. Then, to eliminate the interblock interference (IBI) and to obtain a simple representation for FDE, a length-$G$ cyclic prefix is appended to each block where $G = \max_{1 \le i \le 2} \lceil \tau_{N_{c,i}-1,i}/T \rceil + 1$ with $\lceil \cdot \rceil$ being the ceiling operation. When the ST coding defined by (5.1) is applied directly to the CPM signal in (2.1), the phase functions that correspond to the first and second antennas before appending the cyclic prefix are

computed as

$$\varphi(t+NT,\mathbf{x}_{1,b+1}) = -\varphi((-t)_{NT},\mathbf{x}_{2,b}) + \pi,$$
$$\varphi(t+NT,\mathbf{x}_{2,b+1}) = -\varphi((-t)_{NT},\mathbf{x}_{1,b}), \tag{5.2}$$

respectively, which lead to

$$c(t+NT,\mathbf{x}_{1,b+1}) = -c^*((-t)_{NT},\mathbf{x}_{2,b}),$$
$$c(t+NT,\mathbf{x}_{2,b+1}) = c^*((-t)_{NT},\mathbf{x}_{1,b}), \tag{5.3}$$

respectively, where $0 \leq t \leq NT$ and $\mathbf{x}_{i,b}$ is the length-$N$ symbol sequence for the CPM modulation of the $b$th block at the $i$th transmit antenna. As shown in (5.2), for each antenna, the phase representation at the $(b+1)$th block is negative and is also reversed in time compared to the phase representation at the $b$th block. Thus, it is not possible to apply the ST coding in (5.2) without phase discontinuities during the interblock transitions since the modulation procedure defined in (2.2) is not maintained. Also the method in [30] cannot preserve the phase continuity perfectly depending on a similar inconsistency. To circumvent this problem, a new scheme must be applied. For this purpose, both of the length-$N$ symbol sequences to be demodulated in two block durations, which can be denoted as $\mathbf{x}_1$ and $\mathbf{x}_2$, respectively, are modified by the proposed scheme to transmit appropriate CPM signals from each antenna without any phase discontinuities as encountered during the interblock transitions in (5.2) and to obtain a discrete representation similar to (5.1) after appropriate processing at the receiver.

The proposed ST block coding scheme is described in Section 5.1.1 and the modifications for the FDE algorithm in Chapter 4 are presented in Section 5.1.2.

### 5.1.1. ST Block Coding for CPM

In order to apply ST block coding and insert appropriate cyclic guard intervals to make the application of FDE in Chapter 4 possible while maintaining the phase

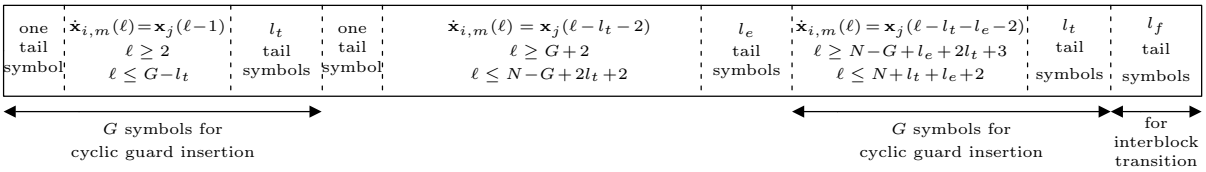



Figure 5.1. Modulating sequence for the ST block coding scheme with the cyclic prefix

continuity, $\mathbf{x}_1$ and $\mathbf{x}_2$ are modified according to the format illustrated in Figure 5.1 where $\dot{\mathbf{x}}_{i,m}$ denotes the new symbol sequence used by CPE to obtain the $m$th signal block at the $i$th transmit antenna with $m \in \{b, b+1\}$ and $i \in \{1,2\}$, and $j \in \{1,2\}$. First element of $\dot{\mathbf{x}}_{1,b}$ is a tail symbol to stay at the zero state in (2.19) where the initial state for the CPE trellis is also zero. After the first symbol, proceeding $G - l_t - 1$ elements of $\dot{\mathbf{x}}_{1,b}$ are set to be equal to the first $G - l_t - 1$ symbols in $\mathbf{x}_1$ as Figure 5.1 implies. Then $l_t + 1$ tail symbols are used to return to and stay at the zero state. For $G + 2 \leq \ell \leq N - G + 2l_t + 2$, the sequence elements are set as $\dot{\mathbf{x}}_{1,b}(\ell) = \mathbf{x}_1(\ell - l_t - 2)$ and, after that, $l_e \geq l_t$ tail symbols are used to return to and stay at the zero state. Last $G - l_t$ symbols in $\mathbf{x}_1$ are exploited to obtain $\dot{\mathbf{x}}_{1,b}(\ell) = \mathbf{x}_1(\ell - l_t - l_e - 2)$ where $N - G + l_e + 2l_t + 3 \leq \ell \leq N + l_t + l_e + 2$. Then $l_t$ tail symbols are used to return to the zero state which is followed by $l_f \geq l_t$ tail symbols to go to and stay at the state in (2.20) where the cumulative tilted phase is equal to $\pi$ rather than zero. Similar procedure is applied to obtain $\dot{\mathbf{x}}_{2,b+1}$ and $\dot{\mathbf{x}}_{2,b}$ using $\mathbf{x}_1$ and $\mathbf{x}_2$, respectively, whereas the only difference is employing $l_f$ tail symbols at the end to stay at the zero state. The sequence $\dot{\mathbf{x}}_{2,b}$ is produced by using $\mathbf{x}_2$ where the initial state for the CPE trellis is set as the state in (2.20) with first tail symbol keeping the trellis path at the same state. Then $l_t+1$ and $l_e$ tail symbols shown in Figure 5.1 are used to return to and stay at the state in (2.20) rather than the zero state. Furthermore, $l_t$ tail symbols return the trellis path to the state in (2.20), whereas the last $l_f$ tail symbols are applied to go to and stay at the zero state. The proposed ST block coding scheme requires the time-reversal of the first $\bar{N} := N + 2l_t + l_e + 2$ symbols at the second antenna transmissions. That is

why the tail symbols to make the insertion of a cyclic guard interval possible without phase discontinuities are applied at both the beginning and end of the symbol sequence in Figure 5.1, which is not the case for single antenna transmissions as shown in Figure 4.1. Denoting the overall block length with the cyclic prefix as $N' := \bar{N} + l_f + G$, $l_e$ and $l_f$ are set properly so that $h(M-1)\bar{N}$ and $h(M-1)N'$ is an even number which yields that $(\pi h(M-1)\bar{N})_{2\pi} = (\pi h(M-1)N')_{2\pi} = 0$. Depending on this property and after appending the cyclic guard intervals, the CPM phase functions for each antenna and block which are obtained from the corresponding tilted-phase functions using the relation in (2.15) are equal to

$$\begin{aligned}
\varphi_{1,b}(t) &:= \varphi(t + (\bar{N} - G)T, \dot{\mathbf{x}}_{1,b}), \\
\varphi_{1,b+1}(t + N'T) &:= \varphi(t + (N' + \bar{N} - G)T, \dot{\mathbf{x}}_{1,b+1}), \\
\varphi_{2,b}(t) &:= -\varphi(-t + GT, \dot{\mathbf{x}}_{2,b}), \\
\varphi_{2,b+1}(t + N'T) &:= -\varphi(-t + (N' + G)T, \dot{\mathbf{x}}_{2,b+1}),
\end{aligned} \tag{5.4}$$

on the interval $0 \leq t \leq GT$,

$$\begin{aligned}
\varphi_{1,b}(t) &:= \varphi(t - GT, \dot{\mathbf{x}}_{1,b}) = -\varphi_{2,b+1}(-t + (N' + \bar{N} + G)T), \\
\varphi_{1,b+1}(t + N'T) &:= \varphi(t + (N' - G)T, \dot{\mathbf{x}}_{1,b+1}) = -\varphi_{2,b}(-t + (\bar{N} + 2G)T) + \pi, \\
\varphi_{2,b}(t) &:= -\varphi(-t + (\bar{N} + G)T, \dot{\mathbf{x}}_{2,b}), \\
\varphi_{2,b+1}(t + N'T) &:= -\varphi(-t + (N' + \bar{N} + G)T, \dot{\mathbf{x}}_{2,b+1}),
\end{aligned} \tag{5.5}$$

on the interval $GT \leq t \leq (\bar{N} + G)T$, and

$$\begin{aligned}
\varphi_{1,b}(t) &:= \varphi(t - GT, \dot{\mathbf{x}}_{1,b}), \\
\varphi_{1,b+1}(t + N'T) &:= \varphi(t + (N' - G)T, \dot{\mathbf{x}}_{1,b+1}), \\
\varphi_{2,b}(t) &:= -\varphi(-t + (\bar{N} + G)T, \dot{\mathbf{x}}_{2,b}), \\
\varphi_{2,b+1}(t + N'T) &:= -\varphi(-t + (N' + \bar{N} + G)T, \dot{\mathbf{x}}_{2,b+1}),
\end{aligned} \tag{5.6}$$

on the interval $(\bar{N}+G)T \leq t \leq N'T$, where $\bar{N} = N+2l_t+l_e+2$ and $N' = \bar{N}+G+l_f$ as mentioned previously, and it is assumed that $b = 0$ for simplicity in the presentation. For all phase functions in (5.4)-(5.6), phase continuity is maintained since it is assured by tail symbols in Figure 5.1 that the CPE trellis path terminates at and continues from the same state at $t = 0$, $t = GT$, $t = (\bar{N} + G)T$, and $t = N'T$. Because the proposed scheme applies time-reversal and negative sign to the phase functions throughout all blocks at the second antenna, no phase discontinuities are encountered, whereas these operations are applied only during the $(b+1)$th block at both antennas in (5.2) which result in phase discontinuities at interblock transitions. Furthermore, as shown in Appendix C, phase functions for the second antenna in (5.4)-(5.6) can be obtained by applying a modulation procedure similar to the one in (2.2) so that there is no requirement at the transmitter to store and reverse the real-time signals.

Using the phase functions above, corresponding ST-block coded CPM signals are produced for $b = 0$ as

$$\begin{aligned} c_{1,b}(t) &:= e^{j\varphi_{1,b}(t)}, \\ c_{1,b+1}(t+N'T) &:= e^{j\varphi_{1,b+1}(t+N'T)}, \\ c_{2,b}(t) &:= e^{j\varphi_{2,b}(t-T_s)}, \\ c_{2,b+1}(t+N'T) &:= e^{j\varphi_{2,b+1}(t-T_s+N'T)}, \end{aligned} \tag{5.7}$$

respectively, on the interval $0 \leq t \leq N'T$, where $T_s = T/n_s$ is the period for sampling to get a discrete representation at the receiver with $n_s$ being the number of samples at each symbol interval. By using the properties of the symbol sequences shown in Figure 5.1 and the phase functions in (5.4)-(5.6), the signals in (5.7) lead to

$$\begin{aligned} c_{1,b}(nT_s + T_s/2 + GT) &= \mathbf{c}_1(n), \\ c_{1,b+1}(nT_s + T_s/2 + GT) &= -\mathbf{c}_2(n), \\ c_{2,b}(nT_s + T_s/2 + GT) &= \mathbf{c}_2^*((-n)_{\tilde{N}}), \\ c_{2,b+1}(nT_s + T_s/2 + GT) &= \mathbf{c}_1^*((-n)_{\tilde{N}}), \end{aligned} \tag{5.8}$$

respectively, for $n = 0, 1, \ldots, \tilde{N} - 1$ where $\tilde{N} = n_s \bar{N}$. Depending on the discrete representation in (5.8), after the appropriate low-pass filtering and sampling, and then the cyclic guard interval at the beginning and the last $l_f$ transition periods at the end of each block, the $\tilde{N}$-point DFT of the samples of the received signals at the $b$th and $(b+1)$th blocks are found as

$$\begin{aligned} \mathbf{R}_b &= \mathbf{\Lambda}_1 \mathbf{C}_1 + \mathbf{\Lambda}_2 \mathbf{C}_2^* + \mathbf{V}_b, \\ \mathbf{R}_{b+1} &= -\mathbf{\Lambda}_1 \mathbf{C}_2 + \mathbf{\Lambda}_2 \mathbf{C}_1^* + \mathbf{V}_{b+1} \end{aligned} \tag{5.9}$$

where $\mathbf{R}_b$ is the $\tilde{N} \times 1$ vector of DFT coefficients for the signal samples at the $b$th block, $\mathbf{\Lambda}_i$ is a $\tilde{N} \times \tilde{N}$ diagonal matrix whose $(k,k)$th entry is equal to the $k$th coefficient after taking the DFT of $[\tilde{h}_{0,i}, \tilde{h}_{1,i}, \ldots, \tilde{h}_{L_c-1,i}, \mathbf{0}_{1\times(\tilde{N}-L_c)}]$ with $\tilde{h}_{l,i}$, $i \in \{1,2\}$, $l = 0, 1, \ldots, L_c - 1$,being the $l$th channel path gain for the $i$th antenna, $\mathbf{C}_j$ is the $\tilde{N} \times 1$ vector of DFT coefficients for $\mathbf{c}_j$ in (5.8) with $j \in \{1,2\}$, and $\mathbf{V}_b$ is the vector of the DFT coefficients for the additive white Gaussian noise (AWGN) terms at the $b$th block interval with zero mean and the variance being equal to $\sigma_v^2$. Then by applying the orthogonal ST combining as

$$\mathbf{R} = \begin{bmatrix} \mathbf{\Lambda}_1^* \mathbf{R}_b + \mathbf{\Lambda}_2 \mathbf{R}_{b+1}^* \\ \mathbf{\Lambda}_2 \mathbf{R}_b^* - \mathbf{\Lambda}_1^* \mathbf{R}_{b+1} \end{bmatrix} = \begin{bmatrix} \mathbf{\Lambda} & 0 \\ 0 & \mathbf{\Lambda} \end{bmatrix} \begin{bmatrix} \mathbf{C}_1 \\ \mathbf{C}_2 \end{bmatrix} + \begin{bmatrix} \tilde{\mathbf{V}}_1 \\ \tilde{\mathbf{V}}_2 \end{bmatrix} \tag{5.10}$$

$\mathbf{C}_1$ and $\mathbf{C_2}$ are decoupled without the loss of optimality, where the $(k,k)$th entry of the $\tilde{N} \times \tilde{N}$ diagonal matrix $\mathbf{\Lambda}$ is equal to $|\mathbf{\Lambda}_1(k,k)|^2 + |\mathbf{\Lambda}_2(k,k)|^2$ and $\tilde{\mathbf{V}}_j$ is the noise vector added to the $j$th block of signal to be equalized, which has an autocorrelation matrix being equal to $\tilde{N}\sigma_v^2 \mathbf{\Lambda}$.

### 5.1.2. Frequency-Domain Equalization for ST Block-Coded CPM

After the ST combining in (5.10), MMSE FDE filtering in Chapter 4 is applied as in case of single antenna transmission with the same computational complexity. The only differences are replacing the channel coefficients with $\mathbf{\Lambda}(k,k)$ and setting the noise variance as $\tilde{N}\sigma_v^2 \mathbf{\Lambda}(k,k)$ while computing the $k$th MMSE filter coefficient in the

frequency domain, where the application of SIC/MMSE FDE filtering to (5.10) as in (4.7) leads to

$$\begin{bmatrix} \hat{\mathbf{C}}_1 \\ \hat{\mathbf{C}}_2 \end{bmatrix} = \begin{bmatrix} \mathbf{W} & 0 \\ 0 & \mathbf{W} \end{bmatrix} \mathbf{R} - \begin{bmatrix} \mathbf{W} & 0 \\ 0 & \mathbf{W} \end{bmatrix} \begin{bmatrix} \mathbf{\Lambda} & 0 \\ 0 & \mathbf{\Lambda} \end{bmatrix} \begin{bmatrix} \bar{\mathbf{C}}_1 \\ \bar{\mathbf{C}}_2 \end{bmatrix} + \mu \begin{bmatrix} \bar{\mathbf{C}}_1 \\ \bar{\mathbf{C}}_2 \end{bmatrix} \tag{5.11}$$

where the $(k,k)$th entry of the $\tilde{N} \times \tilde{N}$ diagonal matrix $\mathbf{W}$ is equal to $\mathbf{W}(k,k) = W_k$ being the $k$th FDE coefficient. In (5.11), $\bar{\mathbf{C}}_j(k)$ is the $k$th coefficient after taking the $\tilde{N}$-point DFT of the $\tilde{N} \times 1$ vector $\bar{\mathbf{c}}_j$, $j \in \{1,2\}$, containing the mean values for the $j$th block of signal samples which are produced by the CPM demodulator as in Figure 4.2. Furthermore, the symbol gain $\mu$ is computed as in (4.6) leading to

$$\mu = \frac{1}{\tilde{N}} \sum_{k=0}^{\tilde{N}-1} \mathbf{W}(k,k)\mathbf{\Lambda}(k,k). \tag{5.12}$$

Using the doubly-iterative structure presented in Section 4.1.1, the FDE filter coefficients must be updated at each equalizer iteration since $\bar{\mathbf{C}}_i$ changes at each iteration. However this complexity is reduced as described in Section 4.1.1 and Appendix B by computing two different sets of equalizer coefficients under either FAI or ZAI scenarios which correspond to $\bar{\mathbf{C}}_j = \mathbf{0}_{\tilde{N}\times 1}$ and $\bar{\mathbf{C}}_j = \mathbf{C}_j$, respectively, and by starting the initial FDE iterations with the ZAI coefficients and then switching to the FAI coefficients after a few iterations. Using the same procedure described in Appendix B by replacing $\tilde{H}_k$ with $\mathbf{\Lambda}(k,k)$ and updating the variance of the $k$th additive noise term in the frequency domain as $N\sigma_v^2\mathbf{\Lambda}(k,k)$, the FDE coefficients after the ST combining are computed under the ZAI and FAI assumptions as

$$\mathbf{W}^{\text{ZAI}}(k,k) = \frac{1}{\mathbf{\Lambda}(k,k) + \sigma_v^2}\ , \tag{5.13}$$

$$\mathbf{W}^{\text{FAI}}(k,k) = \frac{1}{\tilde{N}\sigma_v^2 + (1/\tilde{N})\sum_{m=0}^{\tilde{N}-1}\mathbf{\Lambda}(m,m)}\ , \tag{5.14}$$

respectively. The equalizer outputs $\tilde{\mathbf{c}}_1$ and $\tilde{\mathbf{c}}_2$ in time domain are obtained by applying $\tilde{N}$-point IDFT operation to $\hat{\mathbf{C}}_1$ and $\hat{\mathbf{C}}_2$, respectively, which are exploited to compute

sample probabilities in (4.14) delivered to the demodulator for each signal block. The switching condition from the ZAI to FAI coefficients are determined by comparing the transfer characteristic curves of the FDE filter for each scenario, as in Figure 4.3 by computing $A_{\mathrm{D}}$ and $A_{\mathrm{E}}$ as in (4.15) and (4.16), respectively, where the mean values from the CPM demodulator are generated artificially as described in Section 4.2. The convergence analysis for back-end iterations is also the same as in Section 4.2.

## 5.2. Simulation Results

In this section, the BER performance of the proposed orthogonal ST block coding scheme for CPM which is combined with the turbo FDE method in Chapter 5 is presented for different number of front- and back-end iterations, and is also compared

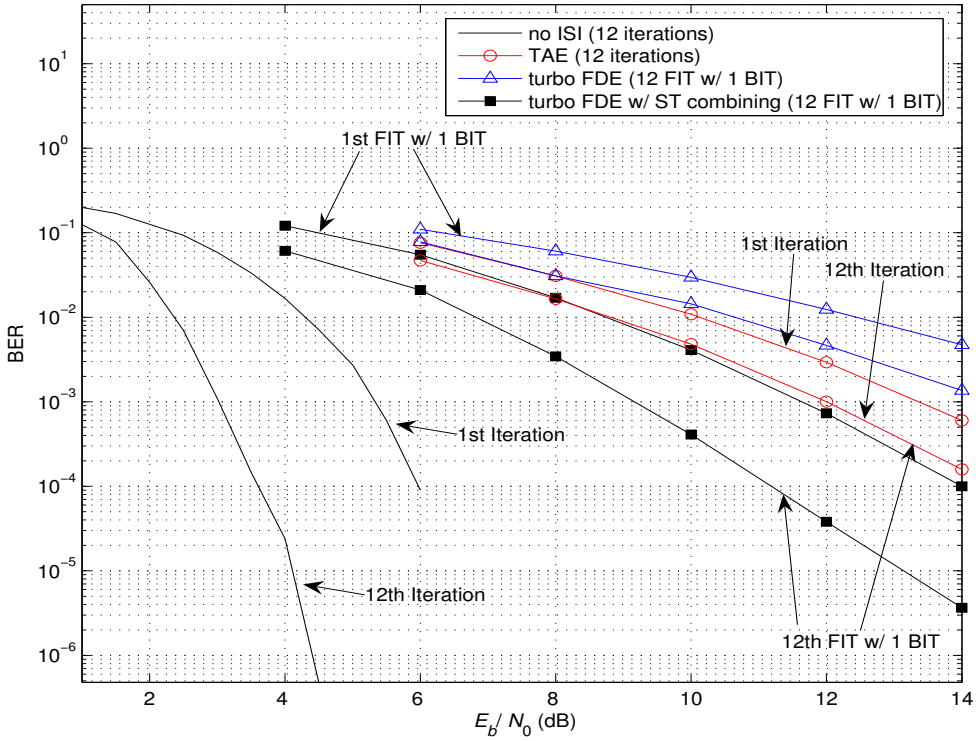



Figure 5.2. BER performance for the turbo FDE with/without ST combining, TAE, and no ISI scenario

to the case without ST combining, to the performance of TAE cascading the SISO optimal CED module in [10] with a back-end channel decoder, and to the performance for the coded CPM in AWGN channel where the receiver consists of a SISO demodulator

followed by a SISO decoder. The 3RC CPM with $L = 3$ and $h = 0.5$ is considered as in [2] with $n_s = 2$, the two-sided bandwidth of the low-pass filter is $2/T$, and the channel resolution is $T_s = T/2$, as in [23]. The rate-1/2 convolutional code with generator polynomial $(64, 74)_8$ is used and random interleaving is applied. The aforementioned methods with turbo equalizers are compared in an eleven-tap quasi-static channel environment, where the tap coefficients are zero-mean complex white Gaussian random variables with exponentially decaying power profile such that the variance of the $m$th path coefficient is $e^{-m/2}/\left(\sum_{l=0}^{10} e^{-l/2}\right)$ and the corresponding path delay is $mT_s$ for $m = 0, 1, \ldots, 10$.

In Figure 5.2, the BER performance of the turbo FDE with the ST combining is compared to the those of the turbo FDE without the ST combining and the TAE by using the aforementioned multipath fading channels. The turbo FDE exploits double iterations where each FIT is followed by one BIT between the CPM demodulator and

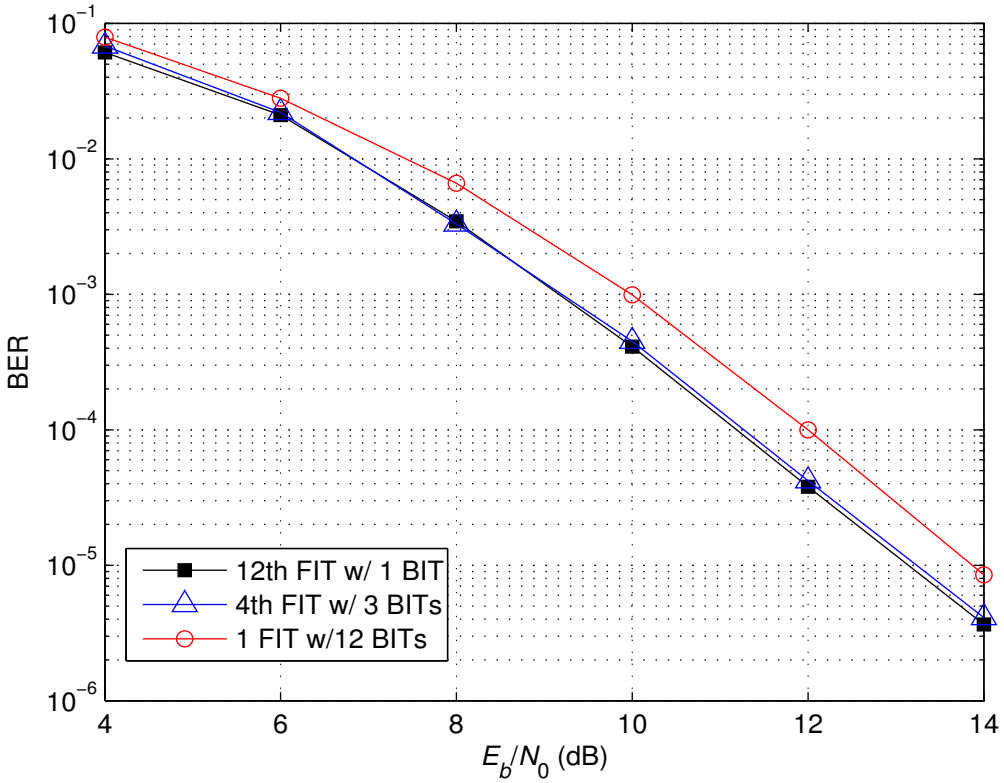



Figure 5.3. BER performance for the turbo FDE with ST combining

the channel decoder whether the proposed ST coding scheme is applied or not. The

TAE conducts twelve iterations between the optimal CED and the channel decoder. In AWGN channel scenario, the demodulator and the decoder exchange soft information by performing twelve iterations. As shown in Figure 5.2, after applying the ST block coding scheme, the error performance of the turbo FDE is improved significantly where the performance gap is almost 5 dB at BER= $1 \times 10^{-3}$ after the twelve FITs with each being followed by one BIT. Furthermore, the performance of the turbo FDE with ST coding is also much better than that of the TAE in the expense of deploying only one more transmit antenna. On the other hand, the receiver complexity for TAE is exponentially increasing by the length of the channel because of the trellis-based CED module it employs. The complexity for the FDE filter is independent of the channel memory.

The complexity of the proposed receiver can be further reduced by feeding *a priori* information to the SIC/equalizer after a few BITs, as shown in Figure 5.3. For the eleven-tap multipath fading channels, four FITs where each one is followed by three BITs result in the same performance compared to twelve FITs where each one is followed by one BIT, while the equalizer complexity is three times less for the former scenario, as in Section 4.3. Moreover, by exploiting the SISO capability of FDE, the performance gain of the aforementioned scenarios compared to one FIT followed by twelve BITs is about 0.75 dB after BER= $1 \times 10^{-3}$. In this way, the overall complexity of the turbo FDE is reduced while its performance with ST coding is significantly better than TAE.

# 6. ST PRE-EQUALIZATION OF CPM ON MULTIPATH FADING CHANNELS

Optimal joint equalization and demodulation of CPM on frequency-selective multipath fading channels entails an intensive search over a single super trellis, which combines the memory effects of both the modulator and the intersymbol interference (ISI) channel [10]. Application of the reduced-state adaptive trellis search algorithms as in [16, 17] for the joint detection of CPM results in lower complexity and does not require channel state information (CSI). However, the computational load could still be prohibitively large to obtain a good performance for channels with long impulse responses. To circumvent the complexity limitations of the aforementioned methods, the receivers proposed in Chapter 3 and 4, [18], [22], and [23] separate the equalization and demodulation functions and employ a linear equalizer at the front-end before the trellis-based CPM demodulation.

Application of channel precoding (or pre-equalization) at the transmitter reduces the complexity further for receivers with limited resources [32]. TH-type precoders in [33, 34] employ modulo-arithmetic operations to maintain the stability of the transmitter, whereas direct application of the TH method to phase-modulated waveforms results in large envelope fluctuations and destroys the spectral efficiency. As previously mentioned, dimension partitioning is applied to MSK in [36]. However, this type of pre-equalization is not applicable to other CPM schemes in general since they cannot be represented by square signal constellations. Furthermore, frequency-domain pre-equalizers in [37] and [38], and combined equalizers in [39] and [40] that consider pre-equalization at the transmitter and post-equalization at the receiver to increase the channel capacity rather than to reduce the receiver complexity cannot manage to maintain the spectral efficiency of CPM since they result in variations in the signal envelope and discontinuities in the signal phase. Although the precoders proposed for CPM in [41]-[45] exhibit good spectral efficiency, these methods aim to equalize the inherent ISI due to modulation memory and are not applicable for multipath channels.

This chapter presents a ST pre-equalization scheme for CPM which maintains the spectral efficiency while mitigating the ISI effects of the multipath fading channels. By applying a selection diversity technique, one of the antennas is chosen for the transmission of the CPM signal while the rest of the antennas are used to transmit the precoded signals to suppress the ISI. The signals for ISI cancellation are shaped as the CPM signal added to a residual signal with small envelope variations such that the narrow-band property of CPM is satisfied by attaining a PAPR close to one. The proposed method considers a time-division duplex (TDD) system where the transmitter and the receiver operate alternately in the same frequency band. Then, by assuming a slowly-varying multipath fading process that is approximately constant throughout two data packets, channel information that is obtained from the received packets is used to pre-equalize the transmitted packets since the forward and reverse radio frequency (RF) links are reciprocal according to the reciprocity theorem [69, 70]. The proposed scheme depends on the approximation of CPM signals by using nSnOEE in [57], which provides high accuracy and low complexity by employing a few basis functions as described in Section 2.1.2. For pre-equalization, the ISI is computed and projected onto the basis functions, where the projection coefficients are truncated using modulo-arithmetic operations as in TH-type precoding to ensure stability. In the modulo operations, a scaling parameter is employed to shorten the range of values for the truncated coefficients, which is computed depending on the proposed transmit selection diversity scheme. Then, the truncated projection coefficients are used to obtain the spectrally-efficient signals for ISI cancellation. At the receiver, perfect synchronization is assumed, and a bank of filters matched to the aforementioned basis functions is employed. The only channel information that must be determined is the amplitude of the fading path with the smallest propagation delay between the selected transmit antenna and the receive antenna, which is estimated by using a training sequence. After applying modulo operations, the projection coefficients for CPM signals are estimated and fed to the CPM demodulator.

An upper bound on the error performance of the proposed system is computed depending on the modulo operation errors at the receiver. The effect of the number of transmit antennas on the spectral efficiency of the system is analyzed. In the sim-

ulations, the envelope variations and the power spectrum of the precoded signals are depicted for different values of the system parameters. BER performance is presented for different number of antennas and different channel and bandwidth scenarios. The upper bound is shown to be consistent with the simulation results. Because transferring the equalization functions reduces the complexity significantly, a turbo receiver is also considered for coded CPM by performing iterations between the CPM demodulator and the channel decoder, which are both implemented by the Log-BCJR algorithm as described in Section 2.2.

The remainder of this chapter is organized as follows. Section 6.1 presents the proposed channel precoding scheme and the design of the training sequence. Analyses for the error performance and the number of transmit antennas required by the system are described in Section 6.2. Section 6.3 presents the simulation results.

## 6.1. Space-Time Pre-Equalization of Continuous Phase Modulation

At the beginning of this section, the TH-type pre-equalization of CPM in the presence of a single transmit antenna is described while the resulting precoded signal is stated to encounter large envelope variations that disrupt the spectral efficiency. Then, the space-time pre-equalizer is proposed so as to alleviate the envelope variations of the precoded signals by using a scaling factor that is determined depending on a transmit selection diversity scheme. The selected antenna transmits the CPM signal while the rest of the antennas transmit the spectrally-efficient precoded signals that are used to suppress the ISI at the receiver. At the end of the section, the design of the training sequence to estimate the amplitude of the first fading path between the selected transmit antenna and the receive antenna is presented. This amplitude information is the only channel parameter that must be known for the detection of CPM signals at the receiver.

The multipath channel in (2.23) fades slowly such that it is assumed to be time-

invariant throughout the duration of two data packets and is represented as

$$h(t) = \sum_{\ell=0}^{L_c-1} h_\ell \delta(t - \tau_\ell) \tag{6.1}$$

where $L_c$ is the number of paths, $h_\ell$ and $\tau_\ell$ are the fading coefficient and the propagation delay for the $\ell$th path, respectively, and $h_\ell = \rho_\ell e^{j\theta_\ell}$ with $\rho_\ell$ and $\theta_\ell$ denoting the amplitude and the phase of the $\ell$th path, respectively. The proposed method requires that the ISI on a symbol interval depends on the past symbols only, as in [35] and [36]. Therefore, it is assumed that $\tau_\ell - \tau_0 \geq T$ for $\ell = 1, \ldots, L_c - 1$. For simplicity, $\tau_0$ is assumed to be zero in the rest of the paper. Similar to [35] and [36], the channel information is perfectly obtained from the received packet at the transmitter and is used for pre-equalization of the downlink packet.

For the single antenna transmission, the CPE output signal $y(t, \mathbf{x}_1^k)$ in (2.14) is pre-equalized to form $z(t)$. The ISI signal obtained after the transmission of $z(t)$ through the multipath fading channels is expressed as

$$I(t) = \sum_{\ell=1}^{L_c-1} h_\ell z(t - \tau_\ell) \tag{6.2}$$

assuming that the channel coefficients $h_\ell$ are properly scaled to compensate for the shift in (2.14). A linear precoder with a transfer function equal to the inverse of the channel transfer function yields $z(t) = e^{-j\theta_0}\big(y(t, \mathbf{x}_1^k) - I(t)\big)/\rho_0$ and results in perfect ISI cancellation without any processing at the receiver. However, such a precoder is not stable unless all the zeros of the channel transfer function are inside the unit circle [35, 36]. To circumvent the stability problems, a non-linear precoder can be used, as in TH-type precoding. For this purpose, time-invariant complex coefficients are obtained by the projection of $I(t)$ in (6.2) onto the orthonormal basis functions in (2.27), which leads to

$$I_{k,i} = \int_{(k-1)T}^{kT} I(t)\phi_i^*\big(t - (k-1)T\big)dt, \qquad i = 1, \ldots, N_b, \tag{6.3}$$

at the $k$th symbol interval. Furthermore, the coefficients in (6.3) are divided by the amplitude of the first fading path, $\rho_0$, i.e.,

$$\tilde{I}_{k,i} = I_{k,i}/\rho_0, \qquad i = 1, \ldots, N_b, \tag{6.4}$$

to compensate for the scaling effect of $\rho_0$ after the transmission over the ISI channel. Then, modulo-$2\tilde{\mu}A_i$ and modulo-$2\tilde{\mu}B_i$ operations are applied to truncate the real and imaginary parts of $\tilde{I}_{k,i}$, respectively, to ensure stability. Here, $\tilde{\mu} \geq 1$ is the factor that defines the range of the modulo operations and

$$A_i = \max_{1 \leq m \leq \mathcal{P}M^L} \mathfrak{Re}(|\lambda_{m,i}|), \tag{6.5}$$

$$B_i = \max_{1 \leq m \leq \mathcal{P}M^L} \mathfrak{Im}(|\lambda_{m,i}|) \tag{6.6}$$

where $\lambda_{m,i} \in \Lambda_m$ and $i = 1, \ldots, N_b$. Then, the CPM signal in (2.14) can be precoded at the $k$th symbol interval as

$$z(t) = e^{-j\theta_0}\left[y(t, \mathbf{x}_1^k) - \sum_{i=1}^{N_b} \big(\tilde{I}_{k,i} + \zeta_{k,i} 2\tilde{\mu}A_i + j\xi_{k,i} 2\tilde{\mu}B_i\big)\phi_i\big(t-(k-1)T\big)\right], \ (k-1)T \leq t \leq kT \tag{6.7}$$

where $e^{-j\theta_0}$ compensates for the phase distortion of the first path, and $\zeta_{k,i}$ and $\xi_{k,i}$ are integers such that $\big(\mathfrak{Re}(\tilde{I}_{k,i}) + \zeta_{k,i} 2\tilde{\mu}A_i\big)$ and $\big(\mathfrak{Im}(\tilde{I}_{k,i}) + \xi_{k,i} 2\tilde{\mu}B_i\big)$ lie in the intervals $[-\tilde{\mu}A_i, \tilde{\mu}A_i]$ and $[-\tilde{\mu}B_i, \tilde{\mu}B_i]$, respectively.

The received signal can be represented as

$$r(t) = h_0 z(t) + I(t) + v(t) \tag{6.8}$$

where $v(t)$ is the AWGN with zero mean and two-sided power spectral density $N_0/2$. If a bank of filters matched to the orthonormal basis functions is applied to $r(t)$ in (6.8) at the $k$th signalling interval, the projection coefficients are obtained as

$$r_{k,i} = \int_{(k-1)T}^{kT} r(t)\phi_i^*\big(t-(k-1)T\big)dt = \rho_0 \tilde{a}_{k,i} - \zeta_{k,i} 2\tilde{\mu}\rho_0 A_i - j\xi_{k,i} 2\tilde{\mu}\rho_0 B_i + v_{k,i} \tag{6.9}$$

where the AWGN term $v_{k,i} = \int_{(k-1)T}^{kT} v(t)\phi_i^*\big(t-(k-1)T\big)dt$ has zero mean and variance $N_0$, and $\mathrm{E}[v_{k,i}v_{k,l}^*] = 0$ if $i \neq l$. The real and imaginary parts of $\rho_0\tilde{a}_{k,i}$ can be estimated by applying modulo-$2\tilde{\mu}\rho_0 A_i$ and modulo-$2\tilde{\mu}\rho_0 B_i$ operations to those of $r_{k,i}$, respectively. Because $A_i$ and $B_i$ denote the maximum absolute values that are obtained from the real and imaginary parts of the CPM projection coefficients for the $i$th basis function, respectively, no signal information is lost at the receiver when the additive noise is zero. However, the basis functions with the truncated coefficients in (6.7) result in huge envelope fluctuations and, thus, $z(t)$ cannot attain the narrow-band property of a CPM signal.

The ST pre-equalizer is proposed to meet the bandwidth requirements of CPM with small envelope variations, which uses a transmit selection diversity scheme to replace the signal for ISI cancellation in (6.7) by the CPM waveform in (2.14) and a residual signal. The signal for ISI cancellation is obtained as follows.

Considering $N_T$ transmit antennas, the ISI in (6.2) is modified as

$$I(t) = \sum_{p=1}^{N_T} \sum_{\ell=1}^{L_c-1} h_{\ell,p} z_p(t - \tau_{\ell,p}) \tag{6.10}$$

where $h_{\ell,p}$ is the $\ell$th path coefficient that corresponds to the $p$th antenna with $h_{\ell,p} = \rho_{\ell,p}e^{j\theta_{\ell,p}}$, $\tau_{\ell,p}$ is the $\ell$th path delay that corresponds to the $p$th antenna, and $z_p(t)$ is the precoded signal transmitted from the $p$th antenna. The antenna selection is performed by choosing the first path amplitude that minimizes the distance below as

$$s := \arg \min_{1 \leq p \leq N_t} \left| \rho_{0,p} - \frac{\rho_T}{\nu + 1} \right| \tag{6.11}$$

where $s$ is the index of the chosen antenna, $\rho_T = \sum_{p=1}^{N_T} \rho_{0,p}$ is the sum of the first path amplitudes for all transmit antennas, and $\nu > 1$ is a parameter to control the envelope variations. Using $I(t)$ in (6.10), $\{I_{k,i}\}$ are found as in (6.3), and (6.4) is modified as

$$\tilde{I}_{k,i} = \frac{\sqrt{N_T} I_{k,i}}{\rho_T - \rho_{0,s}}, \qquad i = 1, \ldots, N_b. \tag{6.12}$$

Then, defining

$$D_{k,i} := \tilde{a}_{k,i} + \tilde{I}_{k,i}, \tag{6.13}$$

$$\gamma := (\rho_{0,s})/(\rho_T - \rho_{0,s}), \tag{6.14}$$

modulo-$2\tilde{\mu}A_i\gamma$ and modulo-$2\tilde{\mu}B_i\gamma$ operations are applied to the real and imaginary parts of $D_{k,i}$, respectively, which leads to

$$\kappa_{k,i} = \tilde{a}_{k,i} + \tilde{I}_{k,i} + \zeta_{k,i}2\tilde{\mu}A_i\gamma + j\xi_{k,i}2\tilde{\mu}B_i\gamma \tag{6.15}$$

where $\zeta_{k,i}$ and $\xi_{k,i}$ are integers such that $\mathfrak{Re}(\kappa_{k,i})$ and $\mathfrak{Im}(\kappa_{k,i})$ lie in the intervals $[-\tilde{\mu}A_i\gamma, \tilde{\mu}A_i\gamma]$ and $[-\tilde{\mu}B_i\gamma, \tilde{\mu}B_i\gamma]$, respectively. The $\gamma$ ratio in (6.14) is the scaling

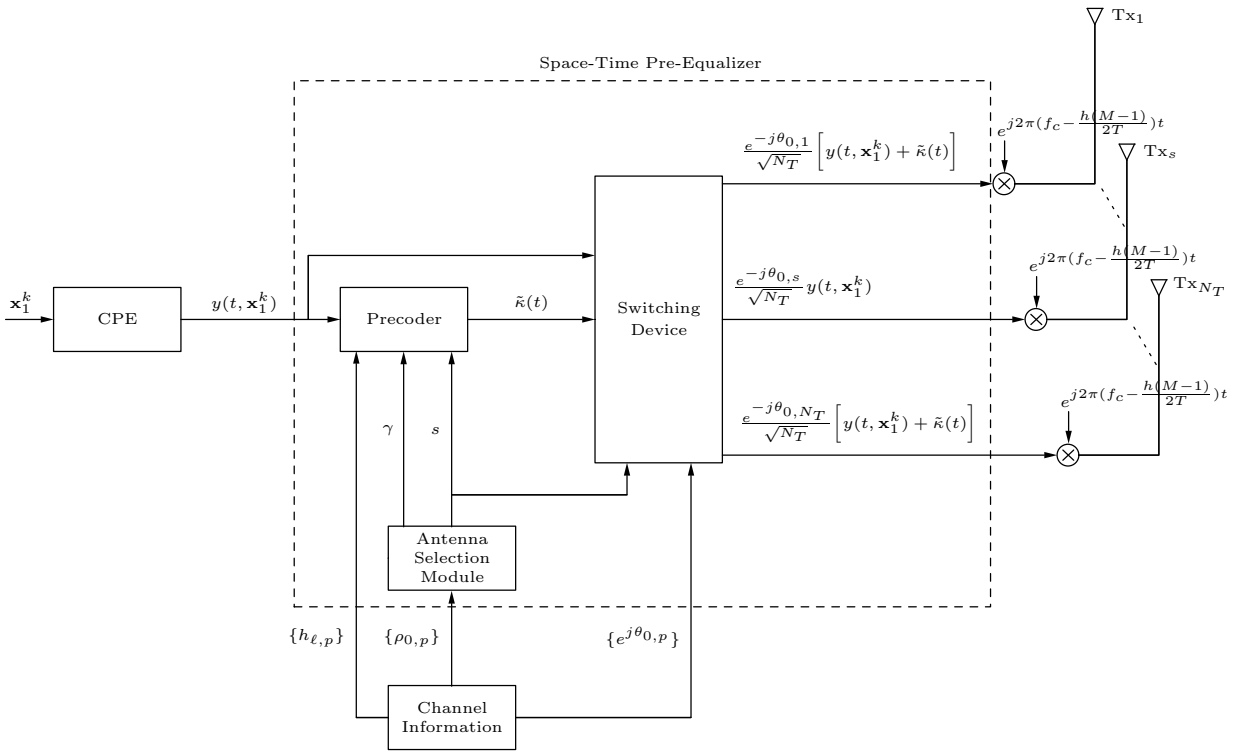



Figure 6.1. Space-time CPM pre-equalizer

factor that alleviates the envelope variations. Defining the residual signal as

$$\kappa(t) := -\sum_{i=1}^{N_b} \kappa_{k,i}\phi_i\big(t - (k-1)T\big), \qquad (k-1)T \le t \le kT, \tag{6.16}$$

the signal for ISI cancellation is obtained as $y(t, \mathbf{x}_1^k) + \kappa(t)$ whose projection onto the orthonormal bases yields the complex coefficients, $(-\tilde{I}_{k,i} - \zeta_{k,i} 2\tilde{\mu} A_i \gamma - j\xi_{k,i} 2\tilde{\mu} B_i \gamma)$, for $i = 1, \ldots, N_b$. For further spectral efficiency, the residual signal, $\kappa(t)$, is low-pass filtered with negligible energy loss to form $\tilde{\kappa}(t)$.

As shown in Figure 6.1, the $s$th antenna chosen using (6.11) transmits the CPM signal as

$$z_s(t) = \frac{e^{-j\theta_{0,s}}}{\sqrt{N_T}} y(t, \mathbf{x}_1^k), \qquad (k-1)T \leq t \leq kT, \tag{6.17}$$

and, for $1 \leq p \leq N_T$ and $p \neq s$, the corresponding antennas transmit the signals for ISI cancellation as

$$z_p(t) = \frac{e^{-j\theta_{0,p}}}{\sqrt{N_T}} \Big[ y(t, \mathbf{x}_1^k) + \tilde{\kappa}(t) \Big], \qquad (k-1)T \leq t \leq kT \tag{6.18}$$

where $1/\sqrt{N_T}$ in (6.17) and (6.18) is for energy scaling. After applying matched filtering to the received signal as in (6.9), we obtain

$$r_{k,i} = \frac{\rho_{0,s}}{\sqrt{N_T}} \Big[ \tilde{a}_{k,i} - \zeta_{k,i} 2\tilde{\mu} A_i - j\xi_{k,i} 2\tilde{\mu} B_i \Big] + v_{k,i}. \tag{6.19}$$

Then, assuming that $\rho_{0,s}$ is available at the receiver, the real and imaginary parts of $\rho_{0,s}\tilde{a}_{k,i}/\sqrt{N_T}$ are found by applying modulo-$2\tilde{\mu}\rho_{0,s}A_i/\sqrt{N_T}$ and modulo-$2\tilde{\mu}\rho_{0,s}B_i/\sqrt{N_T}$ operations to those of $r_{k,i}$, respectively. When the minimum distance in (6.11) is close to zero, $\gamma$ is approximately equal to $1/\nu$. Then the residual component in (6.18) diminishes by increasing $\nu$, which also improves the spectral efficiency of the signal, as also shown in Section 6.3. However, as observed in (6.11), it is more probable to choose a deep fading first path coefficient as $\nu$ increases. Therefore, there is a tradeoff between the power efficiency of the system and the PAPR of the precoded signal in (6.18).

The transmitter sends the value of $\rho_{0,s}$ to the receiver for the estimation of $\{\tilde{a}_{k,i}\}$ in (6.19). For this purpose, $\rho_{0,s}$ is quantized by considering $V = 2^J$ decision levels,

where the step size is $\alpha = C/(V-1)$ and $C$ is a positive constant that satisfies $\Pr(\rho_{0,s} > C) \approx 0$ given that $\rho_{0,s}$ is Rayleigh distributed. The quantized information is sent without any impact on the phase continuity and the constant envelope by using appropriate training symbols for CPM modulation. At the receiver, an ISI-free signal is obtained depending on the property that half of the $\mathcal{P}M^L$ tilted-phase CPM signals are the negative of the other half for even values of $\mathcal{P}$. Design of the training symbol sequence depends on the similarity of CPE to a recursive convolutional coder [6] where a length-$L_t$ tail sequence can be used to go from any state to the zero state in (2.19) or to the state in (2.20). The only difference of the latter state compared to the zero state is the value of $\tilde{\varphi}_k$. For simplicity, this state is referred as the '$\pi$ state' in the rest of this section. Denoting $N_c = \lceil \tau_{\max}/T \rceil + 1$ where $\lceil \cdot \rceil$ is the ceiling operation, $\tau_{\max}$ is the maximum delay among $\{\tau_{L_c-1,p}\}$, the length-$2(N_c + L_t)$ symbol sequences to represent $+1$ and $-1$ are

$$\mathbf{p}_k^{k+2(N_c+L_t)-1} = \{\tilde{\mathbf{Z}}_{s_k}\ \mathbf{0}_1^{N_c}\ \tilde{\mathbf{P}}_{s_{(k+N_c+L_t)}}\ \mathbf{0}_1^{N_c-1}\ X\}, \tag{6.20}$$

$$\mathbf{m}_k^{k+2(N_c+L_t)-1} = \{\tilde{\mathbf{P}}_{s_k}\ \mathbf{0}_1^{N_c}\ \tilde{\mathbf{Z}}_{s_{(1+N_c+L_t)}}\ \mathbf{0}_1^{N_c-1}\ X\}, \tag{6.21}$$

respectively, where $\mathbf{0}_1^{N_c}$ denotes an all-zero sequence with $N_c$ elements, $\tilde{\mathbf{Z}}_{s_k}$ and $\tilde{\mathbf{P}}_{s_k}$ are the length-$L_t$ tail sequences to go to the zero and $\pi$ states from the state $s_k$, respectively, and

$$X = \arg \max_{1 \le \tilde{x} \le M-1} \left[ \int_0^T \left| e^{j\pi h W(t)} - e^{j\pi h(4\tilde{x}q(t)+W(t))} \right|^2 dt \right]. \tag{6.22}$$

Using (2.14), $e^{j\pi h W(t)}$ and $e^{j\pi h(4\tilde{x}q(t)+W(t))}$ in (6.22) are the unit-amplitude CPM waveforms generated on the interval $0 < t < T$ by the state transition where the initial state is zero and the transition symbols are 0 and $\tilde{x}$, respectively. Then, assuming that $J = 3$, defining $L_s := N_c + L_t$, and starting at $k = 1$, a sample training sequence to convey the three-bit information, $\{b_1, b_2, b_3\} = \{+1, -1, +1\}$, can be represented by the waveform $y(t, \mathbf{t}_1^{6L_s})$, where

$$\mathbf{t}_1^{6L_s} = \left\{\mathbf{p}_1^{2L_s}\ \mathbf{m}_{2L_s+1}^{4L_s}\ \mathbf{p}_{4L_s+1}^{6L_s}\right\}. \tag{6.23}$$

All the antennas transmit the same training sequence such that

$$z_p(t) = \frac{e^{-j\theta_{0,p}}}{\sqrt{N_T}} y(t, \mathbf{t}_1^{6L_s}),\ 0 \le t \le 6L_sT,\ p = 1, \ldots, N_T. \tag{6.24}$$

At the receiver, the ISI-free signal is obtained as

$$r\big(t + (2i-1)L_sT - T\big) + r\big(t + 2iL_sT - T\big) = \frac{\rho_T}{\sqrt{N_T}} \Big( e^{j\pi h W(t) + j\pi\delta(b_i+1)} + e^{j\pi h(4Xq(t)+W(t))+j\pi\delta(b_i-1)} \Big) + v\big(t + (2i-1)L_sT - T\big) + v\big(t + 2iL_sT - T\big) \tag{6.25}$$

where $0 \le t \le T$, $i = 1, 2, \ldots, J$, $\delta(\cdot)$ is the Kronecker delta function, $e^{j\pi h W(t)+j\pi}$ and $e^{j\pi h(4Xq(t)+W(t))+j\pi}$ are the tilted-phase CPM waveforms generated by the state transitions where $\pi$ state is the initial state and the transition symbols are 0 and $X$, respectively, and $b_i \in \{-1, +1\}$. Defining $f(t) := e^{j\pi h W(t)} - e^{j\pi h(4Xq(t)+W(t))}$, the bit values and $h_{0,s}$ are computed as

$$\hat{b}_i = \mathrm{sgn}\Big\{ \int_0^T \Big[ r\big(t + (2i-1)L_sT - T\big) + r\big(t + 2iL_sT - T\big) \Big] f^*(t) dt \Big\}, \tag{6.26}$$

and

$$\hat{h}_{0,s} = \alpha \sum_{i=1}^{J} \tilde{b}_i 2^{i-1}, \tag{6.27}$$

respectively, where $\tilde{b}_i = (\hat{b}_i + 1)/2$. The duration of the training sequence to transmit a $J$-bit label is $J2L_s$ symbol periods.

## 6.2. Analyses for the Error Performance and the Number of Antennas

### 6.2.1. Upper Bound on the Error Performance

When the modulo operations are applied to $r_{k,i}$ in (6.19), errors are encountered especially due to deep fading on the first channel path and/or large noise power, caus-

ing a non-Gaussian observation noise in projection coefficient estimates and, therefore, deteriorating the system performance significantly. However, as the SNR increases and fewer coefficient estimates are affected by additive non-Gaussian noise at each symbol interval, more packets can be recovered without bit errors after CPM demodulation. Thus, modulo operation errors dominate the system performance and the average probability of having modulo operation errors at a symbol interval throughout a packet can be considered as an upper bound on the BER performance of the demodulator. Given the transmitted CPM burst and $\rho_{0,s}$, and considering the complex AWGN terms in (6.19), whose real and imaginary parts are mutually independent with zero mean and variance $N_0/2$, the average conditional probability of having modulo operation errors at a symbol interval is defined as

$$p_{me|\rho_{0,s},\tilde{\mathbf{a}}} := \frac{1}{N}\sum_{k=1}^{N} p_{me|\rho_{0,s},\tilde{a}_k} \tag{6.28}$$

where

$$p_{me|\rho_{0,s},\tilde{a}_k} = 1 - \frac{1}{\pi N_T N_0}\sum_{k=1}^{N}\prod_{i=1}^{N_b}\int_{-\rho_{0,s}\tilde{\mu}A_i}^{\rho_{0,s}\tilde{\mu}A_i} e^{-\frac{\left|u-\rho_{0,s}\Re\mathfrak{e}(\tilde{a}_{k,i})\right|^2}{N_T N_0}} du \int_{-\rho_{0,s}\tilde{\mu}B_i}^{\rho_{0,s}\tilde{\mu}B_i} e^{-\frac{\left|v-\rho_{0,s}\Im\mathfrak{m}(\tilde{a}_{k,i})\right|^2}{N_T N_0}} dv \tag{6.29}$$

and $u$ and $v$ are the random variables to represent the real and imaginary parts of $\rho_{0,s}\tilde{a}_{k,i} + \sqrt{N_T}v_{k,i}$, respectively. Then, the average probability of having a modulo operation error is

$$p_{me} = \int_{-\infty}^{\infty}\left(\sum_{\tilde{\mathbf{a}}} p(\tilde{\mathbf{a}}) p_{me|\rho_{0,s},\tilde{\mathbf{a}}}\right) f(\rho_{0,s}) d\rho_{0,s} \tag{6.30}$$

where $p(\tilde{\mathbf{a}})$ is the probability of having the projection coefficients $\tilde{\mathbf{a}}$ of the corresponding CPM burst and $f(\rho_{0,s})$ denotes the probability density function (pdf) of $\rho_{0,s}$. Considering independent and identically distributed (i.i.d.) sequences of uniformly distributed $M$-ary symbols, $\{\tilde{x}_k\}_1^N$, and starting CPM modulation at a certain state such as the

zero state, $p(\tilde{\mathbf{a}}) = 1/M^N$ for all possible packets, and

$$\sum_{\tilde{\mathbf{a}}} p(\tilde{\mathbf{a}}) p_{me|\rho_{0,s},\tilde{\mathbf{a}}} = \frac{1}{M^N} \sum_{\tilde{\mathbf{a}}} p_{me|\rho_{0,s},\tilde{\mathbf{a}}}. \tag{6.31}$$

Furthermore, because the $NM^N$ waveforms generated by the aforementioned symbol sequences are distributed almost uniformly over $\mathcal{P}M^L$ possible tilted phase CPM waveforms,

$$\frac{1}{M^N} \sum_{\tilde{\mathbf{a}}} p_{me|\rho_{0,s},\tilde{\mathbf{a}}} \approx \frac{1}{\mathcal{P}M^L} \sum_{m=1}^{\mathcal{P}M^L} p_{me|\rho_{0,s},\lambda_m} \tag{6.32}$$

where

$$p_{me|\rho_{0,s},\lambda_m} = 1 - \frac{1}{\pi N_T N_0} \prod_{i=1}^{N_b} \int_{-\rho_{0,s}\tilde{\mu}A_i}^{\rho_{0,s}\tilde{\mu}A_i} e^{-\frac{\left|u-\rho_{0,s}\mathfrak{Re}(\lambda_{m,i})\right|^2}{N_T N_0}} du \int_{-\rho_{0,s}\tilde{\mu}B_i}^{\rho_{0,s}\tilde{\mu}B_i} e^{-\frac{\left|v-\rho_{0,s}\mathfrak{Im}(\lambda_{m,i})\right|^2}{N_T N_0}} dv. \tag{6.33}$$

Then, from (6.30)-(6.32),

$$p_{me} \approx \frac{1}{\mathcal{P}M^L} \int_{-\infty}^{\infty} \left( \sum_{m=1}^{\mathcal{P}M^L} p_{me|\rho_{0,s},\lambda_m} \right) f(\rho_{0,s}) d\rho_{0,s}. \tag{6.34}$$

When the minimum distance in (6.11) is zero, the first fading path amplitude for the selected antenna is found as

$$\rho_{0,s} = \frac{\rho_T}{\nu + 1} = \frac{\sum_{p=1}^{N_T} \rho_{0,p}}{\nu + 1} \tag{6.35}$$

where $\{\rho_{0,p}\}$ are i.i.d. Rayleigh random variables with variance $(2 - \pi/2)\sigma_R^2$. In [71], an accurate closed-form pdf approximation for the sum of $N_T$ i.i.d. Rayleigh random variables with variance $(2 - \pi/2)$ is given as

$$f_{N_T}(\varepsilon) = \frac{\varepsilon^{2N_T-1} e^{-\varepsilon^2/(2b)}}{2^{N_T-1} b^{N_t} (N_T - 1)!} - \frac{(\varepsilon - a_2)^{2N_T-2} e^{a_1(\varepsilon-a_2)^2/(2b)}}{2^{N_T-1} b (b/a_1)^{N_T} (N_T - 1)!} \times a_0 [b(2N_T\varepsilon - a_2) - a_1\varepsilon(\varepsilon - a_2)^2] \tag{6.36}$$

with

$$\varepsilon = \rho/\sqrt{N_T} \tag{6.37}$$

where $\rho$ is the sum of the random variables. The values of the coefficients $b$, $a_0$, $a_1$, and $a_2$ change by the number of random variables in the sum, and they are computed in [71] for a wide range of $N_T$ values. Using the pdf in (6.36), $p_{me}$ can be numerically computed as

$$p_{me} \approx \frac{1}{\mathcal{P}M^L} \int_{-\infty}^{\infty} \left( \sum_{m=1}^{\mathcal{P}M^L} p_{me|\rho_{0,s},\lambda_m} \right) f_{N_T}(\varepsilon) d\varepsilon \tag{6.38}$$

where it can be found that $\rho_{0,s} = \sigma_R \sqrt{N_T}\, \varepsilon/(\nu+1)$ by using the expressions in (6.35) and (6.37).

### 6.2.2. Analysis for the Number of Antennas

The precoding scheme has to maintain small envelope variations for the spectral efficiency as described in Section 6.1. For limiting the envelope variations successfully, the minimum distance in (6.11) needs to be as small as possible so that the $\gamma$ values in (6.14) are not much larger than $1/\nu$. For a given value of $\nu$, the mean of the normalized minimum distance, $D := \frac{|\rho_{0,s} - \rho_T/(\nu+1)|}{\rho_T/\nu+1}$, can be used as an information measure to be evaluated for different $N_T$ values, where $\rho_T = \sum_{p=1}^{N_T} \rho_{0,p}$ as defined in Section 6.1. In this way, the number of transmit antennas yielding the minimum mean value and, thus, the most accurate $\gamma$ ratios can be determined. Using (6.11), the mean of $D$ is computed as

$$\begin{aligned} \mathrm{E}\{D\} := \bar{D} = \int_{\rho_{0,N_T}=0}^{\infty} \cdots \int_{\rho_{0,1}=0}^{\infty} & \frac{\min_{1\le p\le N_t} \left|\rho_{0,p} - \rho_T/(\nu+1)\right|}{\rho_T/(\nu+1)} \\ & f(\rho_{0,1}|\sigma) \ldots f(\rho_{0,N_T}|\sigma) d\rho_{0,1} \ldots d\rho_{0,N_T} \end{aligned} \tag{6.39}$$

where first fading path amplitudes with powers $\sigma^2$ are assumed to be i.i.d. Rayleigh random variables and $f(\xi|\sigma) = (\xi/\sigma^2) e^{-\xi^2/2\sigma^2}$. Then, using (6.39), $\bar{D}$ can be numer-

ically computed for different $N_T$ values and the number of antennas that results in the minimum $\bar{D}$ value can be determined. However, the computation of $\bar{D}$ becomes impractical as $N_T$ increases depending on the complexity of the integration operations in (6.39). By simulating large enough number of samples and assuming a stationary ergodic process, an accurate average can be used instead of (6.39). Then, considering samples from the aforementioned Rayleigh distribution and denoting $\rho_{0,p,i}$ and $\rho_{T,i}$ as the $i$th sample for the $p$th first path amplitude and the sum of $i$th samples for $N_T$ first path amplitudes, respectively, it can be concluded that

$$\lim_{m\to\infty} \frac{1}{m} \sum_{i=0}^{m} \frac{\min_{1\leq p\leq N_t} \left|\rho_{0,p,i} - \rho_{T,i}/(\nu+1)\right|}{\rho_{T,i}/(\nu+1)} = \bar{D}. \tag{6.40}$$

For small values of $N_T$, results obtained from (6.39) and (6.40) are also shown to be consistent in Section 6.3.

## 6.3. Simulations

The modulation scheme used in the simulations is 4-ary 3RC CPM with $h = 1/2$ [2]. Three pulses are used for nSnOEE where the optimized set of frequencies is found as $\{0.25/T, 0.95/T, 1/T\}$ in [57]. The precoding parameter $\tilde{\mu}$ is set as 1.5. Prior to the CPE block, the data bits are encoded according to a rate-1/2 convolutional code with generator polynomial $(7, 5)_8$. Then, the code bits are interleaved randomly. The duration of the packets is $N = 256$ symbol periods. The first path amplitude is estimated by appending a training sequence to each packet, where $J = 12$. In the simulations, continuous time-varying channel coefficients are such that $h_{\ell,p}(t) = h^r_{\ell,p}(t) + jh^i_{\ell,p}(t)$ where $h^r_{\ell,p}(t)$ and $h^i_{\ell,p}(t)$ are zero-mean Gaussian random variables, $E[h^r_{\ell,p}(t)h^i_{\ell,p}(t+\tau)] = 0$, $E[h^r_{\ell,p}(t)h^r_{\ell,p}(t+\tau)] = E[h^i_{\ell,p}(t)h^i_{\ell,p}(t+\tau)] = \sigma^2_{\ell,p}J_0(2\pi f_m\tau)/2$, with $J_0(.)$ being the zeroth order Bessel function of the first kind, $f_m$ being the maximum Doppler shift, and $\sigma^2_{\ell,p}$ being the power corresponding to $\ell$th path of the $p$th antenna. Furthermore $E[h_{\ell,p}(t)h^*_{\ell',p'}(t+\tau)] = 0$ if $\ell \neq \ell'$ and/or $p \neq p'$. The performance of the pre-equalizer is compared to that of the FDE in [22], which considers a single antenna at the transmitter and uses the aforementioned orthogonal bases for matched filtering at the receiver.

Because FDE in [22] assumes symbol-spaced multipath channels, the channel delays for the precoder are also chosen as $\tau_{\ell,p} = \ell T$, where the power of the path coefficients are $\sigma^2_{\ell,p} = e^{-\ell T/T} = e^{-\ell}$. The pre-equalization performance is also compared to that of the coded CPM in the presence of AWGN channel where a single antenna is deployed at the transmitter and the CPM demodulator is followed by the convolutional decoder at the receiver, without any equalization block at the front-end. For both the pre-equalizer and FDE, the number of channel taps is $L_c = 5$. During these simulations, Doppler spread is set as $f_m t_f = 0.001$ where $t_f$ is the duration of a packet with the training sequence. For the pre-equalizer, it is shown that the BER performance after CPM demodulation is upper bounded well by (6.38) for different system and channel parameters. The precoding performance is also observed with randomly spaced channel taps, where $L_c = 20$, $\tau_{0,p} = 0$ and $\tau_{\ell,p}$, $\ell = 1, \ldots, L_c - 1$, are uniformly distributed over $[T, 4T]$ for the $p$th antenna, the power of the path coefficients are $\sigma^2_{\ell,p} = e^{-\tau_{\ell,p}/T}$. In addition to $f_m t_f = 0.001$, scenarios with $f_m t_f = 0.005$ and $f_m t_f = 0.0005$ are evaluated to observe the system behavior in faster and slower varying multipath fading channels. It is possible to obtain further performance gain by employing turbo decoding between CPM demodulator and the channel decoder, as also depicted by the simulation results.

Table 6.1. Envelope Variations for the Precoded CPM

| | $\nu = 2$ | $\nu = 3$ | $\nu = 5$ | $N_T = 1$ |
|---|---|---|---|---|
| $\bar{\sigma}^2_{\varepsilon}$ (dB) | -8.4 | -10.1 | -12.7 | -6.3 |

Table 6.1 gives the envelope variations (in decibels) of the precoded signal, $y(t, \mathbf{x}_1^k) + \kappa(t)$, for different values of $\nu$ and the signal in (6.7).The variation is defined as $\bar{\sigma}^2_{\varepsilon} := \sum_{i=1}^{N_s} \frac{|\varepsilon_i - 1|^2}{N_s}$ where the sampling rate, $N_s$, is 64 samples/symbol, $\varepsilon_i$ is the magnitude at the $i$th sampling point, and the precoded signal is normalized to have unit average envelope magnitude. As shown in Table 6.1, envelope variations are reduced by increasing $\nu$. For $\nu = 2, 3$, and 5, it is found that approximately 99% of the precoded signal energies are concentrated in the frequency intervals $[-2.5/T, 2.5/T]$, $[-2/T, 2T]$, and $[-1.25/T, 1.25/T]$, respectively. Therefore, there is no significant energy loss by applying low-pass filtering to the residual part of the precoded signal. For filtering,

a square-root raised cosine pulse is employed where the roll-off factor is 0.25 and the

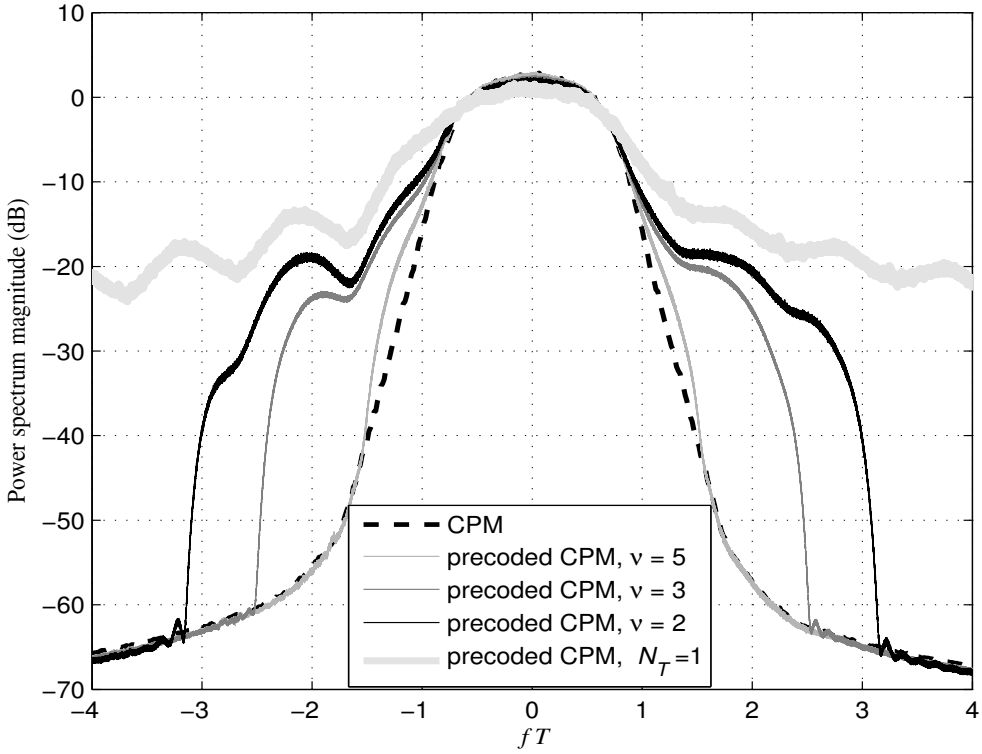



Figure 6.2. Power spectra for the original and the precoded CPM signals

main lobe width is set appropriately according to the bandwidth requirements of each case. The envelope variations are huge for the single antenna scenario. In Figure 6.2, power spectra of the precoded signals in (6.18) and (6.7) are compared to the spectrum of the original CPM signal by averaging the squared magnitude of the discrete Fourier transform of different packets [2]. Considering the $k$th symbol interval and the $i$th orthonormal basis function, the residual component in (6.16) corresponds to a square waveform with complex gain, $-\kappa_{k,i}$, that is multiplied by the complex exponentials in (2.9). The Fourier transform of this waveform is equivalent to the superposition of sinc pulses that are shifted in the frequency domain by $\{f_k\}$ in (2.9), respectively. Therefore, the power spectra for the precoded signals are asymmetric. The spectrum for $\nu = 5$ is almost the same as the spectrum of the original CPM signal. Decreasing $\nu$ results in bandwidth expansion but it becomes less likely to choose a deep fading first path coefficient as (6.11) yields. Therefore, there is a trade-off between the performance and the bandwidth requirements. Furthermore, it is also possible to avoid deep fading by increasing the number of transmit antennas while keeping $\nu$ constant

and maintaining the spectral efficiency. When the transmit selection diversity is not used ($N_T = 1$), bandwidth efficiency deteriorates.

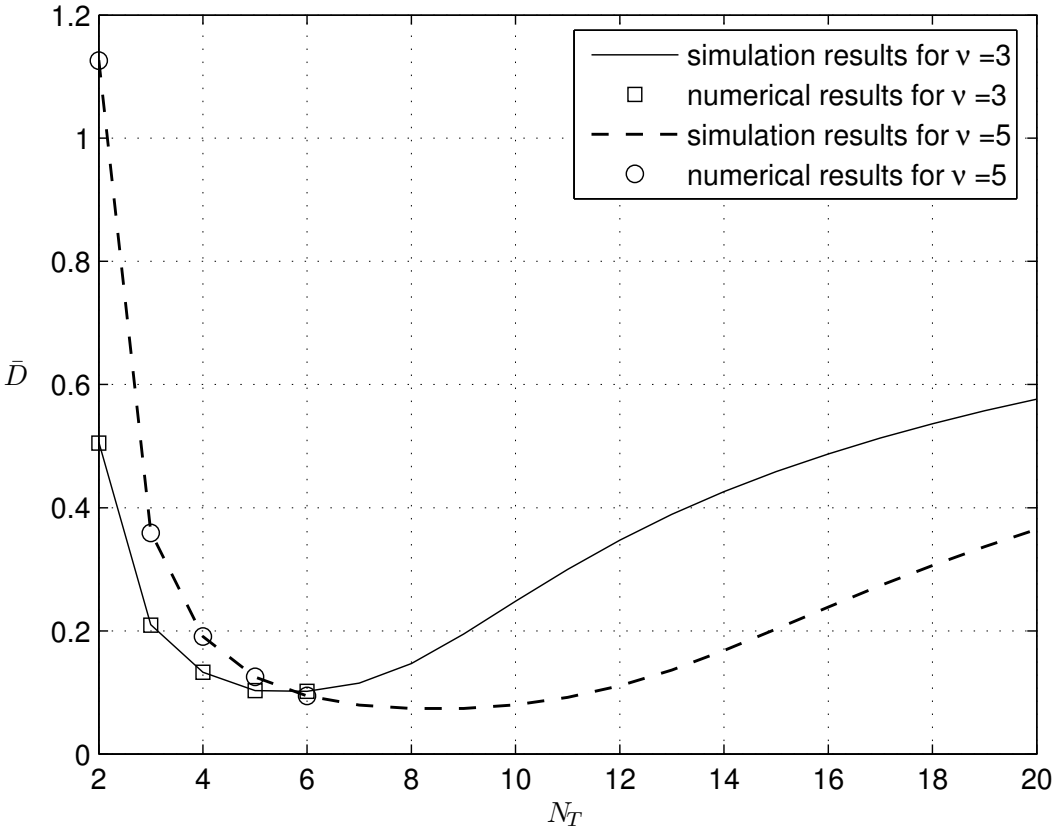



Figure 6.3. Distance $\bar{D}$ versus $N_t$ for $\nu = 3$ and 5

It is also possible to avoid deep fading by deploying more transmit antennas (which results in larger $\rho_T$). However, the distance in (6.11) needs to be small enough to maintain the spectral efficiency while increasing the number of antennas, as described in Section 6.2.2. In Figure 6.3, change of $\bar{D}$ while increasing $N_T$ is depicted with $\nu$ being equal to 3 and 5. Depending on the complexity issues, (6.40) is employed by simulating one million samples for each antenna. Simulation results are consistent with the numerical results found by (6.39) for up to six transmit antennas. As shown in Figure 6.3, small $\bar{D}$ values must be considered to maintain the spectral efficiency while determining the number of antennas.

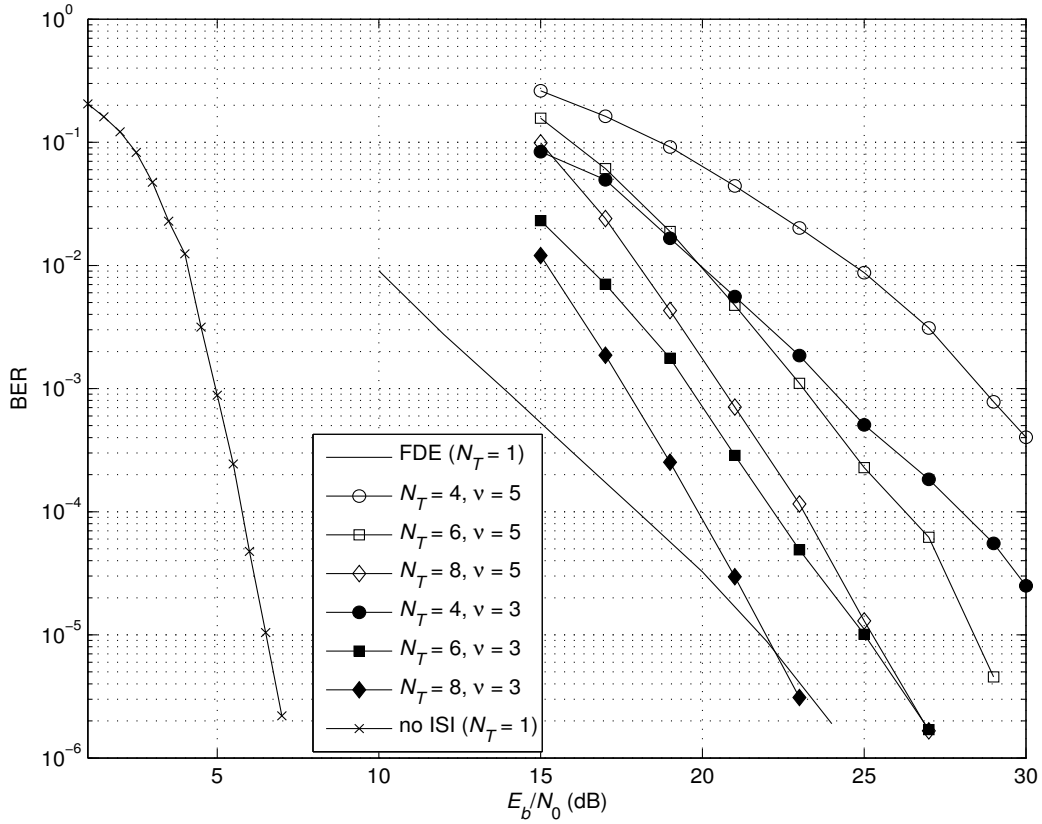



Figure 6.4. BER performance for the no ISI scenario, FDE, and the pre-equalizers

In Figure 6.4, BER performance of the pre-equalizer is illustrated for different values of $N_T$ and $\nu$ and is also compared to that of no ISI case and FDE. Both the pre-equalizer with $\nu = 3$ and $N_T = 8$ and the FDE go below BER $= 1 \times 10^{-5}$ at the same $E_b/N_0$ value. However, signal bandwidth is almost extended twice, whereas eight times more transmit antennas are deployed for pre-equalization. When $\nu = 5$, the performance gap between the pre-equalizer and FDE is about 6.5 dB and 3 dB at BER $= 1 \times 10^{-5}$ for $N_T = 6$ and $N_T = 8$, respectively, while the gap is around 15 dB at BER $= 1 \times 10^{-3}$ for $N_T = 4$. The spectral efficiency is almost as same as the original CPM signal as shown in Figure 6.2.

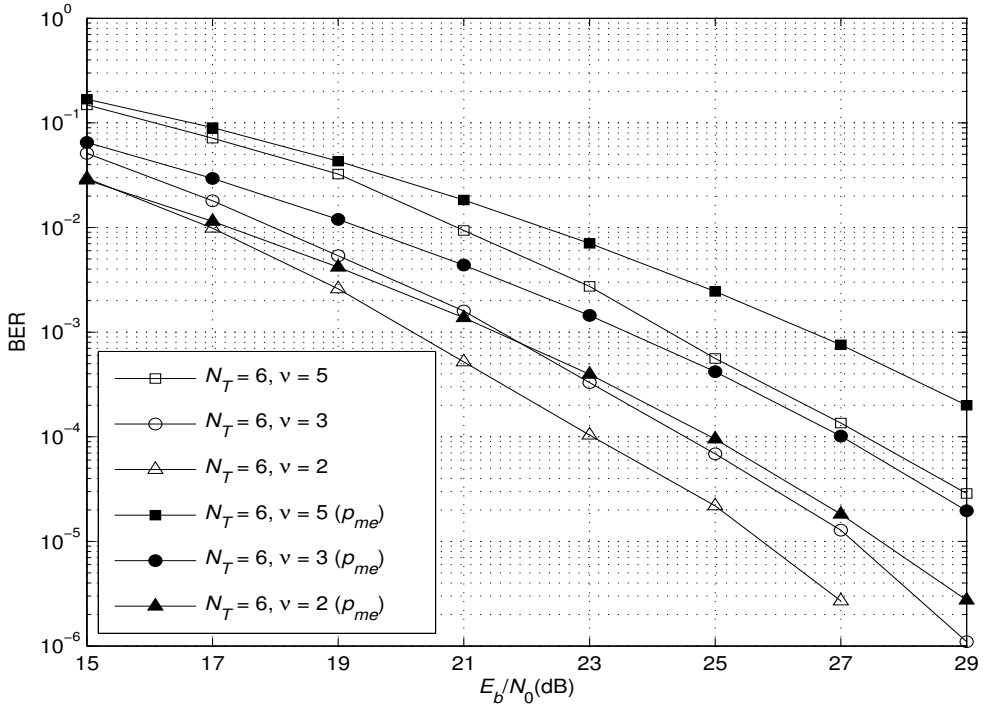



Figure 6.5. BER performance of the CPM demodulator and the upper bound, $p_{me}$, for $N_T = 6$

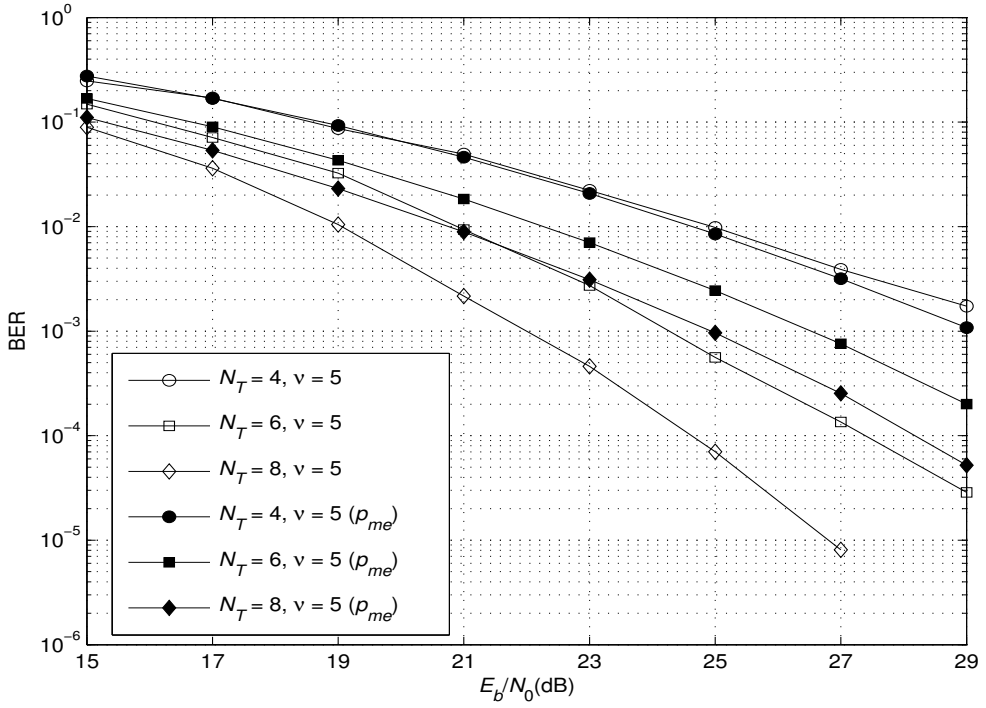



Figure 6.6. BER performance of the CPM demodulator and the upper bound, $p_{me}$, for $\nu = 5$

Performance-bandwidth and performance-spatial diversity trade-offs can also be

observed analytically by exploiting $p_{me}$ in (6.38). By setting the number of transmit antennas as $N_T = 6$, $p_{me}$ and BER performance after CPM demodulation are compared for different bandwidth scenarios in Figure 6.5, where $p_{me}$ is consistent with the system behavior and acts as an upper bound on the BER performance, as described in Section 6.2.1. Moreover, in Figure 6.6, $p_{me}$ and BER performance after CPM demodulation are compared for different number of transmit antennas, where $\nu = 5$. During the simulations to obtain the BER performance for the CPM demodulator, $\rho_{0,s}$ is assumed to be estimated perfectly and no low-pass filtering is applied to the residual signal to satisfy the same assumptions while deriving (6.38). Both simulation scenarios justify that the system performance depends on the modulo operation errors and $p_{me}$ can be used to understand the system behavior for different pre-equalizer and channel parameters. For $N_T = 4$, $p_{me}$ is not exactly an upper bound on the BER curves. This

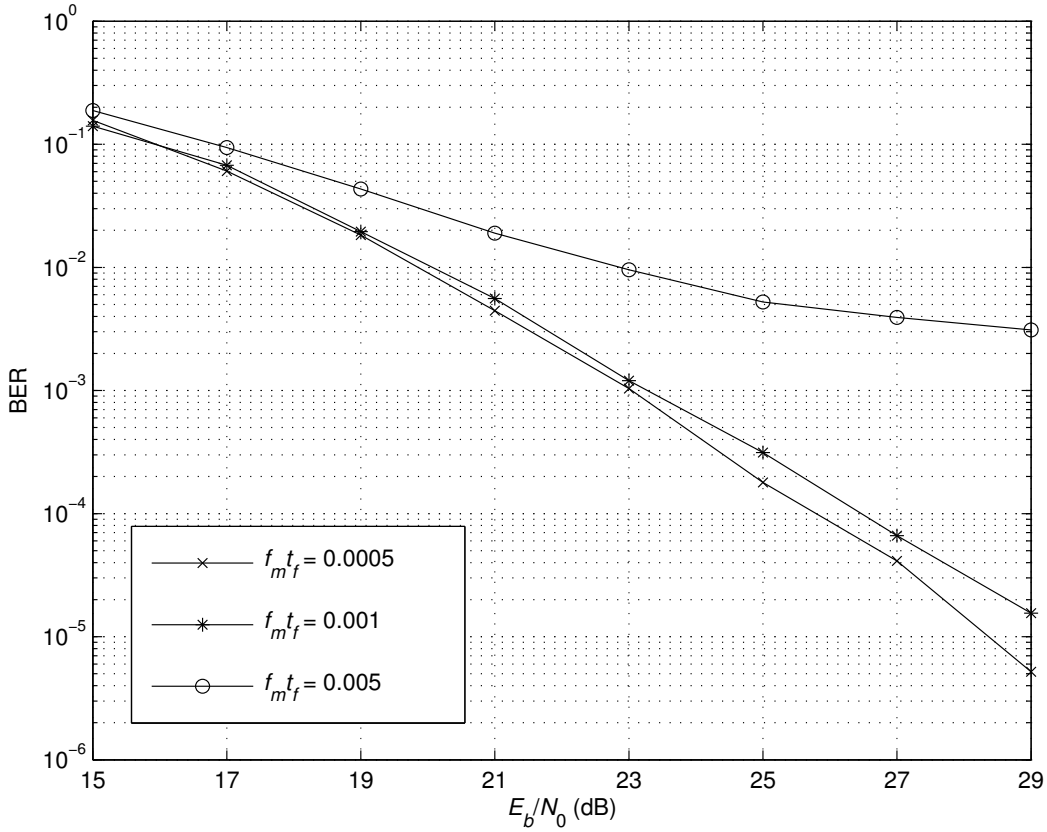



Figure 6.7. BER for different maximum Doppler spread ($f_m$) values, where $N_T = 6$, $\nu = 5$, and $L_c = 20$

is because the derivation of $p_{me}$ considers that the minimum distance in (6.11) is zero.

However, as shown in Figure 6.3, $\bar{D}$ value is greater for $N_T = 4$ than those for $N_T = 6$ and $N_T = 8$, respectively. Thus, because of larger deviations, it is more probable to choose a deep fading first path and to encounter modulo operation errors (which result in bit errors) compared to the theoretical results.

In Figure 6.7, the BER performance is also illustrated for different values of the maximum Doppler spread, $f_m$, where the aforementioned 20-tap multipath channels are considered with $N_T = 6$ and $\nu = 5$. The performance at $f_m t_f = 0.001$ is almost the same compared to the case where $f_m t_f = 0.0005$. An error floor is observed at $f_m t_f = 0.005$. For coded CPM, further gain is observed by performing iterations between the CPM demodulator and the channel decoder, which are both implemented

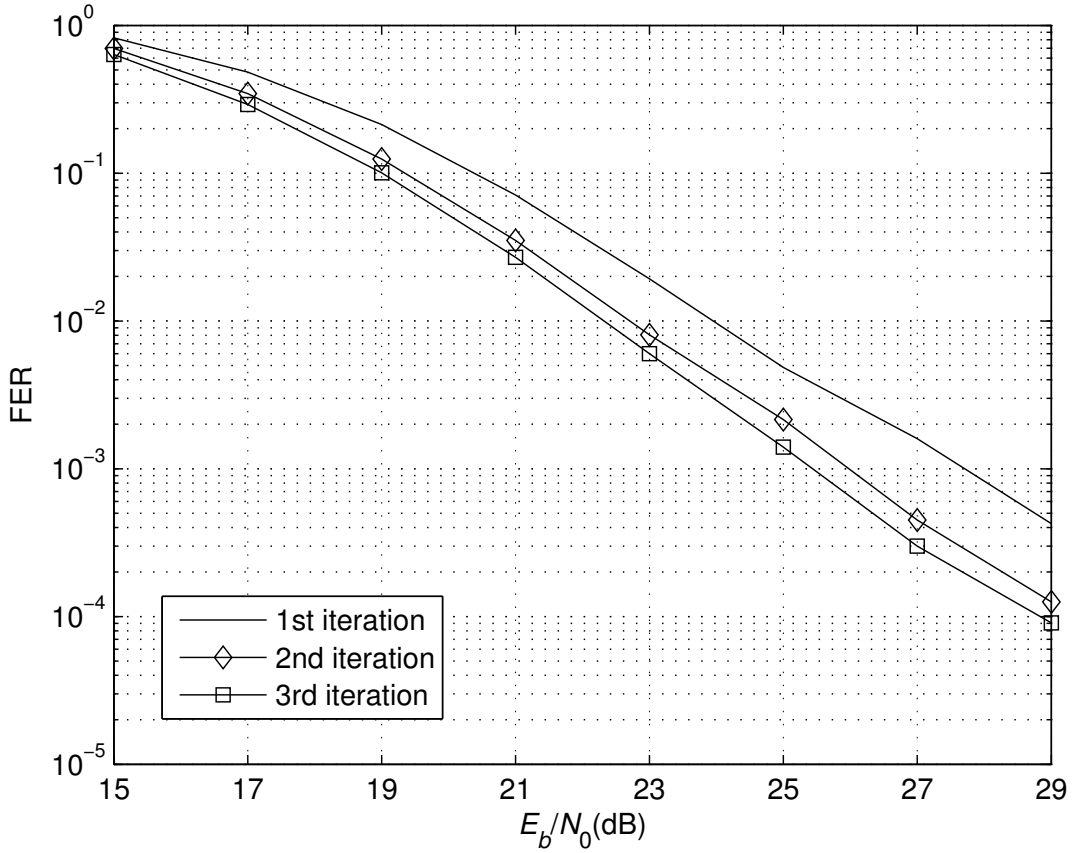



Figure 6.8. Turbo performance for $f_m t_f = 0.001$, $N_T = 6$, $\nu = 5$, and $L_c = 20$

by the BCJR algorithm [9]. In Figure 6.8, the frame error rate (FER) is shown for 20-tap multipath channels with $f_m t_f = 0.001$, $N_T = 6$ and $\nu = 5$, rather than the BER performance. FER is preferred for better presentation purposes since the modulo

operation errors result in non-Gaussian noise at lower SNRs, which makes the BER values increase after each iteration due to the incorrect modelling of the additive noise.

# 7. CONCLUSIONS

In this dissertaion, advanced transceiver designs are introduced for CPM on multipath fading channels by applying novel iterative and space-time methods. To reduce the detection complexity while attaining near-optimal performance, turbo receivers using soft-information-aided linear TDE and FDE filters are proposed for bit-interleaved coded CPM in Chapter 3 and 4, respectively. Then a ST block coding scheme is proposed in Chapter 5 to improve the performance of the turbo FDE. In Chapter 6, a ST pre-equalizer is proposed to mitigate the ISI effects of the multipath channel at the transmitter to remove the equalization functions at the receiver.

The low-complexity turbo receiver in Chapter 3 consists of a SIC/MMSE TDE at its front-end, and SISO demodulator and channel decoder blocks at its back-end. Doubly-iterative processing overcomes the performance degradation resulting from the suboptimality of the receiver. Performing a few BITs after each FIT, *a priori* information for the equalizer is improved, and faster convergence to low bit error rates is attained with less complexity. This behavior is also observed by EXIT chart analysis. Contrary to the CED methods, the proposed receiver does not result in very large super trellises with exponentially increasing number of states, which happens with longer channel length or higher modulation memory.

In Chapter 4, the doubly-iterative receiver with a SISO frequency-domain MMSE equalizer at the front-end is proposed for CPM with higher performance and less complexity than its counterparts also employing linear equalizers, such as the doubly-iterative receiver with TDE in Chapter 4 and TLE in [23] using a BFDE filter. For the application of the FDE, a cyclic guard interval is appended to the transmitted block by maintaining the phase continuity of CPM with each block and between the consecutive blocks. The convergence behavior of the proposed receiver is determined by EXIT chart analysis as in Chapter 3. Effectiveness of the new receiver is presented with comparisons in terms of the overall computational complexity and the BER simulations.

By proposing an orthogonal ST block coding scheme for CPM in Chapter 5 which is combined with FDE at the receiver, significant diversity gain is obtained. The proposed scheme is applied by maintaining the phase continuity of CPM where the orthogonality allows the application of FDE as in case of single antenna transmissions. By deploying only two transmit antennas, the proposed scheme combined with the turbo FDE in Chapter 4 results in even better performance than a turbo receiver using an optimal trellis-based CED module with high complexity and a back-end channel decoder.

In Chapter 6, a ST pre-equalization method is proposed for CPM that maintains the spectral efficiency with small envelope variations by using a transmit selection diversity scheme. As shown in the simulations, achieving a narrow spectrum deteriorates the power efficiency of the system. However, it is possible to improve the system performance by increasing the number of transmit antennas while preserving the spectral efficiency. The theoretical results for the error performance are also consistent with the simulation results. Despite its spatial complexity at the transmitter, the proposed method provides simplification at the receiver by removing the channel estimation and equalization functions. Only channel information to be estimated is the amplitude of a single channel path which is found by using a training sequence.

In this dissertation, perfect CSI is assumed to be available at either the transmitter or receiver. For future research work, the proposed designs for CPM offer a framework that can be extended to implement turbo receiver algorithms with a front-end channel estimator as well as adaptive turbo equalization algorithms without channel estimation functions. Furthermore, the multipath fading channel is assumed to be time-invariant throughout a transmitted block. Inspired by the work for the MMSE equalization of orthogonal frequency-division multiplexing in time-varying fading channels in [72]-[74], new turbo FDE designs for CPM that can operate under time-varying fading channels can be introduced.

# APPENDIX A: MEAN CPM SIGNALS BASED ON BIT PROBABILITIES

The *a priori* information for the SIC/MMSE equalization in Chapters 3 and 4 is not computed using the extrinsic information for the encoded bits produced by the demodulator over the CPM trellis because of the following reason.

In [48], the binary CPM signal is represented as the superposition of $N_p = 2^{L-1}$ PAM waveforms as

$$c(t, \mathbf{x}_1^N) = \sum_{n=1}^{N} \sum_{i=0}^{N_p-1} d_{n,i} D_i(t - (n-1)T) \tag{A.1}$$

with

$$d_{n,i} = e^{jh\pi\left(\sum_{k=1}^{n} x_k - \sum_{k=1}^{L-1} x_{n-k}\varepsilon_{i,k}\right)}, \tag{A.2}$$

where $x_k$ are the input bits and $\varepsilon_{i,k} \in \{0, 1\}$ are computed as in (2.8). Thus, $\mathrm{E}[d_{n,i}]$ needs to be computed to find $\mathrm{E}[c(t)]$. Using (A.2) and assuming independent bits,

$$\mathrm{E}[d_{n,i}] = \prod_{k=1}^{n} \mathrm{E}\left[e^{jh\pi x_k}\right] \prod_{k=1}^{L-1} \mathrm{E}\left[e^{-jh\pi x_{n-k}\varepsilon_{i,k}}\right]. \tag{A.3}$$

It is obvious that

$$\left|\mathrm{E}[e^{jh\pi x_k}]\right| \leq \mathrm{E}\left[|e^{jh\pi x_k}|\right] = 1. \tag{A.4}$$

Then, the magnitude of the complex mean $\mathrm{E}[e^{jh\pi x_k}]$ will be less than one unless $P(x_k = +1) = 1$ or $P(x_k = -1) = 1$. Thus, the magnitude of (A.3) goes to zero as $n$ increases. Since the MMSE equalizer is fed with zero mean values, and no SIC operation takes place, turbo processing is not possible unless the probabilities for the encoded bits are very close to one.

Here only binary CPM is considered for simplicity in the presentation. However, the result above can also be extended for $M$-ary CPM by using the PAM decomposition in [52] and following the same steps.

# APPENDIX B: MMSE FILTER COEFFICIENTS FOR SIC/FDE

The optimum FDE filter coefficients minimizes the MSE cost function in (4.8) which is equivalent to

$$\begin{aligned} J_{\mathrm{MSE}}(W) &= \mathrm{E}\left[\left|C_k - W_k\tilde{H}_k C_k - W_k V_k + W_k\tilde{H}_k\bar{C}_k - \mu\bar{C}_k\right|^2\right], \\ &= \mathrm{E}\left[\left|C_k - W_k\tilde{H}_k C_k - W_k V_k + W_k\tilde{H}_k\bar{C}_k - \frac{\bar{C}_k}{\tilde{N}}\sum_{\ell=0}^{\tilde{N}-1} W_\ell\tilde{H}_\ell\right|^2\right] \end{aligned} \tag{B.1}$$

where $\bar{C}_k = \mathrm{E}[C_k]$. The MMSE solution is found as

$$W_k = \frac{\tilde{H}_k^*\left(\mathrm{E}[|C_k|^2] - |\bar{C}_k|^2 + |\bar{C}_k|^2/\tilde{N} - |\bar{C}_k|^2\sum_{\ell=0}^{\tilde{N}-1} W_\ell\tilde{H}_\ell/\tilde{N}^2\right)}{|\tilde{H}_k|^2\left(\mathrm{E}[|C_k|^2] - |\bar{C}_k|^2\right) + \mathrm{E}[|V_k|^2]}. \tag{B.2}$$

Using the definition for $\mu$ in (4.6), (B.2) simplifies to

$$W_k = \frac{\tilde{H}_k^*\left(\mathrm{E}[|C_k|^2] - |\bar{C}_k|^2 + (1-\mu)|\bar{C}_k|^2/\tilde{N}\right)}{|\tilde{H}_k|^2\left(\mathrm{E}[|C_k|^2] - |\bar{C}_k|^2\right) + \tilde{N}\sigma_v^2} \tag{B.3}$$

where $\mathrm{E}[|V_k|^2]$ is replaced by $\tilde{N}\sigma_v^2$. Then the optimum FDE filter coefficients are computed by finding the joint solution of (4.6) and (B.3) for $\mu$ together and inserting the result into (B.3). Because $\{\bar{C}_k\}$ and $\mathrm{E}[|C_k|^2]$ change as new signal probabilities are delivered from the demodulator, the filter coefficients need to be updated at each equalizer iteration. To simplify the receiver, the FDE coefficients can be computed under ZAI and FAI assumptions by setting $\bar{C}_k = 0$ and $\bar{C}_k = C_k$, respectively. For ZAI case, (B.3) leads to

$$W_k^{\mathrm{ZAI}} = \frac{\mathrm{E}[|C_k|^2]\tilde{H}_k^*}{\mathrm{E}[|C_k|^2]|\tilde{H}_k|^2 + \tilde{N}\sigma_v^2}. \tag{B.4}$$

For FAI scenario, $|\bar{C}_k|^2$ is replaced by $\mathrm{E}[|C_k|^2]$ since it is assumed that $\bar{C}_k = C_k$, and (B.3) simplifies to

$$W_k^{FAI} = \frac{(1-\mu)\mathrm{E}[|C_k|^2]\tilde{H}_k^*}{\tilde{N}^2\sigma_v^2}. \tag{B.5}$$

The joint solution of (4.6) and (B.5) for $\mu$ results in

$$\mu = 1 - \frac{\tilde{N}^3\sigma_v^2}{\tilde{N}^3\sigma_v^2 + \sum_{\ell=0}^{\tilde{N}-1}\mathrm{E}[|C_\ell|^2]|\tilde{H}_\ell|^2}. \tag{B.6}$$

Inserting the solution in (B.6) into (B.5) leads to

$$W_k^{FAI} = \frac{\mathrm{E}[|C_k|^2]\tilde{H}_k^*}{\tilde{N}^2\sigma_v^2 + \sum_{\ell=0}^{\tilde{N}-1}\mathrm{E}[|C_\ell|^2]|\tilde{H}_\ell|^2/\tilde{N}}. \tag{B.7}$$

For simplicity, $\mathrm{E}\left[|C_k|^2\right]$ terms in (B.4) and (B.7) can be replaced by the average

$$\frac{1}{\tilde{N}}\sum_{k=0}^{\tilde{N}-1}|C_k|^2 = \frac{1}{\tilde{N}}\sum_{k=0}^{\tilde{N}-1}\sum_{n=0}^{\tilde{N}-1}\sum_{\ell=0}^{\tilde{N}-1}c_n c_\ell^* e^{-j2\pi(n-\ell)k/\tilde{N}} = \tilde{N}, \tag{B.8}$$

which is independent of the index $k$ and obtained through the symmetry of the DFT operation and the unit-amplitude CPM signals. After the replacement, it is found that

$$W_k^{\mathrm{ZAI}} = \frac{\tilde{H}_k^*}{\sigma_v^2 + |\tilde{H}_k|^2}, \tag{B.9}$$

$$W_k^{FAI} = \frac{\tilde{H}_k^*}{\tilde{N}\sigma_v^2 + (1/\tilde{N})\sum_{\ell=0}^{\tilde{N}-1}|\tilde{H}_\ell|^2}. \tag{B.10}$$

# APPENDIX C: TIME-REVERSED CPM SIGNALS

Reversing the baseband CPM signal in (2.1) in time on the interval $0 \leq t \leq NT$ yields

$$\breve{c}(t) := c(NT - t, \mathbf{x}_1^N) = e^{j\varphi(NT-t,\, \mathbf{x}_1^N)}. \tag{C.1}$$

To produce $\breve{c}(t)$ in (C.1), the real-time CPM signal must be stored at the transmitter before the time reversal. However, given the modulating symbol sequence $\mathbf{x}_1^N$, it is possible to modify the phase modulation procedure in (2.2) to obtain $\breve{c}(t)$ without storing and reversing $c(t, \mathbf{x}_1^N)$. Defining the new symbol sequence as $\breve{\mathbf{x}}_1^N := \mathbf{x}_N^1$ such that $\breve{x}_\ell = x_{N+1-\ell}$ for $\ell = 1, \ldots, N$,

$$\vartheta(t, \breve{\mathbf{x}}_1^k) = \vartheta_k \; + \; \vartheta_L(t, \breve{\mathbf{x}}_k^{k-1+L}), \qquad (k-1)T < t < kT \tag{C.2}$$

with

$$\begin{aligned} \vartheta_k &= \vartheta_{k-1} - \pi h \breve{x}_{k-1+L}, & \text{(C.3)} \\ \vartheta_L(t, \breve{\mathbf{x}}_k^{k-1+L}) &= 2\pi h \sum_{i=k}^{k-1+L} \breve{x}_i \breve{q}\big(t - iT + LT\big), & \text{(C.4)} \end{aligned}$$

for $k = 1, \ldots, N$, where $\breve{q}(t) = q(LT - t)$ and $\vartheta_k$ is initialized as $\vartheta_1 = \pi h \sum_{\ell=L+1}^{N} \breve{x}_\ell$. Using the continuous phase function in (C.2), the time-reversed CPM signal can be generated as

$$\breve{c}(t) = e^{j\vartheta(t, \breve{\mathbf{x}}_1^k)}, \qquad (k-1)T < t < kT. \tag{C.5}$$

The tilted-phase CPM signal after the time reversal can also be obtained by using the relation in (2.14) as

$$\breve{y}(t) = \breve{c}(t) e^{j\pi h(M-1)(NT-t)/T} = e^{j\tilde{\vartheta}(t, \breve{\mathbf{x}}_1^k)} \tag{C.6}$$

for $(k-1)T \leq t \leq kT$. Similar to (C.2)-(C.4), the tilted phase $\tilde{\vartheta}(t, \breve{\mathbf{x}}_1^k)$ can be represented as

$$\tilde{\vartheta}(t, \breve{\mathbf{x}}_1^k) = \tilde{\vartheta}_k \; + \; \tilde{\vartheta}_L(t, \breve{\mathbf{x}}_k^{k-1+L}) + \pi h \breve{\mathcal{W}}(t-(k-1)T), \qquad (k-1)T < t < kT \quad \text{(C.7)}$$

with

$$\tilde{\vartheta}_k = \tilde{\vartheta}_{k-1} - 2\pi h \breve{x}_{k-1+L}, \quad \text{(C.8)}$$

$$\tilde{\vartheta}_L(t, \breve{\mathbf{x}}_k^{k-1+L}) = 4\pi h \sum_{i=k}^{k-1+L} \breve{x}_i \breve{q}\big(t - iT + LT\big), \quad \text{(C.9)}$$

and $\breve{\mathcal{W}}(t) = \mathcal{W}(T-t)$, for $k = 1, \ldots, N$, where $\breve{x}_\ell = (\breve{x}_\ell + M - 1)/2$ and $\tilde{\vartheta}_k$ is initialized as $\tilde{\vartheta}_1 = 2\pi h \sum_{\ell=L+1}^{N} \breve{x}_\ell$.

# REFERENCES


1. Aulin, T. and C. E. Sundberg, "Continuous Phase Modulation-Parts I and II", *IEEE Transactions on Communications*, vol. COM-29, pp. 196-225, March 1981.

2. Anderson, J. B., T. Aulin, and C. E. Sundberg, *Digital Phase Modulation*, New York: Plenum, 1986.

3. Mulder, R. J., "DECT-A Universal Cordless Access System", *Philips Telecommunications Review*, vol. 49, pp. 68-73, September 1991.

4. Mouly, M. and M. B. Pautet, *The GSM System for Mobile Communications*, Telecom Publishing, 1992.

5. Zvonar, Z., P. Jung, and K. Kammerlander, *GSM: Evolution towards 3rd Generation Systems*, New York: Kluwer Academic, 2002.

6. Rimoldi, B., "A Decomposition Approach to CPM", *IEEE Transactions on Information Theory*, vol. 34, pp. 260-270, March 1988.

7. Brutel, C., J. Boutros, F. Belveze, "Serial Encoding and Iterative Detection of Continuous Phase Modulations", *Proceedings of the IEEE Global Telecommunications Conference*, Rio de Janeiro, Brazil, vol. 5, pp. 2375-2379, December 1999.

8. Narayanan, K. R. and G. L. Stüber, "Performance of Trellis-Coded CPM with Iterative Demodulation and Decoding", *IEEE Transactions on Communications*, vol. 49, pp. 676-87, April 2001.

9. Bahl, L. R., J. Cocke, F. Jelinek, and J. Raviv, "Optimal Decoding of Linear Codes for Minimizing Symbol Error Rate", *IEEE Transactions on Information Theory*, vol. IT-20, pp. 284-287, March 1974.

10. Yiin, L. and G. L. Stüber, "MLSE and Soft-Output Equalization for Trellis-Coded

Continous Phase Modulation", *IEEE Transactions on Communications*, vol. 45, pp. 651-659, June 1997.

11. Douillard, C., M. Jézéquel, and C. Berrou, "Iterative Correction of Intersymbol Interference: Turbo Equalization", *European Transactions on Telecommunications*, vol. 6, pp. 507-511, September/October 1995.

12. Laot, C., A. Glavieux, and J. Labat, "Turbo Equalization: Adaptive Equalization and Channel Decoding Jointly Optimized", *IEEE Journal on Selected Areas in Communications*, vol. 19, pp. 1744-1752, September 2001.

13. Tüchler, M., A. C. Singer, and R. Koetter, "Turbo Equalization: Principles and New Results", *IEEE Transactions on Communications*, vol. 50, pp. 754-767, May 2002.

14. Dejonghe, A. and L. Vandendorpe, "Turbo-Equalization for Multilevel Modulation: An Efficient Low-Complexity Scheme", *Proceedings of the IEEE International Conference on Communications*, New York, vol. 3, pp. 1863-1867, December 1999.

15. Tüchler, M., A. C. Singer, and R. Koetter, "Minimum Mean Squared Error Equalization Using A Priori Information", *IEEE Transactions on Signal Processing*, vol. 50, pp. 673-683, Mar. 2002.

16. Chung, K., K. M. Chugg, and J. Heo, "Reduced State Adaptive SISO Algorithms for Serially Concatenated CPM over Frequency-Selective Fading Channels", *Proceedings of the IEEE Global Telecommunications Conference*, San Antonio, TX, pp. 1162-1166, November 2001.

17. Hansson, A. and T. Aulin, "Generalized APP Detection of Continuous Phase Modulation over Unknown ISI Channels", *IEEE Transactions on Communications*, vol. 53, pp. 1615-1619, October 2005.

18. Cheung, J. C. S. and R. Steele, "Soft-Decision Feedback Equalizer for Continuous

Phase Modulated signals in Wideband Mobile Radio Channels", *IEEE Transactions on Communications*, vol. 42, pp. 1628-1638, February-April 1994.

19. Sari, H., G. Karam, and I. Jeanclaud, "Transmission Techniques for Digital Terrestrial TV Broadcasting", *IEEE Communications Magazine*, vol. 33, pp. 100-109, February 1995.

20. Tüchler, M. and J. Hagenauer, "Turbo Equalization Using Frequency Domain Equalizers," *Proceedings of the Allerton Conference*, Monticello, IL, October 2000.

21. Falconer, D., S. L. Ariyavisitakul, A. Benyamin-Seeyar, and B. Edision, "Frequency Domain Equalization for Single-Carrier Broadband Wireless Systems", *IEEE Communications Magazine*, vol. 40, pp. 58-66, April 2002.

22. Tan, J. and G. L. Stüber, "Frequency Domain Equalization for Continuous Phase Modulation", *IEEE Transactions on Wireless Communications*, vol. 4, pp. 2479-2490, September 2005.

23. Pancaldi, F. and G. M. Vitetta, "Equalization Algorithms in the Frequency Domain for Continuous Phase Modulations", *IEEE Transactions on Communications*, vol. 54, pp. 648-658, April 2006.

24. Zhang, X. and M. P. Fitz, "Space-Time Code Design with Continuous Phase Modulation", *IEEE Journal on Selected Areas in Communications*, vol. 21, pp. 783-792, June 2003.

25. Zhang, X. and M. P. Fitz, "Soft-Output Demodulator in Space-Time-Coded Continuous Phase Modulation", *IEEE Transactions on Signal Processing*, vol. 50, pp. 2589-2598, October 2002.

26. Wang, G. and X. -G. Xia, "An Orthogonal Space-Time Coded CPM System with Fast Decoding for Two Transmit Antennas", *IEEE Transactions on Information Theory*, vol. 50, pp. 486-493, March 2004.

27. Wang, G., W. Su, and X. -G. Xia, "Orthogonal-Like Space-Time Coded CPM with Fast Demodulation for Three and Four Transmit Antennas", *Proceedings of the IEEE Global Telecommunications Conference*, San Francisco, CA, vol. 6, pp. 3321-3325, December 2003.

28. Zhao, W. and G. B. Giannakis, "Reduced Complexity Receivers for Layered Space-Time CPM", *IEEE Transactions on Wireless Communications*, vol. 4, pp. 574-582, March 2005.

29. Maw, R. L. and D. P. Taylor, "Space-Time Coded Systems Using Continuous Phase Modulation", *IEEE Transactions on Communications*, pp. 2047-2051, vol. 55, pp. 2047-2051, November 2007.

30. Sivester, A.-M., R. Schober, and L. Lampe, "Burst-Based Orthogonal ST Block Coding for CPM", *IEEE Transactions on Wireless Communications*, vol. 6, pp. 1208-1212, April 2007.

31. Al-Dhahir, N., "Single-Carrier Frequency-Domain Equalization for Space-Time Block-Coded Tranmissions over Frequency-Selective Fading Channels", *IEEE Communication Letters*, vol. 5, pp. 304-306, July 2001.

32. Fischer, R. F. H., *Precoding and Signal Shaping for Digital Transmission*, New York: J. Wiley-Interscience, 2002.

33. Tomlinson, M., "New Automatic Equalizer Employing Modulo-Arithmetic", *Electronic Letters*, vol. 7, pp. 138-39, March 1971.

34. Harashima, H. and H. Miyakawa, "Matched Transmission Technique for Channels with Intersymbol Interference", *IEEE Transactions on Communications*, vol. C-20, pp. 774-780, August 1972.

35. Chan, Y.-L. and W. Zhuang, "Channel Precoding for Indoor Radio Communications Using Dimension Partitioning", *IEEE Transactions on Vehicular Technology*,

vol. 48, pp. 98-114, January 1999.

36. Lee, J. S. Y. and W. Zhuang, "Channel Precoding with Small Envelope Variations for $\pi/4$-QPSK and MSK over Frequency-Selective Slow Fading Channels", *IEEE Transactions on Vehicular Technology*, vol. 52, pp. 24-36, January 2003.

37. Choi, R. L. and R. D. Murch, "A Transmit MIMO Scheme with Frequency Domain Pre-Equalization for Wireless Frequency Selective Channels", *IEEE Transactions on Wireless Communications*, vol. 3, pp. 929-938, May 2004.

38. Guo, Y. and B. C. Levy, "Worst-Case MSE Precoder Design for Imperfectly Known MIMO Communications Channels," *IEEE Transactions on Signal Processing*, vol. 53, pp. 2918-2930, August 2005.

39. Scaglione, A., P. Stoica, S. Barbarossa, G. B. Giannakis, and H. Sampath, "Optimal Designs for Space-Time Linear Precoders and Decoders", *IEEE Transactions on Signal Processing*, vol. 50, pp. 1051-2930, May 2002.

40. Windpassinger, C., R. F. H. Fischer, T. Vencel, and J. B. Huber, "Precoding in Multiantenna and Multiuser Communications", *IEEE Transactions on Wireless Communications*, vol. 3, pp. 1305-1316, July 2004.

41. Thesken, T. M., "Trellis Coding on a Channel Having Precoding, Continuous Phase Modulation, and Differential Detection", Proceedings of the IEEE Military Communications Conference, vol. 3, pp. 1018-1022, November 1991.

42. Trachtman, A., I. Kalet, and S. Shamai (Shitz), "Limiter-Discriminator Detection of Continuous Phase Modulation (CPM) - Tomlinson Filtering", *IEEE Transactions on Communications*, vol. COM-42, pp. 819-825, February-April 1994.

43. Crozier, S. N., "Precompensated Frequency Modulation (PFM) Designed for $\pi/4$-Shifted QPSK Receivers", *Proceedings of the 18th Biennial Symposium on Communications*, Queens University, Kingston, Canada, 1996.

44. Low, M. A. and P. H. Wittke, "Precoded Nonlinear Constant-Envelope Modulations", *Proceedings of the URSI International Symposium on Signals, Systems, and Electronics*, pp. 349-355, 29 September-2 October 1998.

45. Varshney, P. and C. Hessel, "Performance of Trellis Coded M-ary 1RC CPM with Linear Receiver and Pre-coding", *Proceedings of the IEEE Military Communications Conference*, vol. 1, pp. 373-376, October 2000.

46. Brink, S. ten, "Convergence Behavior of Iteratively Decoded Parallel Concatenated Codes", *IEEE Transactions on Communications*, vol. 49, pp. 1727-1737, October 2001.

47. Tüchler, M., "Convergence Prediction for Iterative Decoding of Threefold Concatenated Systems", *Proceedings of the IEEE Global Telecommunications Conference*, Taipei, Taiwan, November 2002, pp. 1358-1362.

48. Laurent, P. A., "Exact and Approximate Construction of Digital Phase Modulation by Superposition of Amplitude Pulses (AMP)", *IEEE Transactions on Communications*, vol. 34, pp. 150-160, February 1986.

49. Saleh, A. A. M. and R. A. Valenzuela, "A Statistical Model for Indoor Multipath Propagation", *IEEE Journal on Selected Areas in Communications*, vol. SAC-5, pp. 128-137, February 1987.

50. Suzuki, H., "A Statistical Model for Urban Radio Propagation", *IEEE Transactions on Communications*, vol. COM-25, pp. 673-680, July 1977.

51. Hashemi, H., "The indoor radio propagation channel", Proceedings of IEEE, vol. 81, pp. 943-967, July 1993.

52. Mengali, U. and M. Morelli, "Decomposition of M-ary CPM Signals into PAM Waveforms", *IEEE Transactions on Information Theory*, vol. 41, pp. 1265-1275, September 1995.

53. Perrins, E. and M. Rice, "PAM Decomposition of M-ary Multi-h CPM", *IEEE Transactions on Communications*, vol. 53, pp. 2065-2075, December 2005.

54. Cariolaro, G. and A. M. Cipriano, "Minimal PAM Decomposition of CPM Signals with Seperable Phase", *IEEE Transactions on Communications*, vol. 53, pp. 2011-2014, December 2005.

55. Wylie-Green, M. P., "A New Finite Series Expansion of Continuous Phase Modulated Waveforms", *IEEE Transactions on Communications*, vol. 55, pp. 1547-1556, August 2007.

56. Huber, J. and W. Liu, "An Alternative Approach to Reduced-Complexity CPM Receivers", *IEEE Journal on Selected Areas in Communications*, vol. 7, pp. 1437-1449, December 1989.

57. Zhao, Q. and G. L. Stüber, "Robust Time and Phase Synchronization for Continuous Phase Modulation", *IEEE Transactions on Communications*, vol. 54, pp. 1857-1869, October 2006.

58. Forney, G. D., "The Viterbi algorithm", *Proceedings of IEEE*, vol. 61, pp. 268-278, March 1973.

59. Hagenauer, J. and P. Hoeher,"A Viterbi Algoritm with Soft-Decision Outputs and its Applications", *Proceedings of the IEEE Global Telecommunications Conference*, Dallas, Texas, pp. 47.1.1-47.1.7, November 1989.

60. Seshadri, N. and C.E. Sundberg, "List Viterbi Decoding Algorithms with Applications", *IEEE Transactions on Communications*, vol. 42, pp. 313-323, February-April 1994.

61. Robertson, P., E. Villebrun, and P. Hoeher, "A Comparison of Optimal and Sub-Optimal MAP Decoding Algorithms Operating in the Log Domain", *Proceedings of the IEEE International Conference on Communications*, Seattle, WA, pp. 1009-

1013, June 1995.

62. Viterbi, A. J., "An Intuitive Justification and a Simplified Implementation of the MAP Decoder for Convolutional Codes", *IEEE Journal on Selected Areas in Communications*, vol. 16, pp. 260-264, February 1998.

63. Franz, V. and J. B. Anderson, "Concatenated decoding with a reduced-search BCJR algorithm," *IEEE Journal on Selected Areas in Communications*, vol. 16, no. 2, pp. 186-195, February 1998.

64. Lin, S. and D.J. Costello, Jr., *Error Control Coding*, 2nd ed. NJ: Pearson Prentice Hall, 2004.

65. Luise, M., R. Reggiannini, and G. M. Vitetta, "Blind Equalization/Detection for OFDM Signals over Frequency-Selective Channels", *IEEE Journal on Selected Areas in Communications*, vol. 16, pp. 1568-1578, October 1998.

66. Proakis, J., *Digital Communications*, 3rd ed. New York: McGraw-Hill, 1995.

67. Oppenheim, A. V. and R. W. Schafer, *Discrete-Time Signal Processing*, Englewood Cliffs, N.J.: Prentice Hall, 1989.

68. Alamouti, S., "A Simple Transmit Diversity Technique for Wireless Communications", *IEEE Journal on Selected Areas in Communications*, vol. 16, pp. 1451-1458, October 1998.

69. Balanis, C. A., *Antenna Theory: Analysis and Design*, New York: Harper, 1982.

70. Cheng, D. K., *Field and Wave Electromagnetics*, Reading, MA: Addison-Wesley, 1991.

71. Hu, J. and N. C. Beaulieu, "Accurate Simple Closed-Form Approximations to Rayleigh Sum Distributions and Densities", *IEEE Communications Letters*, vol. 9, pp. 109-111, February 2005.

72. Cai, X. and G. B. Giannakis, "Bounding Performance and Suppressing Intercarrier Interference in Wireless Mobile OFDM", *IEEE Transactions on Communications*, vol. 51, pp. 2047-2056, December 2003.

73. Schniter, P., "Low Complexity Equalization of OFDM in Doubly Selective Channels", *IEEE Transactions on Signal Processing*, vol. 52, pp. 1002-1011, April 2004.

74. Rugini, L., P. Banelli, and S. Cacopardi, "Simple Equalization of Time-Varying Channels for OFDM", *IEEE Communications Letters*, vol. 9, pp. 619-621, July 2005.